Capillary adhesion and friction : an approach with the AFM Circular Mode

Hussein Nasrallah

UNIVERSITE DU MAINE

LABORATOIRE DE PHYSIQUE DE L'ETAT CONDENSE – MOLECULAR LANDSCAPES AND BIOPHOTONIC SKYLINE GROUP -UMR CNRS 6087

PhD Thesis

Specialty: Physics and Condensed Matter

Capillary adhesion and friction –An approach with the AFM Circular Mode

Defended on December 5th, 2011 by

Hussein NASRALLAH

In front of the jury composed of:

Ernst MEYER	
Professor - University of Basel – Switzerland	***President***
Liliane LEGER	
Professor Emérite - Université Paris-Sud XI Orsay - France	***Reviewer***
Denis MAZUYER	
Professor - Ecole Centrale de Lyon - France	***Reviewer***
Dominique AUSSERRE	
Director of Research - CNRS - Université du Maine - France	***Examinator***
Pierre-Emmanuel MAZERAN	
Associate Professor (HDR) - Université de Compiègne - France	***Collaborator***
Olivier NOEL	
Associate Professor - Université du Maine - France	***Thesis Director***

Abstract

The aim of this thesis is concerned with the influence of sliding velocity on capillary adhesion at the nanometer scale. In ambient conditions, capillary condensation which is a thermally activated process, allows the formation of a capillary meniscus at the interface between an atomic force microscope (AFM) probe and a substrate. This capillary meniscus leads to a capillary force that acts as an additional normal load on the tip, and affects the adhesion and friction forces.

The Atomic Force Microscopy (AFM) offers interesting opportunities for the measurement of surface properties at the nanometer scale. Nevertheless, in the classical imaging mode, limitations are encountered that lead to a non stationary state. These limitations are overcome by implementing a new AFM mode (called Circular AFM mode).

By employing the Circular AFM mode, the evolution of the adhesion force vs. the sliding velocity was investigated in ambient conditions on model hydrophilic and hydrophobic surfaces with different physical-chemical surface properties such as hydrophilicity. For hydrophobic surfaces, the adhesion forces or mainly van der Waals forces showed no velocity dependence, whereas, in the case of hydrophilic surfaces, adhesion forces, mainly due to capillary forces follow three regimes. From a threshold value of the sliding velocity, the adhesion forces start decreasing linearly with the logarithm increase of the sliding velocity and vanish at high sliding velocities. This decrease is also observed on a monoasperity contact between a atomically flat mica surface and a smooth probe, thus eliminating the possibility of the kinetics of the capillary condensation being related to a thermally activated nucleation process as usually assumed. Therefore, we propose a model based on a thermally activated growth process of a capillary meniscus, which perfectly explains the experimental results.

Based on these results, we focused on directly investigating with the Circular mode the role of capillary adhesion in friction mechanisms. We investigated the influence of the sliding velocity on the friction coefficient, and a decrease following three regimes, similar to the sliding velocity dependence of the capillary adhesion, was observed for hydrophilic surfaces that possess a roughness higher than 0.1 nm. Whereas, an increase of the friction coefficient was observed on hydrophilic (Mica) or hydrophobic (HOPG) atomically flat surfaces that posses a roughness lower than 0.1 nm. However, in this latter case, the three regimes are not established. Finally, on a rough hydrophobic surface, the friction coefficient was sliding

velocity independent. A direct comparison with capillary adhesion behavior with the sliding velocity is expected to give new insights to explain this interplay.

Keywords*: Atomic force microscopy, capillary adhesion, capillary condensation, adhesion force, friction, friction coefficient, roughness.*

ACKNOWLEDGEMENTS

A thesis work is not conceivable without the support of many people. I would like to express to everyone who contributed to this thesis my sincere gratitude.

I would like to thank all the members of the Jury, for their attendance and for the fruitful discussion we had.

I would especially like to thank Olivier noel, my supervisor, for his many suggestions and constant support during this research. His advices were always helpful.

I sincerely thank my Pierre Emannuel Mazeran that was as a co-supervisor. Without his careful proof and valuable comments, this thesis cannot be as good as it is.

For Financial support, I would like to acknowledge the National Research Agency (ANR).

Many thanks for all my friends that were beside me through this thesis, I appreciate their help

I would like to thank my parents and my sisters for their continuous support during my study and my PhD.

Finally I thank my wife Samar for being by my side through each step of this PhD. It is her how gave me the strength to continue through all difficult times.

Dedicated to my father, mother, sisters, and wife

Contents

Introduction

Friction, the force that prevents the sliding of two bodies in contact has become of considerable interest for both scientific and technologic research fields. From an essential side, it is a universal phenomenon that is manifested in many natural behaviors such as earthquake dynamics or physics of granular media [1-3]. From a technological side, friction causes energy dissipation that in turn causes setbacks in the durability and autonomy of systems, thus a reduction of this energy loss is a necessity to minimize economical and environmental costs [4]. Over viewing macroscopic scale friction and the laws that govern the elementary process of friction leads to a conclusion that a study at this scale is not sufficient and that fundamental studies of friction on nanometer-scale are mandatory. Nevertheless, a better comprehension of the elementary mechanisms of friction at the nanometer scale is not an easy task. Indeed, the nature of the sliding contact depends on many parameters that are hidden and not easily accessible even at the nanoscale. Anyway, newly developed techniques such as the AFM offer new opportunities for investigating friction at the nanoscale, unfortunately, experimental limitations are encountered with commercial AFMs. Such limitations are related to the sliding motion, which is back and forth, and results in a halt of the displacement when the inversion occurs. This halt could lead to an evolution of the nature of the contact or to a non stationary experimental state. As a result, and to eliminate these inconveniences, we have developed a new AFM mode called the Circular AFM mode [5]. This new mode is particularly useful if one wants to study time dependant phenomena. In particular, at the nanoscale, capillary condensation occurs when two hydrophilic surfaces are in contact leading to capillary adhesion which is time dependent [6]. Moreover, the capillary adhesion acts as an additional normal load to the applied external load on the contact, therefore, in a sliding contact it plays an indirect role in friction mechanisms. The role of capillary adhesion was assumed by various authors [7, 8] to be the reason behind the decrease of friction forces with the sliding velocity. However, this assumption is not based on direct experimental evidence of the behavior of capillary adhesion in a sliding nanometer-sized contact.

In this manuscript, we present direct experimental results obtained with the new Circular AFM mode from investigating the influence of sliding velocity on capillary adhesion. We show that these experimental findings are perfectly explained by a newly developed theoretical model. Friction force measurements are also performed with the Circular mode on

various surfaces and the friction coefficient behavior with the sliding velocity is discussed by considering the interplay of capillary adhesion during sliding.

Chapter 1. From Tribology to Nanotribology

We briefly review the historical background relative to the macroscopic friction and present an overview of contact mechanic in the case of two solids in direct contact before focusing on the nanotribological branch of tribology which studies friction phenomenon at the nanometer scale. We begin by introducing the surface forces resulting from the interaction at close proximity. A second part of this chapter discusses the theoretical explanations of friction at the nanometer scale focusing on the thermally activated process of capillary condensation, and an analytical background on the interplay of the contacts surface characteristics such as roughness, and different environmental condition such as humidity with the capillary force, and finally we give a overview on the previous experimental research conducted for investigating the dependence of the friction force on the sliding velocity .

1. Introduction to tribology – Macro and Microscopic approaches to the laws of friction

The term "tribology" was suggested by Peter Jost in May of 1966 as a name for the research based on the phenomena associated to the contact and relative motion of surfaces. The pursuit for knowledge about origins of friction, lubrication, adhesion, and wear is not a recent scientific activity. Indeed, tribology is one of the oldest fields of interest, dating back from the creation of fire through frictional heating to the current efforts of creating nanodevices. Furthermore, much attention has been paid to study the physical and chemical origin of these phenomena in order to obtain and design ways and means for minimizing losses such as energy dissipation and material degradation that can cause huge economic losses [9, 10].

In spite of the enormous amount of macroscopic tribological research so far, mainly of empirical nature, a clear fundamental understanding of friction still does not exist [11, 12] . The main reason for this lack of fundamental insight is the inherent difficulty to study

interactions that take place at the buried interface of two contacting bodies. A macroscopic contact between two apparently flat solid surfaces consists in practice of a large number of micro- contacts between the asperities that are present on both contacting surfaces [13], as schematically illustrated in Figure 1.1. This notion inspired Frank Philip Bowden [14] in 1950 to the following analogy: "Putting two solids together is rather like turning Switzerland upside down and standing it on Austria - the area of intimate contact will be small ".
In reality, friction is dependent of the atomic interaction between the contacting asperities, and of the macroscopic elastic and plastic deformation that determine the morphology and stress distribution within these contacts [13, 15].

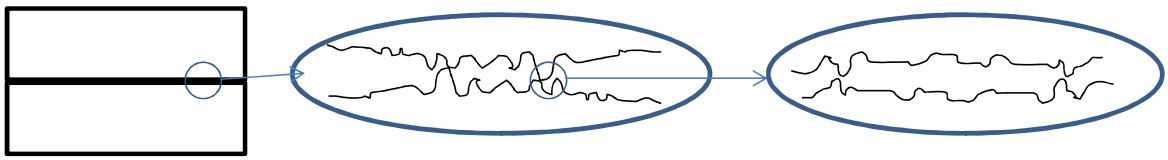

Figure 1.1: Schematic representation of asperities upon asperities.

Nevertheless, at the macroscopic scale the essentials behind the friction mechanism are not well understood due to lack of insight at the contact interface. Therefore, in order to get a better understanding of the friction phenomena, one should study friction at the micro- and nanoscale. However, one should keep in mind that the friction laws have first originated at the macroscale.

1.1. Laws of Amontons and Coulomb

The first scientific documentation of the phenomenon of friction was formulated by Leonardo da Vinci (1452-1519) in the 15th century 200 years before Newton defined the laws of force and mechanics. Da Vinci deduced the rules governing the motion of a rectangular block sliding over a flat surface. He introduced for the first time, the concept of the coefficient of friction as the ratio of the friction force to normal load. However, his work had no historical influence, because his notebooks remained unpublished for hundreds of years. In 1699, the French physicist Guillaume Amontons (1663-1705) rediscovered the rules of friction after he studied dry sliding between two flat surfaces [16].

Guillaume Amontons published his two laws of friction in the proceedings of the French Royal Academy of Science [17]. These laws are now known as the Amontons laws of friction:

First law of friction	*The friction force is proportional to the normal load.*
Second law of friction	*The friction force is independent of the apparent area of contact.*

To these observations the French physicist Charles-Augustin Coulomb (1736-1806), added a third rule:

Third law of friction	*The friction force is independent of sliding velocity.*

The first law can be expressed by the simple equation:

$$F_F = \mu F_N \qquad 1.1$$

, where "μ" is called the coefficient of friction[1], The expression of the first law also implies the second friction law that friction is independent of the apparent area of contact [19].

Amontons first law, that friction is proportional to the load, was readily accepted by the French royal academy as it fitted with the everyday experiences that heavy objects are more difficult to slide than light objects. The second law, that friction is independent of the apparent area of contact, however, was harshly disputed as many thought that friction should also scale with the real contact area.

The third law of friction stated that the friction force is independent of velocity once motion starts. In particular the force needed to initiate sliding is usually greater than that necessary to maintain it. Coulomb also made a clear distinction that the coefficient of static friction μ_s is greater than the coefficient of dynamic friction μ_k [16].

These initial ideas about how friction originates have now evolved over 300 years to where friction between two solid surfaces is thought to originate via different mechanisms such as adhesion.

1 Typically μ is included in between 1/5 and 2/3 for non lubrified surfaces 18. Bharat Bhushan and B.K. Gupta, Handbook of Tribology: Materials, Coatings, and Surface Treatments. 1997: Krieger Publishing Company, Malabar, Florida U.S.A.

1.2. Bowden and Tabor adhesion model

Desanguliers (1734) proposed *adhesion,* the force required to separate two bodies in contact, as an element in the friction process, a hypothesis which appeared to contradict experiments because of the independence of friction on the contact area (Amontons 2nd law).

The contradiction between the adhesive issue and Amontons 2nd law cleared up in the 1930s and 1940s by Bowden and Tabor who introduced the concept of the *real area of contact* A_R. The real area of contact is made up of a large number of small regions of contact, referred to as asperities or junctions of contact, where atom-to-atom contact takes place, pointing out that the true area of contact between two solids is only a small fraction of the apparent contact area A_{App}.

There are various experimental techniques that can be employed to measure the real area of contact such as: ultrasonic technique, neutron-graphic method, paints and radioactive traces, and two of the most important techniques are the optical and the resistance or conductance methods. The measurement of the contact area depends on the properties of the contacting materials. When at least one of the contacting materials is transparent, optical microscopy or interferometer may be used; however, resolution will be limited and the estimated contact area may be wrong. For electrically conducting materials, one can measure the electrical resistance between two conductors and calculate the contact area from the measured electrical resistance and the specific resistivity of the materials [13]. For other materials, reflection and transmission of ultrasound at the interface can be employed [20].

Typical ratios for A_R/A_{App} of 10^{-3}- 10^{-5} were found with contact diameters of the order of some micrometers. Using an optical microscopy, Dieterich and Kilgore [21] imaged the real contact area (as well as its change with the load) by bringing two rough, transparent surfaces in contact and detecting the light passing perpendicular through the contact zone by an optical microscope. Only in those points where the two surfaces were in intimate contact, light could pass straight through while in all other places it would be scattered by the rough surfaces (Fig. 1.2).

By the use of these macroscopic scale measuring methods, it was found that the friction is scaling with the real area of contact A_R. However, these methods do not result in accurate measurements at the nanoscale. Nevertheless, the advancement in nano-technique development, nowadays, offers techniques that help measure the real area of contact with high precision. Such techniques are the Scanning Electron Microscopy (SEM) or the Transmission Electron Microscopy (TEM). Indeed, new experimental setups allow performing tests inside a

TEM chamber using modified *in-situ* techniques. This permits real-time visualization of the contact geometry and its evolution [22].

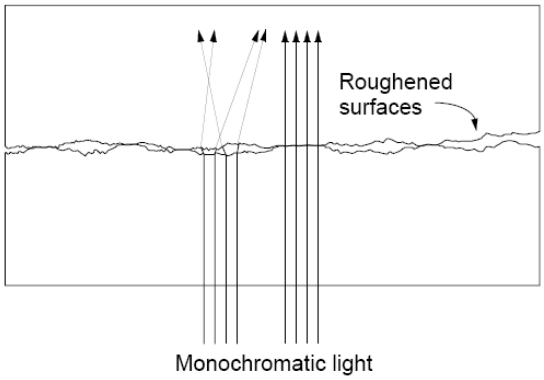

Figure 1.2: Schema representing a light transmitted through rough sliding surfaces, the light is scattered except at the contacts.

Bowden and Tabor developed a model to describe the connection between adhesive forces and friction forces and performed experiments to verify these concepts [14]. Their model postulates that the friction (F_F) arises from the forces required to shear the adhesive junctions and therefore is proportional to the real contact area, that is,

$$F_F = \sigma A_R \qquad 1.2$$

where σ denotes the shear stress at the contacting interface, and the model can be known as the plastic junction model, based on the plastic deformation of the asperities due to the friction mechanism [23]. However, the model is also known as the adhesion model since friction, same as adhesion, is proportional to the real area of contact.
The shear stress (friction yield stress) is defined by the lateral force per unit area, and is given by:

$$\sigma = F_F / A_R \qquad 1.3$$

Moreover a general assumption for a linear dependence of the shear stress on the acting pressure can be understood if one considers the total stress, σ, as comprised of the intrinsic material shear strength, σ_0, plus the compression stress αP_m:

$$\sigma = \sigma_0 + \alpha P_m \quad 1.4$$

, where σ_0 is a constant that refers to the stress at zero load, and P_m corresponds to the normal pressure (the normal force acting on a unit area F_N/A_R). By equating equations 1.3 and 1.4, a dependence of friction on the normal force is obtained

$$F_F = \sigma A_R = (\sigma_0 A_R + (\alpha P_m) A_R) = (\sigma_0 A_R + \alpha F_N) \quad 1.5$$

From eq. 1.5 it can be noted that for high normal pressure (P_m is high compared to σ_0); the model reduces to the Amontons 1st law (with the friction coefficient μ being equal to α).

$$F_F \approx \mu F_N \quad 1.6$$

The friction force becomes independent of the contact area. However, friction may also be dependent on the area of contact, and the contact area under the effect of normal load (F_N) acting on the asperities changes from compliant materials to rigid surfaces, and would be larger in compliant materials than that of the rigid ones due to the elasticity of the materials.
Furthermore, in the case of plastic contact ($P_m = H$), H is the hardness of the material, eq. 1.5 leads to:

$$F_F = \frac{\sigma}{H} F_N = \left(\frac{\sigma_0}{H} + \alpha\right) F_N \quad 1.7$$

The Amontons 1st law is retrieved with μ being equal to $\left(\frac{\sigma_0}{H} + \alpha\right)$. In the case of an elastic or elastic-plastic contact, there exist several examples that have retrieved a non linear dependence of the friction force on the load in the case of two asperities in contact. If a Hertz contact between two spheres is considered (where the applied load has a 2/3 dependence with the area of contact) (see section 1-2.1), and the law of Tabor is applied, a 2/3 dependence is obtained for the friction on the normal load.
Greenwood and Williamson (GW) further improved the model by considering a contact between a flat surface and a rough surface that is covered with a large number of spherically shaped asperities, the asperities have identical radii of curvature and randomly varying heights [24]. In the model the asperity heights follow a statistical distribution, which implies that the number of asperities exceeding a height h above the average surface level can be approximated. And he showed that the area of increases linearly with the applied load.

Therefore, a direct dependence of friction on the normal force was obtained leading to the recovery of 1st Amontons Law.

By assuming a multi asperity contact the Amontons Law can be reestablished, and in order to comprehend the behavior of the contact in relative motion, one should look down to the single-asperity level.

2. Contact mechanics – *Single asperity contacts*

When two surfaces come into contact, for example, when a tip contacts a sample surface, the formed asperities are subjected to forces that will lead to deformations of both sample and tip. Information concerning the contact can be unraveled by studying it at the single asperity level. There are several models based on continuum mechanics which predict how friction force should scale with the normal load and the contact area.

2.1. Fully elastic: The Hertz model

In 1882 Heinrich Hertz solved the problem of the elastic contact between a sphere and a planar surface and between two spheres [25]. His approach assumes that adhesion and surface forces can be neglected. He considered two spheres (radii R_1 and R_2) compressed by a force F_N resulting in a contact area of radius a (Fig. 1.3). Hertz derived equations for the contact radius a and the indentation depth δ between the spheres:

$$a = \left(\frac{3F_N R^*}{4E^*}\right)^{\frac{1}{3}} \qquad 1.8$$

$$\delta = \frac{a^2}{R^*} \qquad 1.9$$

, where R^* describes the effective sphere radius and E^* the effective Young's modulus defined as:

$$\frac{1}{E^*} = \frac{1-\nu_1^2}{E_1} + \frac{1-\nu_2^2}{E_2} \quad \text{and} \quad R^* = \frac{R_1 R_2}{R_1 + R_2} \qquad 1.10$$

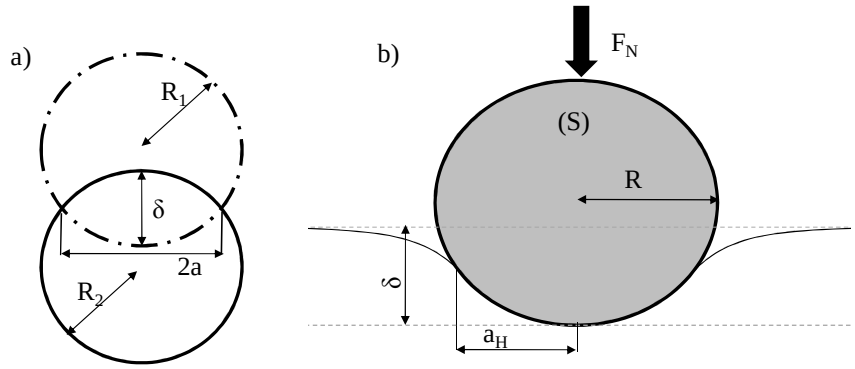

Figure 1.3: Hertz model a) for two compressed spheres (radii R_1 and R_2) and b) for an elastic sphere (S) in contact with an elastic half space. With the Hertz contact radius a_H and penetration depth δ. For the purpose of a better illustration the dimensions are exaggerated.

Here E_i are the Young's moduli and ν_i the Poisson ratios of the two bodies. Combining equations 1.8 and 1.9 it becomes clear that the penetration depth δ is proportional to the $F^{2/3}$

$$\delta = \sqrt[3]{\frac{9F_N^2}{16E^*R^*}} \qquad 1.11$$

And correspondingly, the force to achieve a certain penetration δ is given as:

$$F_N = \frac{4}{3}E^*\sqrt{R^*}\delta^{\frac{3}{2}} \qquad 1.12$$

By substituting Eq. (1.8) in (1.12), a relation between the force and the contact radius can be observed

$$F_N = \frac{4}{3}E^*\sqrt{R^*}\left(\frac{a^2}{R^*}\right)^{\frac{3}{2}} \qquad 1.13$$

The proportionality between the contact radius and the area of contact lead to a proportionality of both with the force

$$a \propto F_N^{\frac{1}{3}} \qquad and \qquad (A_R = \pi a^2) \qquad 1.14$$

Assuming the friction force is proportional to the real area of contact (as in Tabor theory), equation 1.14 leads to:

$$F_F \propto {F_N}^{2/3} \tag{1.15}$$

Moreover, the total force compressing the solids can be expressed in relation to the pressure by:

$$F_N = \int_{-a}^{a} P(r)\, 2\pi r\, dr \tag{1.16}$$

, where P(r) is the pressure distribution over the contact and is given by Hertz to be

$$P(r) = P_0 \sqrt{\left(1 - \left(\frac{r}{a}\right)^2\right)} \tag{1.17}$$

, where r ranges from $-a$ to a. Eq. 1.17 shows that the contact pressure is zero at the edges and is maximum at the center of the contact. Therefore the maximum pressure of contact would be

$$P_0 = \frac{3F_N}{2\pi a^2} = \frac{3}{2\pi} \sqrt[3]{\frac{16\, {E^*}^2 F_N}{9{R^*}^2}} \tag{1.18}$$

The average pressure can be given by the force acting on the area of contact:

$$P_m = \frac{F_N}{\pi a^2} = \frac{1}{\pi} \sqrt[3]{\frac{16\, {E^*}^2 F_N}{9{R^*}^2}} \tag{1.19}$$

When assuming the case of SPM, the limiting case where $R_2 \rightarrow \infty$ (spherical surface with radius R_1 on a flat surface) becomes important.

The Hertz theory allows calculating the contact shape and forces between two contacting surfaces under the influence of an external force. It does not include any surface force and therefore the Hertz model describes accurately the contact between elastic bodies in the absence of adhesion, and the fact that the adhesion is not considered in this model leads to big errors in calculations where attractive forces play the dominant role. In 1971 Johnson, Kendall and Roberts (JKR) extended the Hertz model to include adhesion effects.

2.2. Including adhesive forces: The JKR model

Adhesion plays an important role on the length scales we are interested in and hence it should be taken into account when small objects in contact are used. An extension of the Hertz theory taking account of surface forces was elaborated in 1971 by Johnson, Kendall and Roberts [26] and it has become well known as the JKR theory. Their basic assumption was to take into account the adhesive interaction only within the contact zone and neglect any interaction outside the contact zone (Fig. 1.4).

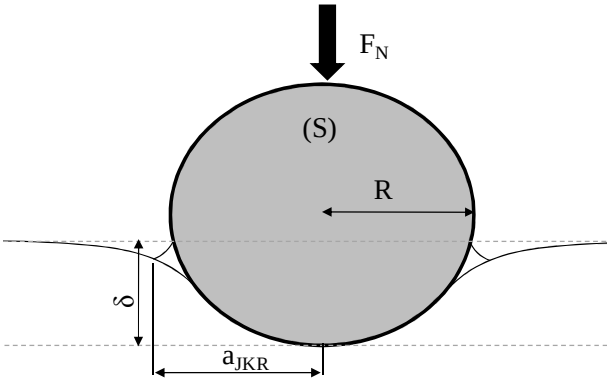

Figure 1.4: The JKR model for a rigid sphere (S) in contact with an elastic half space. The adhesion force considered in the JKR theory can be understood as an additional Hertzian force.

The JKR contact radius a and the JKR indentation depth δ are given as a function of the externally applied load F for an elastic sphere in contact with elastic half space as,

$$a = \left(\frac{3}{4}\frac{R^*}{E^*}\left[F_N + 3\pi R^*\gamma + \sqrt{6\pi R^*\gamma F_N + (3\pi R^*\gamma)^2}\right]\right)^{\frac{1}{3}} \qquad 1.20$$

$$\delta = \frac{a^2}{R^*} - \sqrt{\frac{2\pi a\gamma}{E^*}} \qquad 1.21$$

, where γ is the effective surface energy of adhesion of both surfaces [27]. In this case, they found a larger contact area compared to the contact area in the Hertz model,

$$A_R = \pi a^2 = \left(\frac{3}{4}\frac{\pi R^*}{E^*}\left[F_N + 3\pi R^*\gamma + \sqrt{6\pi R^*\gamma F_N + (3\pi R^*\gamma)^2}\right]\right)^{\frac{2}{3}} \qquad 1.22$$

By assuming the friction force is proportional to the real area of contact (as in Tabor theory) the previous equation will lead to a sub linear dependence of the friction force on the load. Furthermore, in the absence of surface forces ($\gamma = 0$) equations 1.20 and 1.21 reduce to the classical Hertz model (Eqs. 1.8 and 1.9). Furthermore, the JKR model predicts that the force needed to remove the particle (the pull-off force) from the contact is given as:

$$F_{PO}^{JKR} = -\frac{3}{2}\pi\gamma R^* \qquad 1.23$$

By adding an adhesive force to the Hertz model, the JKR theory is able to explain why contacts can be formed during the unloading cycle, also in the negative loading of one body against another one. However, the JKR approach of the contact of two elastic bodies is not right in every case, since it neglects the forces acting at the border of the contact area.

2.3. The Derjaguin-Muller-Toporov (DMT) model

The alternative thermodynamic approach by Derjaguin, Muller and Toporov (DMT) [28] assumes that the contact area does not change due to the attractive surface forces and remains the same as in the Hertz theory. In this model the attractive forces are assumed to act only outside of the contact area. Due to the involved assumptions, the JKR model is more suitable for compliant materials and the DMT model is more appropriate for rigid materials. In the DMT model the attractive force is simply added as an additional load to obtain the correct indentation depth and contact area from the Hertz theory. Therefore the equations for the contact radius and the indentation depth in the case of a sphere indenting a plane become

$$a = \left(\left(\frac{3R}{4E^*}\right)(F_N + 4\pi\gamma R^*)\right)^{\frac{1}{3}} \qquad 1.24$$

$$\delta = \frac{a^2}{R^*} \qquad 1.25$$

In the case of DMT, they obtained a area of contact given by

$$A_R = \pi a^2 = \left(\left(\frac{3\pi R}{4E^*}\right)(F_N + 4\pi\gamma R^*)\right)^{\frac{2}{3}} \qquad 1.26$$

Which once again if the friction force is proportional to the real area of contact (as in Tabor theory) equation 1.26 will lead to a sub linear dependence of the friction force on the load due to a finite value of the contact area at zero applied load, even though a smaller contact radius

than in the JKR case is obtained for the same adhesive force. The sphere-plane pull-off force can be expressed as,

$$F_{PO}^{DMT} = -2\pi\gamma R^{*} \qquad 1.27$$

By experimenting on hydrogen-terminated diamond (111)/tungsten carbide mono-asperity interface using UHV-AFM, Enachescu *et al. [29]* demonstrated in 1998 that the load dependence of the contact area for an extremely hard single asperity contact is perfectly described by the DMT continuum mechanics model. Since the diamond sample is slightly boron-doped and the tungsten-carbide tip is conductive, they were able to measure the local contact conductance as a function of applied load. The experiments provided an independent way of determining the contact area, which can be directly compared to the corresponding friction force.

The DMT model takes into account the surface forces outside the contact area but not the deformations due to these forces. Therefore, one might expect that the JKR model is more appropriate for the case of compliance contacts and high surface energies, whereas the DMT model should be better suited for the case of rigid contacts and low surface energies.

2.4. Maugis model

Maugis in 1992 formulated a somewhat complex description of sphere-flat mechanics [30, 31]. He derived based on the Dugdale [32] potential a set of analytical equations that describe the transition between the JKR and DMT limits. His model is more accurate in a way that one does not have to assume a particular limit for the materials properties.

In his model, Maugis introduces a parameter λ,

$$\lambda = 2\sigma_0 \sqrt[3]{\frac{9R}{16\pi\gamma E^{*2}}} \qquad 1.28$$

, where σ_0 is the maximum constraint and is equal to,

$$\sigma_0 = \frac{16}{9\sqrt{3}}\frac{\gamma}{\epsilon_0} \qquad 1.29$$

, ϵ_0 is the range of action of surface forces at an equilibrium distance.

Maugis expressed the contact area, the normal force, and the penetration depth, by a relation with the Maugis parameter λ and m, m = c/a the ratio of the width of the annular region (including adhesive zone) c to the radius of the contact area a

$$\frac{\lambda\bar{a}^2}{2}\left(\sqrt{m^2-1}+(m^2-2)\tan^{-1}\left(\sqrt{m^2-1}\right)\right) + \frac{4\lambda^2\bar{a}}{3}\left(\left(\sqrt{m^2-1}\right)\tan^{-1}\left(\sqrt{m^2-1}\right)-m+1\right)=1 \quad 1.30$$

$$\bar{F} = \bar{a}^3 - \lambda\bar{a}^2\left(\sqrt{m^2-1}+m^2\tan^{-1}\left(\sqrt{m^2-1}\right)\right) \quad 1.31$$

$$\bar{\delta} = \bar{a}^2 - \frac{4}{3}\bar{a}\lambda\sqrt{m^2-1} \quad 1.32$$

, where $\bar{a}, \bar{F}$ and $\bar{\delta}$ the normalized contact radius, force and the indentation depth which are defined as:

$$\bar{a} = a\left(\frac{\frac{4}{3}E^*}{\pi R^{*^2}\gamma}\right)^{\frac{1}{3}}, \qquad \overline{F_N} = \frac{F_N}{\pi R^*\gamma}, \qquad \text{and} \qquad \bar{\delta} = \delta\left(\frac{\frac{16}{9}E^{*^2}}{\pi^2 R^*\gamma^2}\right)^{\frac{1}{3}} \quad 1.33$$

When varying the parameter λ, it is found that the values of a, F_N and δ are in between the values of DMT model and the JKR model. For a large lambda, $\lambda \gg 3$, the Maugis equations approach those of JKR model, and the pull-off force goes to $-{}^3/_2\,\pi\gamma R^*$. For the limit of λ equals zero, $\lambda \ll 0.01$ Maugis equations approach those of DMT model and the pull-off force approaches $-2\pi\gamma R^*$. For the case of an Atomic Force Microscopy, applications show that in the case of ceramics and metals (rigid materials), the λ parameter is well below 1, and then the application of the DMT model is more suitable. For the case of polymer, λ is of the order of 1, we are in the field of Maugis transition. Finally, for rubber or elastomeric materials (compliant materials), λ is larger than 1, and the JKR model is more suitable.

In Figure 1.5 the different characteristics of the contact in function of the normalized force are represented for the models of Hertz, DMT, JKR, and Maugis.

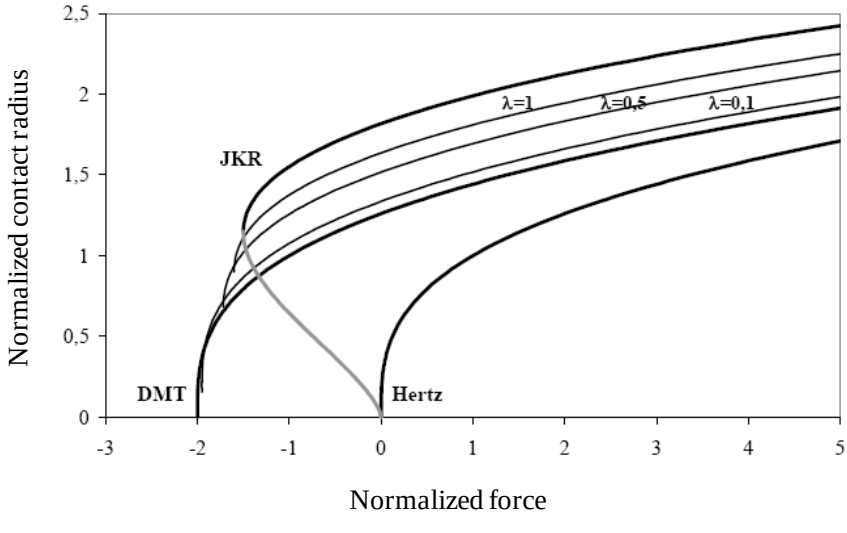

Figure 1.5: A) Normalized contact radius in function of the Normalized force. The Maugis transition is shown for different values of the transition parameter λ in between the DMT and JKR models. B) Normalized indentation depth in function of the Normalized force. The Maugis transition is also shown for different values of the transition parameter λ in between the DMT and JKR models.

2.5. Comparison of the models

The assumptions considered for a given approach could sometimes not exactly describe the materials in contact. We introduce Table. 1.1 and Table. 1.2 that show the assumptions of each of the models described above (Hertz, JKR, and DMT, Maugis) and the corresponding normalized equations that simplify the comparison.

Model	Assumptions	Normalized equations
Hertz	Linear elasticity No adhesion No friction	$\bar{F}_N = \bar{a}^3$ $\bar{\delta} = \bar{a}^2 = F_N^{\frac{2}{3}}$
JKR	Short-range surface forces acting within the contact area No friction	$\bar{F}_N = \bar{a}^3 - \bar{a}\sqrt{6\bar{a}}$ $\bar{\delta} = \bar{a}^2 - \frac{2}{3}\sqrt{6\bar{a}}$
DMT	Long-range surface forces acting outside the contact area No friction	$\bar{F}_N = \bar{a}^3 - 2$ $\bar{\delta} = \bar{a}^2$

Table 1.1: Model assumptions of the Hertz, JKR and DMT theories at a glance with the corresponding normalized equations.

Model	Hypothesis	Limitations
Hertz	No surface forces	Inappropriate when the load is small compared to surface forces
JKR	Surface forces act inside the contact. Formation of an adhesive neck	Underestimation of the load
DMT	Surface forces act outside of the contact	Underestimation of the contact area
Maugis	An attractive ring of variable width acts around the radius of contact	No simple analytical solution

Table 1.2: Comparison of the different hypothesis and limitations for the models of Hertz, JKR, DMT, and Maugis

Concluding from these previous models, it is clear that the single asperity or multi-asperity contact is still an opened question in tribology. Moreover, macroscopic tribological research can provide only empirical information about the frictional behavior of materials due to the lack of information about the interaction that are occurring at the interfaces. These interactions concern for example, the nature of the contact, its geometry, environmental conditions affecting the contact, etc. Therefore, comprehension of friction mechanisms is better established at a scale such as the nanoscale, which can unravel fundamental details about the contact between two bodies.

3. Nanotribology

3.1. Interactions in a nano-contact

The study of tip-surface interactions is an important link between the macroscopical and nanoscopical worlds. The impact of the surface forces is clearly noticeable in friction and adhesion with micro and nano contacts. In particular, the adhesion force between two objects can arise from a combination of different contributions such as the van der Waals force, electrostatic force, chemical bonding, and hydrogen bonding forces, capillary forces, and others. However, the intermolecular and surface forces are a wide subject that one can find in detail by reading Israelachvili [33] and Burnham [34]. We will just give a brief overview on three important forces which can be of relevant importance to our subject, these forces are:

- Electrostatic force;
- van der Waals force; and
- Capillary force

3.1.1. Electrostatic force

Electrostatic forces include those due to charges, image charges and dipoles. Since the time of the ancient Greeks it has been known that amber rubbed with fur would become "electrified" and attract small objects. In 1785 it was Charles A. Coulomb, who first quantitatively measured the electrical attraction and repulsion between charged objects. He formulated that the electrostatic force F_{el} is proportional to the product of the object charges (q_i) and inversely proportional to the square of the distance d between them:

$$F_{el} \propto \frac{q_1 q_2}{d^2} \qquad 1.34$$

For the case of an AFM, assuming a particle with radius R that has an electric potential $\boldsymbol{\varphi}$ relative to a grounded surface, the electrostatic force between the particle and the surface is given by [35]

$$F_{el} \approx 2\pi\varepsilon_0 R^2 \varphi^2 \left[\frac{1}{2(R+d)^2} - \frac{8R(R+d)}{[4(R+d)^2 - R^2]^2}\right] \qquad 1.35$$

, where d is the distance between the particle and the surface, and ε_0 is the permittivity constant. The first term in equation 1.35 describes the force between a grounded conducting

plane and a uniform charge distribution on a sphere. The higher-order terms describe polarization effects that result when the sphere is moved closer to the plane. Nevertheless, in the discussion of the interactions between a micro or nano particle and a surface, the electrostatic force when compared to the van der Waals and capillary forces could be neglected.

3.1.2. Van der Waals force (vdW)

Van der Waals (vdW) forces play a central role in all phenomena involving intermolecular forces. This force exists between any combination of molecules and surfaces, and it is always attractive i.e. tip and sample are attracted to one another, and is present regardless of the tip/surface setup used or the environmental conditions of the experiment. The van der Waals forces originate from three sources: dipole-dipole interactions (both atomic dipoles are free to rotate), dipole-induced dipole, and dipole induced-dipole induced interactions. These interactions are known respectively as the Keesom (orientation), Debye (induction), and the London (fluctuation) interactions[2].

Assuming that the potential, $W(d)$ between two atoms separated by a distance d is known, the force between them can be defined by the gradient of that potential

$$F(d) = -\nabla \mathrm{W}(d) \qquad 1.36$$

For the van der Waals interaction the potential is of the form:

$$W(d) = -\frac{C}{d^6} \qquad 1.37$$

, where C is the interaction constant as defined by London and is specific to the identity of the interacting atoms [36]. Hamaker [37] performed the integration of the interaction potential to calculate the total interaction between two macroscopic bodies. Hamaker used the following hypotheses in his derivation:

- Additive: the total interaction can be obtained by the pair-wise summation of the individual contributions.

2 With the exception of highly polar materials such as water, London dispersion interactions give the largest contribution to the van der Waals attraction.

- Continuous medium: the summation can be replaced by integration over the volumes of the interacting bodies assuming that each atom occupies a volume $d\Omega$ with a number density ρ.
- Uniform material properties: ρ and C are uniform over the volume of the bodies.

The total force between two arbitrarily shaped bodies is given by:

$$F_{vdw} = \rho_1 \rho_2 \int_{\Omega_2} \int_{\Omega_1} F(d)\, d\Omega_1 d\Omega_2 \qquad 1.38$$

, where $\rho_1$and ρ_2 are the number densities of molecules in the solid. Ω_1 and Ω_2 are the volumes of bodies 1 and 2 respectively.

The van der Waals force, $F_{vdw}(d)$ and van der Waals free energy, $S_{vdw}(d)$ for a spherical solid particle in contact with a surface can be described by Eq. 1.39 and Eq. 1.40, respectively [33].

$$F_{vdw}(d) = \frac{A_H R}{6d^2} \qquad 1.39$$

$$S_{vdw}(d) = -\frac{A_H R}{6d} \qquad 1.40$$

, where d is the distance between the particle and the surface; R is the radius of a spherical particle, A_H is Hamaker constant[3] and is given by:

$$A_H = \pi^2 C \rho_1 \rho_2 \qquad 1.41$$

Argento and French [38] derived an expression for the total van der Waals force between a conical tip of angle γ and radius R, and a plane.

The total force is given by:

$$F_{vdw} = \frac{A_H R^2 (1-\sin\gamma)(R\sin\gamma - d\sin\gamma - R - d)}{6d^2(R + d - \mathrm{Rsin}\,\gamma)^2} - \frac{A_H \tan\gamma [d\sin\gamma + R\sin\gamma + R\cos(2\gamma)]}{6\cos\gamma\,(R + d - \mathrm{Rsin}\,\gamma)^2} \qquad 1.42$$

3 The Hamaker constant describes the strength of the interactions between atoms and depends on material properties, it is explained in detail in ref 38. Argento, C. and R.H. French, Parametric tip model and force--distance relation for Hamaker constant determination from atomic force microscopy. Journal of Applied Physics, 1996. ***80****(11): p. 6081-6090.*

, where d is the tip-surface separation, calculation of the van der Waals contribution to the total tip-surface force requires only knowledge of γ, R and A_H; γ and R depend only on the tip-shape. The assumptions made in the derivation of this expression are the same used by Hamaker [37]. Since there is no geometric assumption in this derivation, the expression gives exactly the force on the probe if non-retarded van der Waals interactions are the only interactions present.

The van der Waals force between two media across a solvent medium (i.e. water) will be lower than the interaction across a vacuum medium. By applying the following Lifshitz theory, the appropriate Hamaker constant can be determined for a medium 1 interacting medium 2 across medium 3 [33].

$$\begin{aligned} A_{H\,total} &= A_{H_{v=0}} + A_{H_{v>0}} \\ &\approx \frac{3}{4}KT\left(\frac{\varepsilon_1-\varepsilon_3}{\varepsilon_1+\varepsilon_3}\right)^2 \\ &+ \frac{3hv_e}{8\sqrt{2}}\frac{(n_1^2-n_3^2)(n_2^2-n_3^2)}{(n_1^2+n_3^2)^{\frac{1}{2}}(n_2^2+n_3^2)^{\frac{1}{2}}\left[(n_1^2+n_3^2)^{\frac{1}{2}}+(n_2^2+n_3^2)^{\frac{1}{2}}\right]} \end{aligned} \qquad 1.43$$

, where $A_{H_{v=0}}$ is the Hamaker's constant due to Keesom and Debye interactions, $A_{H_{v>0}}$ is the Hamaker's constant due to London dispersion, ε_n is the static dielectric constant, v_e is the main electronic absorption frequency in the ultraviolet (UV) region n_n is the medium refractive index in the visible light region. However, for two identical mediums interacting across a medium, Eq. 1.43 reduces to,

$$\begin{aligned} A_{H\,total} &= A_{H_{v=0}} + A_{H_{v>0}} \\ &\approx \frac{3}{4}KT\left(\frac{\varepsilon_1-\varepsilon_3}{\varepsilon_1+\varepsilon_3}\right)^2 + \frac{3hv_e}{16\sqrt{2}}\frac{(n_1^2-n_3^2)^2}{(n_1^2+n_3^2)^{\frac{3}{2}}} \end{aligned} \qquad 1.44$$

3.1.3. Capillary force

When two surfaces are close together in the presence of a vapor, water (or any other liquid) may condense to form a liquid meniscus between the two surfaces [33]. The force caused by such a liquid meniscus arises from the Laplace pressure of the curved menisci. This force can be called capillary force. Moreover, this force may influence the contact between two solids, by affecting adhesion and friction forces, especially the static friction forces [39]. The capillary forces must be taken into account in studies of powders, soils, granular materials, and tribology [40-46].

The condensation process of the water vapor in the gaps and small cavities between surface asperities leads to the formation of capillaries that bind the neighboring surfaces (Fig. 1.6). For constant environmental conditions, the size of the capillary depends on the geometry and chemistry of the surfaces. Lord Kelvin proposed one of the first classical views of a capillary bridge. At equilibrium, the surface curvature of the meniscus is imposed by the Kelvin radius R_K:

$$\frac{1}{R_K} = \left(\frac{1}{R_1} + \frac{1}{R_2}\right) \qquad 1.45$$

, where R_1 and R_2 are the minimum and maximum curvature radius of the meniscus respectively (R_1 along the plane of the figure perpendicular to the solid surfaces, R_2 lies in the plane of figure parallel to the solid surfaces) (Fig. 1.6), the radii are taken as positive for convex curvatures and negative for concave curvatures. The Kelvin radius is connected with the relative vapor pressure by the following equation:

$$R_K = -\frac{\gamma_{LV}\Omega_L}{k_B T log(P/P_S)} \qquad 1.46$$

, where γ_{LV} is the surface tension[4], Ω_L is the molar volume, T is the temperature, and k_B is the Boltzmann constant, and the ratio of P the equilibrium on P_s the saturation water vapor pressure corresponds to the relative humidity RH in the case of water.

In the context of AFM measurements, the liquid deflects the cantilever towards the surface by acting as an attractive force on the AFM tip. The amount of this force can be derived from Laplace's equation. According to Pierre Simon de Laplace the pressure inside a liquid is modified over the atmospheric pressure by:

$$P_L = \gamma_{Lv}\left(\frac{1}{R_1} + \frac{1}{R_2}\right) \approx \frac{\gamma_{LV}}{R_K} \qquad 1.47$$

, where P_L is the Laplace pressure, when the meniscus increases in size, R_2 tends to infinity and R_1 tends to the Kelvin radius. The Laplace pressure acts on a wet area A_w that equals $\pi x_2^2 \cong 2\pi RZ$ (computed from Figure 1.6), where R is the radius of the AFM probe (Fig.

4 Surface tension is measured in N.m^{-1} and is defined, for example in the case of a liquid surface in equilibrium, as the force per unit length along a line perpendicular to the surface, necessary to cause the extension of this surface

1.6), the resulting capillary force is then $F_c = P_L A_w = 2\pi R z \left(\frac{\gamma_{LV}}{R_K}\right)$. The adhesion force corresponds to the capillary force F_c in a more general case, it is given by the equation [33]

$$F_c = \frac{2\pi R \gamma_{LV} (\cos\theta_P + \cos\theta_S)}{1 + d/z} \qquad 1.48$$

, where d is the separation between the sphere and the plane, θ_P and θ_S are respectively the contact angles of the sphere[5] (probe) and the flat surface. From equation 1.48 it is clear that the stronger capillary force arises from the condition of separation d = 0.

$$F_{c\,max} = 2\pi R \gamma_{LV} (\cos\theta_P + \cos\theta_S) \qquad 1.49$$

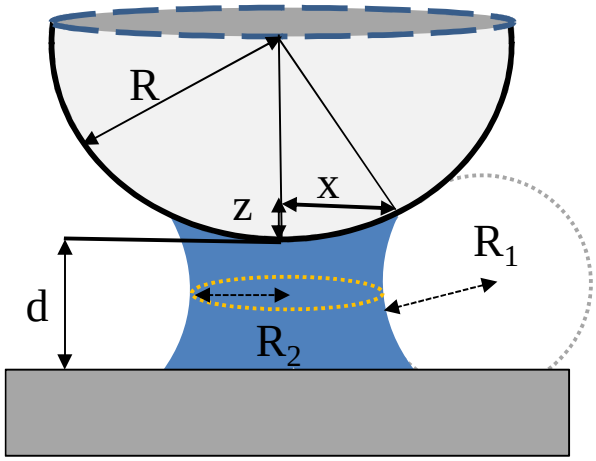

Figure 1.6: Capillary bridge between a sphere and a flat surface. R1 and R2 are the minimum and maximum curvature radius of the meniscus respectively (R1 along the plane of the figure perpendicular to the solid surfaces, R2 lies in the plane of figure parallel to the solid surfaces).

Measuring these forces at the nanoscale was not possible until techniques that can measure forces at the nanoscale were introduced.

5 In the case of water, for θ greater than 90°, one speaks about hydrophobic surface, whereas for θ smaller than 90°, the surface has a hydrophilic behavior, which means that the water molecules are more attracted to the surface than to themselves.

3.2. New approaches for investigations at the nanoscale

Over the past decade, significant advances in the development of experimental techniques as well as in theoretical methods have allowed us to gain further knowledge about frictional processes at the nanometer scale and even at the atomic scale. Observing what is going on at the nanoscale level is of crucial importance to understand what occurs at the macroscopic level for sliding. This wide expanding field of tribology is called "Nanotribology".
Extraordinary developments in experimental techniques over the past three decades have accelerated interest of researchers to study friction on the nanoscale.

The first apparatus for nanotribology research is the Surface Force Apparatus (SFA) invented by Tabor and Winterton [47] in 1969 to measure van der Waals forces in air or vacuum. The SFA can measure the interaction forces with resolutions up to the *nN* as a function of the mutual distance to an accuracy of about 3 Å, between two surfaces that are usually flexible and transparent sheets of mica. The SFA device was further developed in 1972 by Israelachivili and Tabor for the measurement of van der Waals dispersion forces in the range of 1.5 to 130 nm [48]. Furthermore, it was developed by Israelachvili and Adams for the measurement of forces between liquids and vapors [49]. A severe limitation of the Surface Force Apparatus is that the mica is the only surface that can be directly studied. There have been several approaches such as, evaporation of metal layers and oxides, plasma and UV treatments, etc., often in situ (adsorption of surfactants and polymers, grafting of ligands, etc.), to overcome this limitation and allow the use of different surfaces.

Furthermore, it has become a powerful tool to study nanotribological mechanisms on a wide number of systems such as, confined simple liquids, polymer melt and solutions, self-assembled surfactant and polymer layers. Recently the SFA has been used as an molecular tribometer to investigate the nanotribological behavior of self-assembled monolayer's (amine and phosphate) by Mazuyer et al. [50], and it has been modified by Israelachvili to study anisotropy in friction on polymer surfaces [FANAS-ICTP 2011, Trends in nanotribology]. Recent advances in the surface forces apparatus (SFA) technique can be found in [51].

Later in the 1980's two types of microscopes were invented: The Scanning Tunneling Microscope (STM) and the Atomic Force Microscope (AFM) [52]. These devices have gained more and more precision as the industry and the computer sciences evolved, to reach nowadays the atomic resolution and measure forces down to the nano-Newton. The invention in 1981 of the first Scanning Tunneling Microscope (STM) that was based on electron

tunneling between a small tip and a surface, provided the capability of imaging a solid surface with atomic resolution in three dimensions [53, 54], but was limited to the study of electrically conductive samples. The scientific community acknowledged this invention by awarding the Nobel Prize to its inventors, Binnig and Rohrer, in 1986. Few years later, in 1985, Binnig and Rohrer developed an Atomic Force Microscope (AFM) (Annex. 1) that was based on the principles of the STM but with resolving surface structures for non-conducting and conducting materials. The AFM belongs to the great family of Scanning Probe Microscope (SPM). It has the properties of surface imaging and surface force measuring down to the nano-scale. It can be used in different environments going from ultra high vacuum to liquids, to study any kinds of surface, including biological samples.

The advent of these scanning microscopes revolutionized the field of tribology. In recent years, other modifications of original STM and AFM were soon made to measure lateral forces by the use of the now known Friction (or Lateral) Force Microscopy (FFM; LFM) [55], This technique immediately gave rise to friction experiments between single asperity probes at forces of the order of a few nano-newton.

Furthermore, in order to achieve better resolution of the contact, a wide spread method has been lately realized by introducing and SPM into a Scanning Electron Microscope (SEM) [56-58] (Fig. 1.7). These kind of combined techniques allow the real time observation of a contact.

In this thesis, we will use the AFM technique.

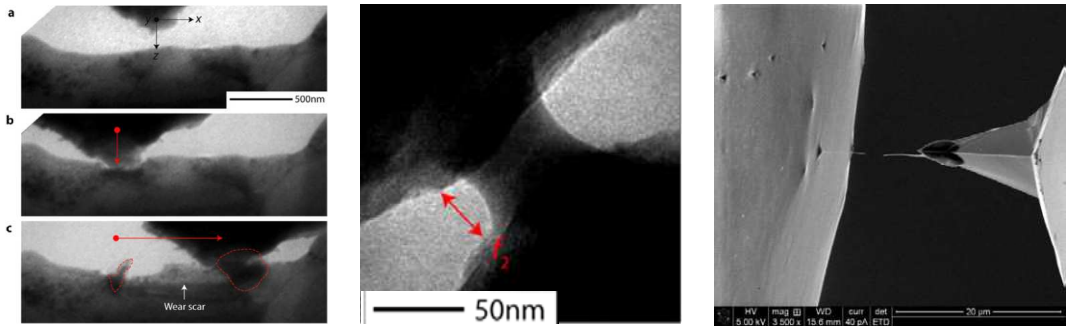

Figure 1.7: SEM images show real time observations of a probe in close contact to the surface from refs [56, 59].

3.3. Nanoscale friction

3.3.1. AFM friction force measurements

The AFM allows the measuring of the friction force at the nanoscale with a high resolution. In this case, the scan direction perpendicular to the fast scan axis is used. And the lateral bending (or twisting) of the cantilever occurs due to the acting friction forces, and this in turn induces a lateral movement of the laser beam on the detector. Thus both the vertical and the lateral bending of the cantilever are simultaneously measured. Moreover, the degree of torsion of the cantilever is a measure of surface friction caused by the lateral force exerted on the cantilever [60]. This mode of operation is called friction force microscopy (FFM) or lateral force microscopy (LFM).

A friction loop is formed by a scan cycle along one scan line in the forward and reverse direction (Fig. 1.8). Each direction of scan is defined by two regimes: A regime which shows a linear increase of the lateral force as function of the lateral piezo-actuator position, and corresponds to the static friction, where the tip sticks to the surface and the cantilever only twists, and a second regime where the lateral forces overcome the potential well characterized by the cantilever-tip-surface system. In this regime the tip starts to slide on the surface, and rests again when the scan direction is reversed. This process is then repeated in the reversed direction. The difference of the average values from trace and retrace corresponds to twice the mean friction force. In such a loop the sign of the friction force signal changes when the scan direction is reversed[6]. Information about the stiffness can be taken from the slope of the lateral force in a friction loop (Fig. 1.8) which is equal to the effective spring constant k_{eff}

$$k_{eff} = (k_C^{-1} + k_T^{-1})^{-1} \qquad 1.50$$

, where k_T is lateral stiffness of the tip, and k_C is the lateral stiffness of the cantilever. Furthermore, it is possible to deduce the energy dissipated by computing to the area enclosed by the loop.

6 The upper and lower parts of this so-called friction loop (Fig. 1.8) result from trace (scanning left) and retrace (scanning right back on the same line)

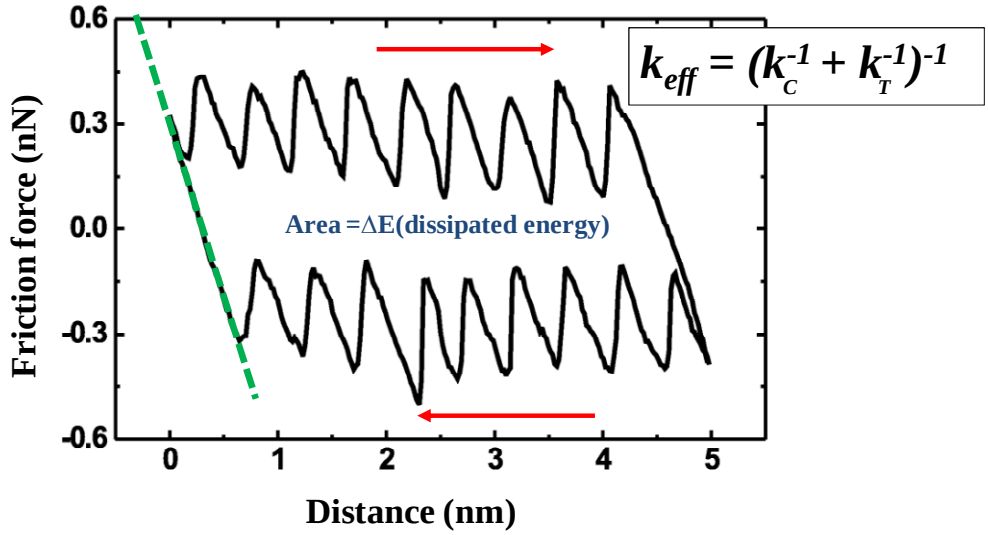

Figure 1.8: Example of the friction force obtained in an AFM friction force measurement [61]. The upper and lower parts of the so-called friction loop correspond to the trace and retrace scan, respectively. The difference between trace and retrace (average value) is proportional to the friction force. The slope in the first regime is the effective stiffness. The enclosed area corresponds to the dissipated energy.

3.3.2. Tomlinson model

Nanotribology is mostly concerned by the nature of the relative motion of two contacting bodies. Sliding one surface past another may result in a continuous movement, i.e. smooth sliding or a discontinuous movement, i.e. stick slip motion, where rather than sliding at a constant velocity, sliding occurs as a sequence of sticking and slipping or as an oscillation at a resonance frequency of the system. The term "stick slip" was coined by Bowden and Lebon (1939). During the stick phase, the friction force builds up to a certain value, and once a large enough force has been applied to overcome the static friction force, slip occurs at the interface.

The first experiments of friction force at the atomic scale were conducted by Mate et al., who carried out atomic resolution measurements using the Friction Force Microscopy [55]. He showed evidence of the stick-slip phenomena for experiments conducted on a graphite surface using a tungsten tip. Later, studies of atomic friction were continued e.g. [62, 63], that were highly inspired by the experiments of Mate *et al.*. A comprehensive study of the stick slip phenomena was conducted by Fujisawa *et al*, [64]. They studied the bending and torsional deformations of the microlever induced by horizontal applied force on different materials such as MoS_2 and NaF (100). By analyzing these signals, two paths were observed for the

movement of the tip on the surface. The authors showed that the tip prefers to jump to the nearest atom. So depending on the sliding direction of the tip with the crystallographic direction of the surface, the stick slip phenomena can follow a straight path (one dimension stick slip) or a zig-zag path (two dimension stick slip) (Fig. 1.9)

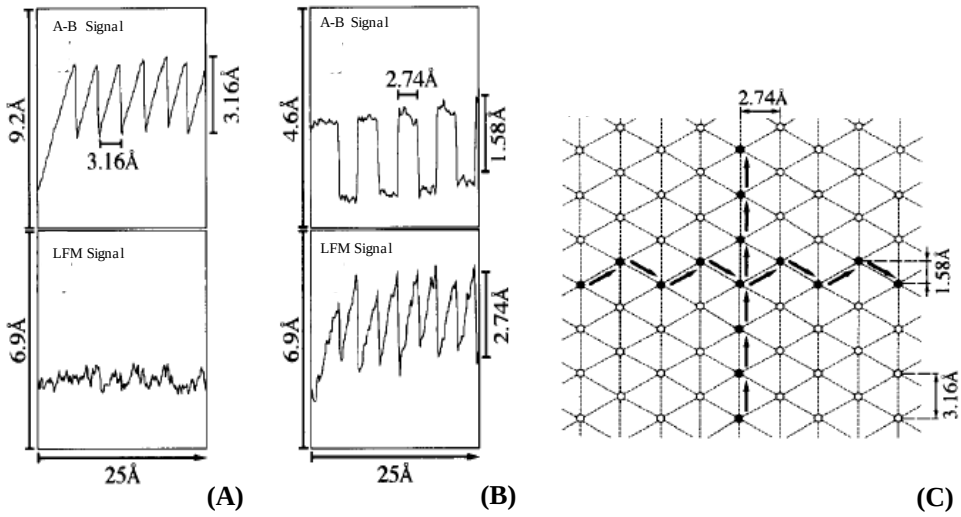

Figure 1.9: Bending and torsion of the cantilever depending on the scanning direction. Typical data for FX and FY (two-dimensional frictional force vector components (A) due to a single fast line scan along the cantilever, 1D stick-slip (along the Y direction). (B) Due to a single fast line scan across the cantilever, 2D stick-slip (along the X direction).

However, after more than seven decades the Prandtl-Tomlinson model still catches the essence of the more recent theories of friction. It is a simple model for friction that was developed by Prandtl (1928) and Tomlinson (1929), and is usually referred to as the Tomlinson model or the independent oscillator model. The model was introduced by G. A. Tomlinson in his paper entitled "A molecular theory of friction" [65]. It is a very simple and instructive mechanical model describing friction of single asperity contacts, and explaining already most of the phenomena occurring in friction such as the atomic stick and slip, the static and the dynamic friction.

The approach is based on the interaction between two surfaces in relative motion. We will describe in detail the simple friction mechanism for the case of one particle in the framework of the one-dimensional Tomlinson model. We consider a single atom (A) elastically attached to an isolated slider surface (1) via a spring of stiffness k; that is moved across another surface (2) that is represented by a periodic potential $C(x)$ (Fig. 1.10).

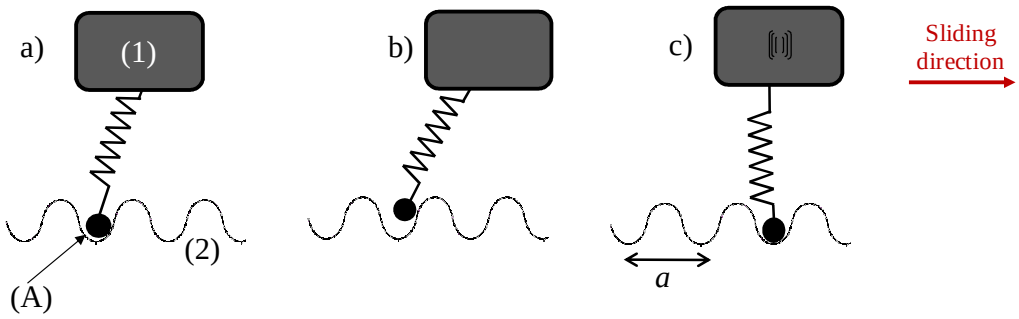

Figure 1.10: Schema of the Tomlinson model. The atom is attached by a spring to a support which moves in the x direction, the atom jumps from one minimum to the other.

As surface (1) slides, the force on the atom will increase (Fig. 1.10-b) until it gets so strong that the atom jumps to the next potential minimum (Fig. 1.10-c). During this transition, relaxation energy is dissipated via lattice vibrations of the upper body and finally via the generation of phonons.[7]

The system composed of the slider surface, the spring, and the surface can be represented as a cantilever of a AFM apparatus sliding on a surface. Let us apply the Prandtl–Tomlinson model to the example of an AFM tip sliding along a one dimensional periodic potential $Y(x)$ with amplitude Y_0:

$$Y(x) = -Y_0 \cos\left(\frac{2\pi x}{a}\right) \qquad 1.51$$

, where Y_0 is the peak to peak amplitude of the sinusoidal potential, and a is the periodicity of the surface lattice.

The tip is coupled to the cantilever via a spring of stiffness k. The position of the cantilever is denoted by x_0 and the tip position by x. When the tip is dragged along the surface lattice, the deformation of the spring is simply $(x - x_0)$. The velocity of the cantilever is given by V_0. Its coordinates will change according to $x_0 = V_0 t$, with t being the time. The total energy of the system for a cantilever moving at a constant velocity v along x becomes

$$Y(x) = -Y_0 \cos\left(\frac{2\pi x}{a}\right) + \frac{1}{2}K(x - x_0)^2 \qquad 1.52$$

7 In the Prandtl–Tomlinson model, this dissipation is described by a simple damping term that is proportional to the velocity of the atom.

$$Y(x) = -Y_0 \cos\left(\frac{2\pi x}{a}\right) + \frac{1}{2}K(x - V_0 t)^2 \qquad 1.53$$

Initially, the tip is located in the equilibrium position of local minimum that can be given by the condition where the first derivative of $Y(x)$ with respect to x is zero:

$$\frac{dY(x)}{dx} = \frac{2\pi Y_0}{a}\sin\left(\frac{2\pi x}{a}\right) + K(x - V_0 t) = 0 \qquad 1.54$$

For the beginning of one stick–slip cycle, we can use the approximation sin $x \approx x$ for small x. This leads to

$$\left(\frac{4\pi^2 Y_0}{a^2} + K\right)x - KV_0 t = 0 \qquad 1.55$$

The initial velocity of the tip V_{tip} can be calculated:

$$V_{tip} = \frac{dx}{dt} = \frac{V_0}{1+Q} \qquad with \qquad Q = \frac{4\pi^2 V_0}{Ka^2} \qquad 1.56$$

The coefficient Q is the ratio between the strength of the tip-sample interaction and elastic energy of the system [61]. Here the initial velocity of the tip V_{tip} is clearly lower than the velocity V_0 of the support. The critical position x^* at which the tip becomes unstable and gets ready to move to the next minimum takes place when the second derivative of the total energy with respect to x (acceleration) changes its sign, this will correspond exactly to the time t^* when the second derivative of the total energy with respect to x is zero:

$$\frac{d^2Y(x)}{d^2x} = \frac{4\pi^2 Y_0}{a^2}\cos\left(\frac{2\pi x^*}{a}\right) + K = 0 \qquad 1.57$$

This leads to:

$$x^* = \frac{a}{2\pi}\arccos\left(-\frac{1}{Q}\right) \qquad 1.58$$

This kind of movement is called stick-slip, and is expected when Q > 1, for example, when the system is not too stiff or the tip-surface interactions are strong enough to make the tip stick at its last position. Whereas in the other case were Q < 1, the tip has one equilibrium position at every moment, and the tip slides continuously.

The friction force is given by

$$F_F = -K(x - V_0 t) \qquad 1.59$$

from equation 1.54, we obtain the relation,

$$F_F = \frac{2\pi Y_0}{a} \sin\left(\frac{2\pi x}{a}\right) \qquad 1.60$$

This shows that the friction forces are maximum immediately before jumping, at the point where $x = {a}/{4}$,

$$F_F^{max} = \frac{2\pi Y_0}{a} \qquad 1.61$$

This gives a linear dependence of the friction force on the potential amplitude Y_0.

Velocity dependence

The jump of the tip through the energy profile from one minimum to the other is prevented by the energy barrier ΔE. Such a barrier decreases while sliding, and, when it becomes zero, the tip slips into the next equilibrium position, where a new sticking phase starts. In the above discussion of the Prandtl–Tomlinson model, we did not consider thermal motion, which corresponds to sliding at $T = 0$ *K*. In this case the tip does not jump until $\Delta E = 0$. In the case of a finite temperature *T*, the reaction rate theory suggests that the tip jumps from a minimum into the next one when the energy barrier a value of $\Delta E \approx k_B T$ (even if $\Delta E \neq 0$ the tip jumps). At a certain time t, the probability for the tip not to jump, p, is determined by:

$$\frac{dp}{dt} = f_0 exp\left(-\frac{\Delta E}{k_B T}\right) p(t) \qquad 1.62$$

, where f_0 is the characteristic lateral frequency of the system (i.e, lateral resonance frequency); In the attempt to explain the observed logarithmic dependence of the lateral force on the scan velocity between a silicon tip sliding on a NaCl (001) surface in UHV at a constant temperature, Gnecco *et al.*, showed that the physical origin of the velocity dependence can be understood within the Tomlinson model by assuming a linear dependence of the energy barrier with the increasing friction force [61]:

$$\Delta E = \tau(F_F^{max} - F_F) \qquad 1.63$$

where the slope τ, will depend on the interaction potential, when there is no lateral force (F_F = 0) the energy barrier is just the maximum possible value, namely Y_0, so we can say that τ is of the order of Y_0/F_{Fmax}. By substituting Eq. 1.63 in Eq. 1.53, a logarithmic dependence of friction force on velocity is obtained:

$$F_F = F_{F0} + \frac{k_B T}{\tau} \ln\left(\frac{V}{V_0}\right) \qquad 1.64$$

where F_{F0} is an offset depending on the applied load. The increase in friction force with velocity simply reflects the fact that at higher sliding speeds, the system has less time to overcome the activation barrier by thermal motion.

4. Recent experimental results on dynamic friction

The experimental results on friction for understanding the dependence of friction on the velocity were for a long time interpreted based on the Tomlinson model. In the proceeding we will overview that different experimental and somewhat distinct results were observed for the relation between the friction and the velocity, depending on the specified experimental conditions and the studied surface. To illustrate clearly this relation, we remind some of the most important results on velocity dependence of the friction.

4.1. Friction independent of the sliding velocity

The first measurement of friction with atomic resolution using friction force microscopy (FFM) was carried out by Mate et al. [55] they used a tungsten wire tip sliding on a Highly Oriented Pyrolytic Graphite (HOPG) surface at loads inferior to 10^{-4} N. They conducted measurements in ambient conditions and revealed little velocity dependence of the friction for scanning velocities between 0.004 μm/s and 0.4 μm/s. They used a model based on the sum of a periodic tip-surface force and a spring force for the tip motion to interpret there results.

In 1998 Zwörner et al conducted measurements on amorphous carbon, diamond and HOPG but over a wide range of velocities with the use of an AFM working in air and equipped with a silicon cantilever [66]. During the measurements the sliding velocities were varied between 0.02 mm/s and 24.4 mm/s, i.e. about 2 orders of magnitude was covered, with the application of normal loads ranging between 3.3 nN and 83.4 nN. It was found that under all the different experimental conditions and for all materials investigated, the friction force is constant. In fact, for velocities lower than 1 μm/s it was found that the friction force is independent of the

sliding velocity. Where for higher sliding velocities, a linear increase was numerically obtained with a theoretical model, and the obtained results regarding the behavior of the frictional forces were illustrated by a simple mechanical model based on the Tomlinson [65] and independent oscillator model [63, 67] which show that the frictional forces are independent of the sliding velocity as long as the slip movement of the tip is faster than the sliding velocity.

4.2. A power-law dependence of the friction on the sliding velocity

In 1997 by Gourdon et al. [68] conducted by the use of an AFM in air a study on a mica surface covered by lipid films with velocities ranging from 0.01 μm/s to 50 μm/s. They observed a linear increase of friction versus the scanning velocity. They reported a critical velocity value of 3.5 μm/s for which the linear increase of friction changes for a constant regime. This increase of the friction force with the sliding speed was attributed to a stick slip phenomena, and the transition at the critical velocity value (V = 3.5 μm/s) was assumed to be the point of changing from a stick to slip regime.

Further experiments conducted by Priolo et al. in 2003 [69] on a boric acid crystal (H_3BO_3) by the use of an AFM at constant relative humidity (RH = 40%) and at ambient temperature (30°) also showed a increase of the friction with the sliding velocity. They observed that for low velocities, inferior to 2 μm/s, a smooth non linear increase of the friction attributed to the predominance of stick forces. They suggested an athermal power-law dependence of atomic friction in the form V^{α} with $\alpha \approx 1.6$ for small scanning velocities [70], whereas a linear dependence is observed at higher velocities due to the predominance of viscosity. For these last studies, the behaviors were explained using an athermal Tomlinson model.

4.3. Friction force versus the sliding velocity variation - Slope change from increasing to decreasing

Most of the time, a logarithmic dependence has been found, but speculations involving an increase or a decrease of the friction force with the sliding velocity are still negotiable.

By the use of a Scanning Force Microscopy (SFM) equipped with a housing chamber, Optiz et al. performed experiments at different environmental conditions, to study the behavior of

the friction force as a function of load and the sliding velocity [71]. They studied friction by sliding a sharp silicon tip against a flat Si (100) sample, while changing the environmental condition from air to vacuum. During pump-down in the vacuum chamber housing the SFM, the behavior of friction as a function of the applied normal load and the sliding velocity undergoes a change. Three distinct friction regimes were found (Fig. 1.11): first regime at ambient condition, where the capillary force dominates, the friction versus the sliding velocity is represented by a negative slope as previously reported by Riedo et al. [72], second regime during pump-down, when the humidity is progressively removed, the slope changes to a positive value, they refer this to a residual water film remaining on the sample surface, that has a thickness of about 0.7 nm and correlates to a film composed of 2 ice-like water bilayers [73, 74]. In this regime, ordering effects of the ice-like bilayers strongly influence friction, leading to speculations that friction arises from the ‘‘pushing aside’’ of these bilayers by the sliding tip. This last behavior is typical for hydrophobic surfaces [71, 72]. In the third regime, after complete water desorption due to the combined effects of the vacuum and friction-induced desorption, only solid–solid contact remains, which exhibits the lowest friction of all the three friction regimes.

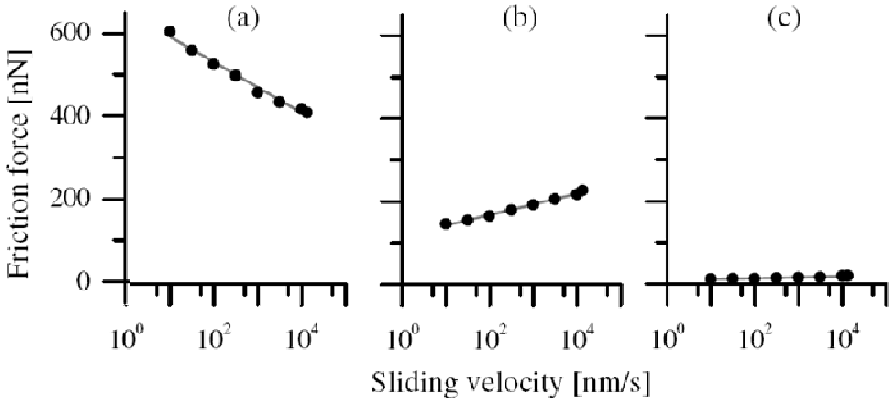

Figure 1.11: Variation of the friction force with the sliding velocity, and a change in the slope from a) where the capillary forces dominate in air to b) where ordering effects dominate during pump down humidity is progressively removed and c) where solid-solid contact remains. From ref [71].

Another recent study in 2006 by Chen et al. [75] reported AFM observations of friction dependency on velocity. For experiments conducted at ambient conditions and with a silicon

probe, they found that the friction decreases with the velocity for system possessing the potential to form cross-linked structures at the interface such as surfaces terminated with groups such as -OH, -COOH, and -NH_2 that are capable of forming networks of H-bonds. Whereas the opposite was found -friction increases with sliding velocity- for systems that are unable to form such networks, such as surfaces that are terminated with chemically saturated species, such as -O- (mica, dry SiO_2), and -CH_3, that are unable to form such networks.

The assumption that the decrease of friction with sliding velocity is attributed to the formation of water bridges is neglected by the authors in this case since the surfaces were very flat (root mean square roughness R_a < 0.3 nm), and they assumed that no capillary bridge can form except in a multiple asperity contact. Therefore to further ascertain that capillarity did not play a role in this case, a study was also done in UHV and the same resulting behavior was observed. The results have been explained in terms of disruption of the glassy H-bonds network domains at critical applied stress leading to slippage.

4.4. Logarithmic dependence of friction force on the sliding velocity

Bouhacina et al. in 1997 performed experiments with a AFM on surfaces of fairly rigid polymer layers grafted on silica [76]. They obtained a logarithmic increase in friction force with sliding velocity (for 0.1 µm/s < V < 60 µm/s) (Fig. 1.12). However, due to the fact that the experiments conducted in ambient conditions were not enough reproducible to extract a significant variation of the friction as function of the scanning velocity, the experiments were conducted in a glove box in which the ppm of O_2 and H_2O is controlled.[8] The increase was explained by a thermally-activated simple stress-modified Eyring model [77, 78]. Nevertheless, depending on the type of the contacting surfaces and the range of sliding velocities, deviations from the logarithmic dependence have been observed.

8 One part per million (ppm) denotes one part per 10^6 parts, This is equivalent to one drop of water diluted into 50 liters

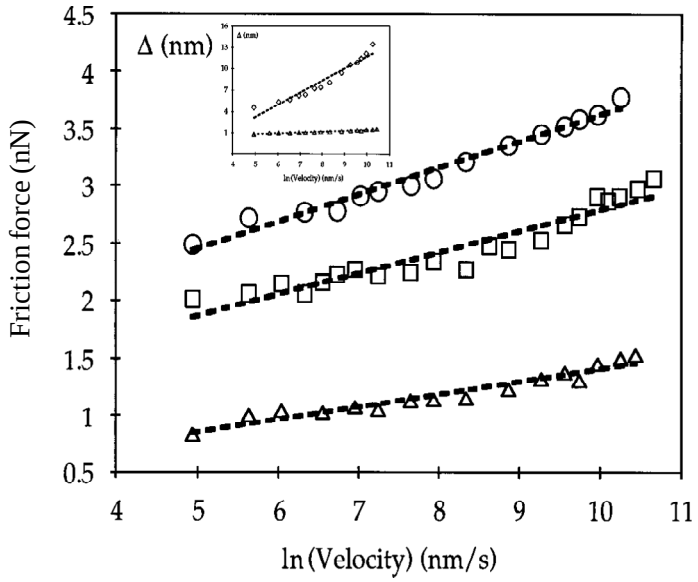

Figure 1.12: Fits and experimental data of friction versus tip velocity for the organo-silanes grafted on silica and probed with three cantilevers, each with corresponding stiffness being k1=0.58N/m (squares), k2=0.12N/m (triangles), and k3=0.38N/m (circles). The measurements were done at zero externally applied loads. Graph from ref [76].

In 2000, using a friction force microscope Gnecco et al. performed the first measurements related to the velocity dependence of atomic scale friction under UHV [61]. For a silicon tip, sliding on a NaCl (100) surface at low velocity ($V \leq 1$ µm/s), they obtained a increasing logarithmic dependence of the mean friction force on the velocity. The results were interpreted within a modified Tomlinson model, taking into account the effects of thermal activation.

In studies related to relative humidity (RH ≈ 35%-65%), experimental results obtained by *H. Liu et al.* using an oscillatory friction and adhesion tester [79] showed a logarithmic decrease in friction with the increasing velocity when a sapphire ball slides on a silicon wafer with native oxide layer [80]. Such dependence was also found for AFM tips sliding on hydrophilic CrN surfaces[9] by Riedo et al. (Fig. 1.13) [7]. They assumed that the decrease of the friction force with the increasing scanning velocity was attributed to the interruption of the development of the meniscus during sliding. Indeed, by considering the capillary

[9] *CrN samples are customarily used in hard coating technology, the CrN films have been deposited at temperatures of 500°C substrate temperature, which lead to contact angle of 45° 81. Hones, P., R. Sanjines, and F. Levy, Characterization of sputter-deposited chromium nitride thin films for hard coatings. Surface and Coatings Technology, 1997.* ***94-95****: p. 398-402.*

condensation between two rough surfaces during sliding, Riedo et al [7] suggested that when the tip faces the surface at a local position for longer contact times (lower sliding velocities) capillary bridges can form also between more distant asperities. For a contact area of diameter d, the residence time *t* is given by $t = x/V$ where *V* is the scanning velocity, and as sliding velocity is decreased, there is a continuous increase of the number of capillary bridges forming in the area of contact.

However, they both observed the contrary on hydrophobic surfaces such as partially hydrophobic diamond like carbon (DLC/Si) films [7, 82], where the capillary force does not play a dominant role [7, 80, 83]. *H. Liu et al* reported that friction force exhibits only a slight increase in the low velocity range (0.09 - 1.3 µm/s), and a significant increase in the range from 1.3 to 100 µm/s. This increase was attributed to higher velocities that lead to prolonged deflection of the spring, since asperity interaction occurs more frequently. The sapphire ball is not able to return to its initial position and thus resulting in higher friction. The experiments by Riedo et al. showed a positive slope for partially hydrophobic surfaces, whereas the slope was negative on partially hydrophilic surfaces (Fig. 1.13).

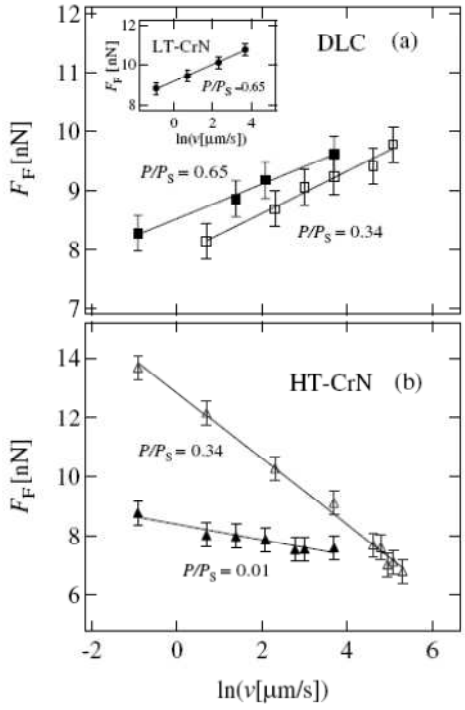

Figure 1.13:(a) Friction force as a function of sliding velocity for partially hydrophobic surfaces, at relative humidities P/PS = 0.34 and 0.65, (b) Friction force as a function of the sliding velocity for a partially hydrophilic surface (HT-CrN) at P/PS = 0.01 and 0.34. From ref [7].

They suggested that the overall friction force is given by superposition of the stick and slip related increase and the capillary condensation related decrease of friction with velocity. However, for atomically flat mica which is a hydrophilic surface, it was assumed that on this surface there is a mono-asperity contact in which no nucleation of the capillary meniscus can occur and the friction force increases with the sliding speed due to the domination of stick slip process. Nevertheless, the experiments by Riedo et al. showed that for all samples and humidities, a linear variation of the friction force with ln(V), which was in agreement with literature [8, 61, 76, 80, 83].

In addition to the logarithmic dependency of the friction force on the velocity also found by Riedo et al. [7, 83, 84], they found a critical velocity beyond which friction remains constant. This behavior was explained by the fact that thermal activation is more efficient at low velocity as it depends on the probability of transition between different equilibrium configurations.

From the overview of the experimental results mentioned in this section (1-4), one can summarize the variation of the friction force with the scanning velocity based on two main processes. On one hand, a time dependent process involving intermolecular forces, or mainly capillary forces based on a thermal activation of water bridges between the tip and the surface, leading to a logarithmic decrease of the friction force with the scanning velocity. Moreover, layers covering the surface and whose disorganization under the applied shear stress results in a decrease of the friction force once they do not have enough time to reorganize in a network. On the other hand, thermal activation involving vibrations that may excite a slipping process from one equilibrium position to the next one. For this kind of thermal activation, the increase of the velocity reduces the probability of transition between the different equilibrium positions leading to a logarithmic increase of the friction with the sliding velocity.

In addition to the logarithmic dependence that has been observed due to the thermal activated processes, few experimental studies have reported a proportional dependence of the friction on V^{β}, with β equal to 1 or 2/3 based on an athermal Tomlinson model. However, most of the results governing this approach have been done theoretically.

Most of the studies have been performed in environments where not all involved parameters are being controlled such as the temperature, and it becomes difficult to decide which process,

thermal or athermal, occurs in reality. In table 1.3 we present a summary of the main results mentioned for the dependence of friction force on the sliding velocity.

Authors	Setup	Friction vs Velocity	Model and note
Mate et al. [55]	FFM Tungsten wire tip Graphite surface Ambient conditions	Independence 0.004 µm/s < V < 0.4 µm/s $F_N < 10^{-4}N$	Similar to 1D Tomlinson model
Zworner et al. [66]	AFM Silicon cantilever Amorphous carbon, Diamond, and graphite In air	Independence 0.002 mm/s< V < 24.4mm/s 3.3 nN < F_N < 83.4 nN	Athermal 1D Tomlinson model
Gnecco et al. [61]	FFM silicon tip NaCl(100) surface UHV	FF ∝ ln V V ≤ 1 µm/s FN = 0.44 nN ; FN = 0.65 nN	Thermal 1D Tomlinson model
Prioli et al. [69]	Contact SFM Silicon nitride H3BO3 Ambient conditions Constant RH (40 %)	$F_F \propto V^{\beta}$, β≈1 for V> 2 µm/s $F_F \propto V^{\beta}$, β≈1.6 for V < 2 µm/s F_N = 100 nN	Athermal 2D Tomlinson model
Gourdon et al. [68]	AFM Silicon tip Lipid films on mica Ambient conditions	F_F increase versus sliding velocity 0.01 µm/s < V < 50 µm/s F_F independent of sliding velocity for V > 3.5 µm/s	Stick slip phenomena Slip regime V > 3.5µm/s
Opitz et al. [71]	SFM Silicon tip Flat Si (100) From air to vacuum	0.01 µm/s < V < 10 µm/s In air friction decreases During pump down friction begins to increase	Decrease due to capillary forces Increase due to residula water films remaining on the surface
Chen et al. [75]	AFM Surfaces having the potential of forming cross linked structures (H-bond networks) Surfaces where no such Networks are formed	logarithmic decrease of the friction with the scanning velocity logarithmic increase of the friction with the scanning velocity were no networks are formed	Disruption of the glassy H-bonds network domains
Bouhacina et al. [76]	AFM Si_3N_4 Grafted layers on silica Glove box	FF ∝ ln V 0.1 µm/s < V <60 µm/s FN = 0	Thermally activated processes

H. Liu et al. [80]	Oscillatory friction and Adhesion tester Sapphire ball slider Relative humidity (RH ≈ 35%-65%),	Logarithmic decrease in friction with the increasing velocity on hydrophilic surface. Slight logarithmic increase in the low velocity range (0.09 - 1.3 µm/s), and a significant increase in the range from 1.3 to 100 µm/s for hydrophobic surfaces	Decrease due to interruption of meniscus development during sliding Increase due to prolonged deflection of the spring,
Riedo *et al.* [7, 83]	AFM Nanotip Mica (hydrophilic) CrN (hydrophobic, hydrophilic) Ambient conditions	Logarithmic decrease in friction with the increasing velocity on hydrophilic surface. V = [0-200 µm/s] Logarithmic increase in friction with the increasing velocity for hydrophobic and atomically flat surfaces. V = [0-20 µm/s]	Thermally activated process

Table 1.3: Overview of the main results for the dependence of the friction force on the sliding velocity.

As discussed above, there are various experimental achievements that have shown a dependence of the friction force on the sliding velocity. Most of these achievements were explained by the Tomlinson model that was detailed previously, or by a thermally activated process. This thermally activated process is related to the presence of capillary condensation.
The presence of capillary condensation was also investigated by Fogden and White who extended the Hertz theory to analyze the elastic contact of a single sphere contacting a rigid flat surface [85]. They considered the effect of elasticity based on the Johnson-Kendall-Roberts (JKR) model for elastic deformation [26]. They neglected the effect of capillary pressure in the contact zone.
However, Maugis and Gauthier-Manuel [30, 31], achieved the model of Fogden and White in the case of a Derjaguin–Muller–Toporov (DMT) contact using the Maugis parameter λ, and they noted that the same problem can be treated in the Fogden and White model simply by replacing parameters featuring capillary adhesion such as the capillary radius P_k with c, their X_K with m, their Laplace pressure Δp with $-\sigma_0$ and $2r_K$ with δ_t, (these parameters are previously noted in part 2). Nevertheless, they found that, for rigid materials, the depression

inside the meniscus was too low to influence the geometry of the contact, which remains Hertzian [12]. The capillary force F_C acts as an extra load that adds to the applied load F_N as suggested by Derjaguin et al. [13]. The total applied load F_{tot} is then the sum of the applied load F_N, the capillary force F_C and other forces like for example the van der Waals force F_{vdW}. This capillary force has been proven experimentally to be contact time dependent [6], this is related to formation of the capillary meniscus which is a thermally activated process. In the following, we will highlight on the origins of the capillary meniscus and the mechanism behind there condensation.

5. Capillary condensation

5.1. From water molecules to capillary bridges

Water is the most abundant compound on Earth's surface, covering 70.9% of the Earth's surface, and is vital for all known forms of life [86]. Water exists as liquid at ambient conditions, but it often co-exists on Earth with its solid state, and gaseous state (water vapor).
The chemical formula of a molecule of water H_2O, also called dihydrogen oxide is composed of two hydrogen atoms covalently bonded to a single oxygen atom (Fig. 1.14-a). The hydrogen atoms at the tips and the oxygen atom at the vertex, they form an angle of 104.45° with bond size of the order of the angstrom (Å). This particular geometry and the higher electro negativity of the oxygen compared to the hydrogen, result in a polar nature of the water molecule. The oxygen end is partially negative and the hydrogen end is partially positive, because of this, the direction of the dipole moment points towards the oxygen. The charge differences cause water molecules to be attracted to each other (the relatively positive areas being attracted to the relatively negative areas). This attraction contributes to hydrogen bonding which is a relatively weak attraction compared to the covalent bonds within the water molecule itself, it is responsible for a number of physical properties of water, such as the relatively high melting and boiling point temperatures.
In liquid water, the charges are balanced in all directions, but at the surface, and due to the collective action of hydrogen bonds the molecules line up in a kind of surface film layer. The strong cohesion between water molecules gives rise to water surface tension. This can be seen when small quantities of water are placed onto adsorption-free surface, such as polyethylene or Teflon, and the water stays together as drops.

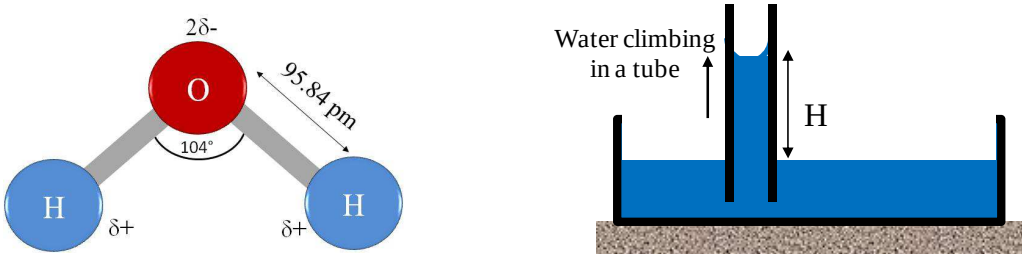

Figure 1.14: a) A single water molecule formed of 2 atoms of Hydrogen and 1 atom of Oxygen, b) the cohesion of water molecules causes water to climb in a tube.

Due to the interplay of the adhesion force and the surface tension, water exhibits capillary action whereby water rises into a narrow tube against the force of gravity. Water adheres to the inside wall of the tube and surface tension tends to straighten the surface causing a liquid surface rise and more water is pulled up through cohesion (Fig. 1.14-b). The process continues as the water flows up the tube until there is enough water such that gravity balances the Laplace pressure. This capillary action is not only present for macroscopic scales, but also at nanoscopic scales, for example the sand castle effects [3, 87]. The sand particles are held together by the capillary liquid bridges through capillary force that increase the cohesion between sand particles. It has also been proven that the particle surface roughness mainly controls the strength of the capillary bridges [44].

As mentioned previously, the capillary force was expressed geometrically according to the formation of the capillary bridge between two surfaces (Eq. 1.49). It was and for a long time, mainly expressed by equations of Young, Laplace and Kelvin. But humidity and granular media experiments showed that the formation of capillary bridges is time and humidity dependent [7, 44, 87], this explained for example the stronger stability of sandcastles when the wet sand was pressed for longer time. New models were developed that take into account the time and humidity dependency of the capillary force.

5.2. Kinetics of capillary condensation of water bridges

When two surfaces are brought close to each other in ambient air, the presence of humidity may lead to the formation of liquid bridges that will bind both surfaces. This process is known as capillary condensation whereby an under-saturated vapor can coexist with the liquid phase in small pores [88, 89]. This condensation process can have various effects in materials science applications such as Atomic Force Microscopy and Micromechanical systems [90,

91], and could also have drastic effects on granular media, modifying the friction and adhesion properties. The mechanism giving rise to the capillary condensation transition has been studied using the SFA by *Christenson* in 1994 [92]. However the kinetics of the capillary condensation is very poorly understood. Measurements of the kinetics of capillary condensation were conducted by the use of a surface force apparatus (SFA) for the first time by *M. Kohonen et al*. They investigated the growth rate of a liquid meniscus after the nucleation in an almost saturated water pressure at 25°C temperature and at humidities typically 99 %. They found a growth rate between 0.5 to 2 nm/s for a menisci growing from 20 to 60 nm [93]. The authors used a model based on Langmuir's theory of the diffusion-limited growth of atmospheric water droplets to explain their results [94].

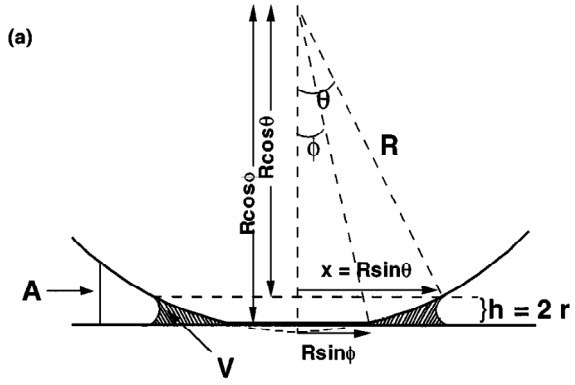

Figure 1.15: Schematic cross section of the surfaces in the equivalent sphere-on-a-flat-surface configuration in adhesive contact with a condensed annulus. R is the radius of curvature of the surfaces, h is the surface separation at the liquid-vapor interface of the condensate (≈2r, twice the radius of curvature of the interface), x = R sinθ is the radius of the annular condensate, and R sinΦ is the radius of the flattened contact zone, Fig from ref [93].

They considered a hydrophilic contact between a sphere and a flat surface illustrated in Figure 1.15. The adsorption from the vapor phase gives rise to thin films (of thickness ≈ 3 nm) on each surface which are squeezed out from between the surfaces when they jump into contact from a separation of approximately 20 nm [92, 95]. The initial value of r (the radius of curvature of the interface) in the subsequent growth of the liquid annulus by capillary condensation is determined by the volume of liquid squeezed out from between the surfaces, and varies between the different liquids and different *S* values. The area of the annular shell at a distance *x* was proposed to be $A = 2\pi x\,[R\cos\Phi - (R^2\text{-}x^2)^{1/2}]$ outside of the liquid condensate and the volume of the annulus is $\Omega \approx 4\pi R r^2$. Introducing the rate of change in the mass of

the liquid condensate Q, then from a simple diffusion theory and assuming a steady state has been reached

$$dc = \frac{Qdx}{\emptyset A} \qquad 1.65$$

where c is the concentration (mass per unit volume) of the vapor at x, and $\emptyset$ is the diffusion coefficient, at the liquid-vapor interface at $x = a$ where the pressure P_a can be calculated by the Kelvin equation and at a far point $x = b$ where the pressure P_b is equal to the vapor pressure of the chamber P, now integrating equation (1.65) between the two points a and b and converting the concentration to pressure units will give:

$$P_b - P_a = \frac{QR_gT}{\emptyset M_w}\int_a^b \frac{dx}{A} \qquad 1.66$$

where R_g is the gas constant, T is the temperature, and M_w is the molecular weight. If r is the radius of curvature at the liquid vapor interface, the rate change Q is given by:

$$Q = \rho\left(\frac{d\Omega}{dr}\right) \times \left(\frac{dr}{dt}\right) \qquad 1.67$$

Finally by substituting equation 1.67 in equation 1.66 and executing the integration one gets,

$$\frac{dr}{dt} = \frac{DM_wP_s}{R_gT\rho}\, G(r;R,\Phi)\left[\ln\frac{P}{P_s} - \exp\frac{\gamma_{LV}\Omega_L}{k_BTr}\right] \qquad 1.68$$

where the ratio of P the effective on P_s the saturation water vapor pressure corresponds to the relative humidity RH, here $G(r;R,\Phi)$ is a function of r and the measured geometric parameters R and Φ, The actual form of the function $G(r;R,\Phi)$ depends on the choice of the upper limit of the integral in equation 1.66; however, the results of integrating equation 1.66 are insensitive to this choice, provided x = b is chosen large enough (a convenient choice is $b = R$ the radius of curvature of the surfaces).

It appears that the simple model described above provides a reasonable prediction of the time scale over which the condensates reach their equilibrium sizes, at least for nonpolar liquids. However, the model gave consistently larger condensation times. Especially in the case of water which displays the largest deviations, the theoretical and observed initial rates of growth differ by a factor of 10, and this was attributed to the effect of dissolution of inorganic material from the surfaces.

Moreover, many models regarding the kinetics of capillary condensation were introduced and one of the first and most interesting was presented by Bocquet et al. in 1988 [44]. In which they have studied the effect of resting time on the angle of first avalanche of a granular system of small spherical glass beads contained in a rotating drum. A logarithmic behavior was observed for the ageing of a maximum static angle. Ageing was not observed for beads with a diameter superior than 0.5 mm, except at very large humidities. They concluded that the humidity played a crucial role in the ageing of the avalanche angle and that it was related to the condensation of small liquid bridges between the beads.

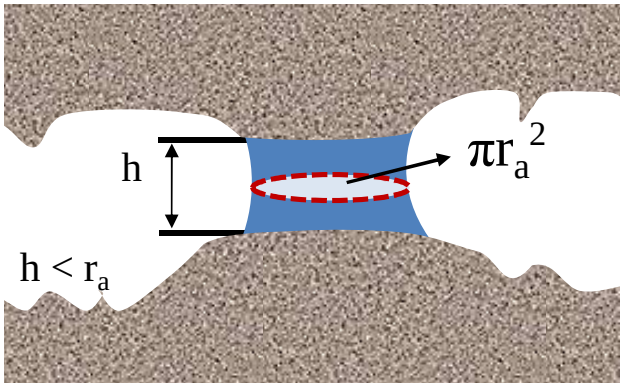

Figure 1.16: Schematic representation of a capillary bridge between rough surfaces.

The developed model was based on the thermally activated nucleation process of liquid bridges. Bocquet et al. considered a contact of two solid surfaces in an unsaturated vapor environment. At certain places of the contact where the separation is too small, at the interstices, capillary condensation should occur (Fig. 1.16). To start the condensing process of a volume Ω of unsaturated vapor surrounding the contact to capillary water, to pass over surface defects constraining the meniscus growth [96], a free energy cost has to be overcome, it is the threshold energy barrier ΔE, and is given by

$$\Delta E \approx k_B T \ln\left(\frac{P_s}{P}\right) \rho \Omega \qquad 1.69$$

where the ratio of P the vapor pressure over P_s the saturated water pressure corresponds to the relative humidity, T is the temperature, ρ the liquid density, and k_B is the Boltzmann constant. The energy barrier ΔE can be influenced by local chemical heterogeneities, roughness or asperities of the surfaces [44, 97, 98]. By assuming that the contact is formed between two rough surfaces, the asperities are distant by a height h, the nucleation of a

capillary bridge occurs at this point and has a volume of nucleation $\Omega = h\pi r_a^2$, where r_a is radius of the capillary bridge formed. Considering a nucleation process to commence, based on the law of Arrhenius[10] it is possible to calculate the time *t* needed to condense a bridge of height *h*

$$t(h) = t_A exp\left(\frac{\Delta E}{k_B T}\right) \qquad 1.70$$

where t_A is the time estimated for the formation of one liquid layer. Later, Riedo et al. have experimentally estimated the time needed to condense the liquid layer to be of 25 µs [7]. And more recently, measurements of temperature and time-dependent nanoscopic frictional forces have shown that the growth of the nucleation times varies exponentially with 1/T obeying the law of Arrhenius [99].

After a given time *t*, the bridges with activation time inferior or equal to *t* will have condensed. This sets the level for a maximum gap height h_{max} for which a bridge had the time to grow:

$$h_{max}(t) = \frac{\ln\left({}^{t}/_{t_A}\right)}{\ln\left({}^{P_s}/_{P}\right)\pi r_a^2 \rho} \qquad 1.71$$

Recently Sirghi et al. [100] reported that when the meniscus is in thermodynamic equilibrium with the water vapor, the capillary bridge has a limit roughly equal to twice the Kelvin radius to remain formed.

When the contact is assumed to be between rough surfaces, only a fraction $f(t)$ is indeed formed at a given time from the total number of the liquid bridges, in particular this is due to the height distribution where only a part of the contact is wetted. This fraction $f(t)$ is proportional to the number of activated bridges:

$$f(t) \approx {}^{h_{max}}/_{\xi} = \frac{\ln\left({}^{t}/_{t_A}\right)}{\ln\left({}^{P_s}/_{P}\right)\pi r_a^2 \rho} \qquad 1.72$$

where ξ is the full width of distribution of the interstitial heights between the surfaces.

As previously mentioned (section 1-3.1), the capillary force originating from a formed capillary bridge in between a sphere and a flat surface is:

[10] *The Arrhenius law gives a dependence of the rate constant t of chemical process on the temperature* T *and the activation energy*

$$F_c = 2\pi R\gamma_{LV}(\cos\theta_P + \cos\theta_S) \quad 1.73$$

An adhesion force $F_{adh,}$ the sum of the capillary force F_c, due to the Laplace pressure of the water meniscus forming between the tip and the sample is given by:

$$F_{adh} = f(t)F_C \quad 1.74$$

Following from the model developed by Bocquet et al, one should keep in notice that it is limited for the application of rough surfaces, and the logarithmic dependency of the adhesion force on humidity and time. These results were recently confirmed by D'Amour et al [101].

5.3. Humidity dependence of a capillary force

Relative humidity is the process that governs the extent of water adsorption on surfaces from the surrounding atmosphere, numerous reports have suggested that the adhesion forces and in particular the capillary forces can be influenced by the change in relative humidity. They report increase and decrease or even no variation of the adhesion force with an increase in the humidity. In this section, we will report a comprehensive review of the literature concerning the influence of the relative humidity on the capillary meniscus and the adhesion force.

At the end of the 1920s, the first insight concerning influence of humidity on the force between surfaces was noted by Stone, W. [102]. He made a qualitative study of the adhesion between pairs of glass spheres (diameter 1 - 2 mm) suspended on silk threads. After comparison, he noticed that the adhesion for experiments conducted in dry air is lower than that at ambient air, and this was attributed to the presence of adsorbed water.

Tomlinson [103, 104] studied adhesion between pairs of quartz fibers and pairs of glass spheres by measuring the deflection of the fibers, he studied freshly formed surfaces in vacuum, and noted that on exposure to the atmosphere, the surfaces lost most of their adhesion due accumulation of contaminating matter from the air, reducing the surface energy of the solid surfaces. The striking difference in the trend between the observations of Tomlinson and Stone no doubt stem from Tomlinson's use of freshly prepared surfaces in vacuum, which will maintain much higher surface energies compared with the dry air conditions of Stone.

McFarlane and Tabor [8] also conducted a more systematic study of the influence of relative humidity on the adhesive forces. They studied the interaction between a spherical glass bead

and a glass plate using a pendulum technique similar to that of Tomlinson [103]. In their system they observed that the adhesion was negligible at low RH values, only showing a notable increase at an RH of around 80%. This increase was shown to correspond closely to a notable increase in experimental values for the adsorbed film thickness of water on glass.

In the 1960s and early 1970s, Zimon studied the influence of the humidity on the adhesion force between glass spheres coated on to flat glass surfaces [105]. He obtained two variations for the adhesion force, he noted a slight increase in the range of RH = 5 - 50%, and an increase of the adhesion for humidities above 50%. As a conclusion Zimon suggested that the capillary forces are more dominant at higher humidities, and this was interpreted by McFarlane and Tabor's assumption about the domination of capillary forces once the asperities are attached by fully formed capillary bridges.

After introducing SPMs and especially the AFM, investigation of adhesion forces was more interesting and efficient since it allowed sensitive measurements at the nanoscale of inter-atomic and surface forces more accurately. Many reports showed that the force between a AFM tip and a hydrophilic surfaces is dependent on humidity [106-110].

The AFM was employed by Sugawara et al., to measure adhesion between a standard Si_3N_4 probe tip measured and a mica surface [111]. They operated under ultrahigh vacuum (UHV) conditions and under ambient pressure with relative humidities between 23% and 65%. Their data revealed a smooth monotonic increase in adhesion with increasing humidity. The increase was in agreement with the experimental results done with a glass sphere of radius several millimeters [14]. The adhesion increase was said to be related to the water films adsorbed on the surfaces.

In 2006 Jones *et al*. conducted by using an AFM, a thorough study of the adhesion force between a flat hydrophilic glass sphere of 20 µm radius interacting with a naturally hydrophilic oxidized silicon wafer [112]. The adhesion force increases monotonically with relative humidity, a variation which was reversible over the range 5 - 90% RH (Fig. 1.17-a). This increase was related to the capillary meniscus theory.

M. Farshchi et al. by employing the AFM the influence of the humidity on the adhesion force for hydrophilic and hydrophobic surfaces [109]. For hydrophilic surfaces the adhesion force either showed continuous increase or a maximum value with the humidity increase. An example is shown in Figure 1.17-b for a contact between a micro-fabricated silicon nitride tip and a hydrophilic silicon wafer surface. The adhesion force first increases, reaches a maximum at 70% relative humidity, and then decreases again. However these were assumed as tendencies. The increase at low humidity in both cases is an indication of roughness.

Moreover, no significant dependence of the adhesion force on humidity was observed for hydrophobic surfaces such as HOPG. This agrees with previous results, where a significant influence of humidity was observed on the adhesion between hydrophilic surfaces, while hydrophobic surfaces showed no dependency [108, 113, 114].

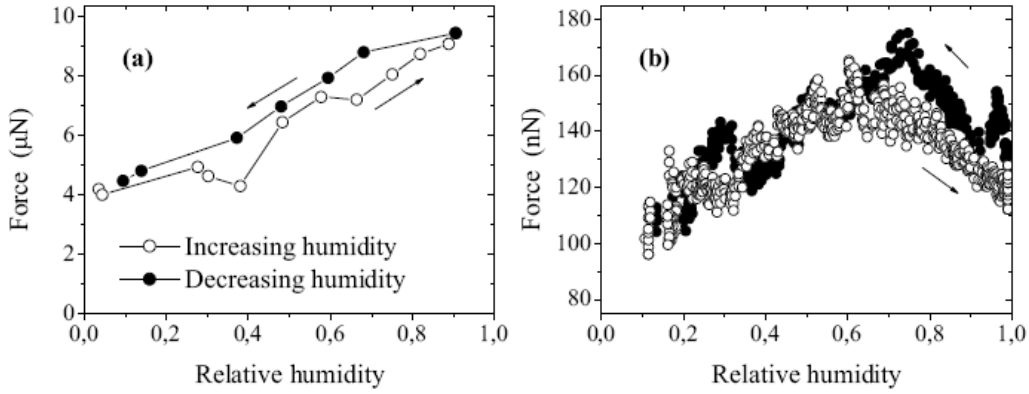

Figure 1.17: Adhesion force versus relative humidity curves. (a) A hydrophilic glass sphere of 20 mm radius interacting with a naturally oxidized silicon wafer as measured by AFM (ref [112]), (b) Force between a microfabricated silicon nitride AFM tip and a silicon wafer (ref [109]).

The different dependencies of adhesion force versus humidity can be explained by the presence of the meniscus force, which depends also on the roughness of the contacting surfaces. Slight changes in the tip or sample roughness can change the meniscus force significantly. We will report an overview of literature that has related variation of the capillary force to change in surface roughness.

5.4. Roughness dependence of a capillary force

Surface roughness has a huge influence on many important physical phenomena such as contact mechanics, adhesion and friction. For example, experiments have shown that a substrate with a root-mean-square (rms) roughness of the order ~ 1μm can completely remove the adhesion between a rubber ball and a substrate, while nanoscale roughness will remove the adhesion between most hard solids, e.g., metals and minerals; this is the reason why adhesion is usually not observed in most macroscopic phenomena [115].

It is important to investigate the effects of surface roughness on capillary force, because surfaces are usually rough on the 1 nm scale, and surface roughness can critically influence

the capillary force [116, 117], since the contact angle will change from a rough surface to a smooth one [118-124]. Several authors take roughness into account by introducing a single asperity [109, 110, 125, 126]. Halsey and Levine [3] extended this approach to describe interacting spheres by discriminating three regimes: In the asperity regime, for low relative vapor pressure and thus small liquid volumes, only one capillary bridge is formed at the outmost asperity, and since the asperity has a small radius of curvature, the capillary force will be low. In the roughness regime, for intermediate vapor pressure, the adhesion force shows a linear dependence on the added volume of fluid, in agreement with the principal result of Hornbaker et al. [87]. In this regime more and more capillary bridges are formed, and the roughness dominates. To quantify the capillary force, the force of one asperity is either multiplied by the number of asperities or a distribution of asperities is assumed [72, 127, 128]. And the spherical regime, at high vapor pressure, the menisci merge into one continuous capillary bridge; the overall radius of the bridges dominates the total capillary forces, and the surface roughness will no longer play a significant role.

Jang et al. [129] investigated how the capillary force that arises from the nanoscale liquid bridge in a AFM is influenced by atomic scale roughness of the contacting surfaces by using Monte Carlo simulations. They varied the humidity from 0 to 80 % and found that at low humidities, even a slight change in roughness of the tip or surface (less than 0.6 nm roughness value) leads to a drastic difference in the pull-off force. Whereas when humidity approaches 80 %, the roughness effect diminishes but never goes away.

6. Conclusion

In this first chapter, we have glanced over the friction phenomena from how it originated beginning from the macroscopic scale to the atomic level. The monoasperity in the cases of adhesive and non-adhesive contact was reviewed and dependence of the friction force on the real area of contact and on the load in each case was stated. A fundamental description of the forces acting on the contact between a tip and a surface was mentioned with the focus being given to the capillary forces that results from the formed liquid bridges, and two mechanisms responsible for the formation of the capillary bridges were discussed, the nucleation process and the meniscus growth process. Finally a brief historical overview of some experimental results obtained for the study of the friction force versus the sliding velocity, and the various trend obtained. Nevertheless, friction at the nanoscale and how it varies with the sliding

velocity has become a very strong and expanding study, which has grasped the attention of many researchers, but is still far from being well understood.

Chapter 2. The Circular AFM Mode

The Atomic Force Microscopy (AFM) offers interesting opportunities for the measurement of normal and lateral forces with a high resolution and at the nanometer scale. However, acquiring knowledge at the nanoscale at a broader range than that obtainable with a commercial AFM necessitates the development of additional technical characteristics that allow performing measurements with a higher accuracy and on a stationary state. In this chapter we will introduce a modification of the original AFM, by which we develop a new mode to address the issue of the limitations encountered with the conventional AFM. The implementation and the possible application fields of this mode will also be discussed.

1. Motivation

Over the years, for the sake of expanding and improving the measurement capabilities of the Atomic Force Microscopy, researchers have introduced and proposed various modifications to the basic technique. However experimental procedures are still subjected to limitations and challenges that hinder their accuracy.

One main limitation is due to the back and forth movement of the probe when performing lateral or normal force acquisition that results in the halt of the displacement when the probe reaches its limit of displacement in one direction and needs to invert its scanning direction. The halt in the displacement will result in the evolution of the contact between the probe and the sample. For instance, when the contact between a hydrophilic probe and a hydrophilic surface is at rest for an interval of time of a few milliseconds [99], a water meniscus between the probe and the sample can form as previously mentioned (see section 1-5). This can be detrimental to lateral force measurements, as the tip-sample contact undergoes two contradictory situations: One during the rest periods where capillary condensation leads to an increase of the meniscus size and thus leading to an increase of the capillary force and the normal load applied to the probe, and another during the sliding period, where the sliding

disturbs the formation of the meniscus and could lead to its vanishing [130, 131] a net decrease of the normal applied load to the probe. This can also be detrimental to adhesion force measurements as it is accepted that adhesion force measurements are contact time dependent due capillary condensation (see section 1-5.2). Consequently, the measurements are performed in a non-stationary state.

The nanoscale probe/sample interaction may also evolve significantly due to plastic flow, or viscoelasticity during these rest periods [7, 132, 133]. The back and forth motion results also in strong changes in some probe-sample interactions, for example, shear stress in the case of imaging or nanotribological measurements and that occurs when the probe rests and inverts its sliding direction. It is also not possible to reach high and constant velocity values that are comparable to realistic velocities of displacement of the contacts in nano or micro devices (MEMs, hard disks…). Nevertheless, in all these cases, a non-stationary state is encountered during scanning. In addition it is not possible with the commercial AFM to measure adhesion forces while the probe is sliding.

Therefore, to do this, and to overcome the previous obstacles encountered with the conventional AFM setup, we developed an original AFM setup in the purpose of conducting experimental procedures with high accuracy and in a stationary state (by eliminating the commercial AFM limitations). The implementation is based on generating a circular motion of the AFM probe relative to the plane of the surface to get a continuous motion with no rest periods. Moreover, this mode can be combined to other modes as force-distance spectrum (which will be known as “Force mode” throughout the thesis).

2. Circular mode Implementation

The Circular AFM mode is an innovative mode [5, 134] in which the motion of the probe is a circular motion relative to the surface. The circular motion of the probe is generated by the application of voltages to the AFM piezo-actuator that drives the probe or sample stage depending if the AFM is a scanned sample AFM or a scanned tip AFM. The applied signals act on the ceramics of the piezo-actuator causing them to expand or contract.

In this thesis, the Circular mode has been implemented on an original AFM (DI 3100 Veeco - coupled to a nanoscope controller V). The Circular mode was obtained by combining a sinusoidal voltage signal in the [-X, X] direction of the scanner, and a sinusoidal voltage signal shifted by $\pi/2$ in the [-Y, Y] direction of the scanner (Fig. 2.1).

$$U_X = U\cos\omega t \quad 2.1$$

$$U_Y = U\sin\omega t \quad 2.2$$

$$U_{-X} = -U_X \quad 2.3$$

$$U_{-Y} = -U_Y \quad 2.4$$

, where U is the voltage amplitude and ω is the angular frequency.

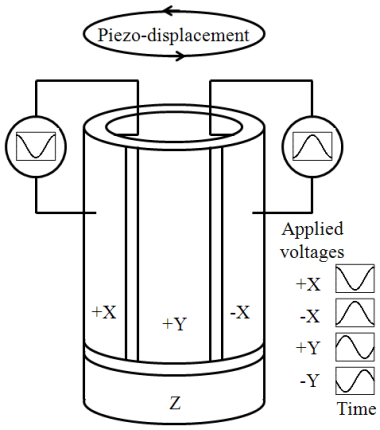

Figure 2.1: Applied voltage to the piezoelectric scanner as a function of time to generate a circular displacement. Cosine (cos) and sine (sin) voltages are applied to the X and Y electrodes. The opposite voltages are applied to the –X and –Y electrodes.

The voltage signals can be produced and controlled by a Digital-to-Analog Converter (DAC) device, a lock-in-amplifier, or a sinusoidal tension generator coupled with a dephasor. The voltage signals are injected to the AFM scanner through a Signal Access Module (SAMs BOX from Veeco). Figure 2.2 represents the general implementation principle of the Circular AFM mode to the AFM.

The implementation of the Circular mode (Fig. 2.2) necessitates:

- A computer with a card (A) that permits generating digital phase shift between X and Y voltage signals, and a software that allows controlling and varying the amplitude and the frequency of the generated signals according to the required (circular) movement.

- A Digital-to-Analog Converter (DAC) (B), an electronic device that converts the generated digital voltage to an analogical voltage that is input to the AFM controller through a SAMs box (D) to control piezo-actuator signals.

- A voltage inverter (C) that permits to generate inverted signals –X and -Y.

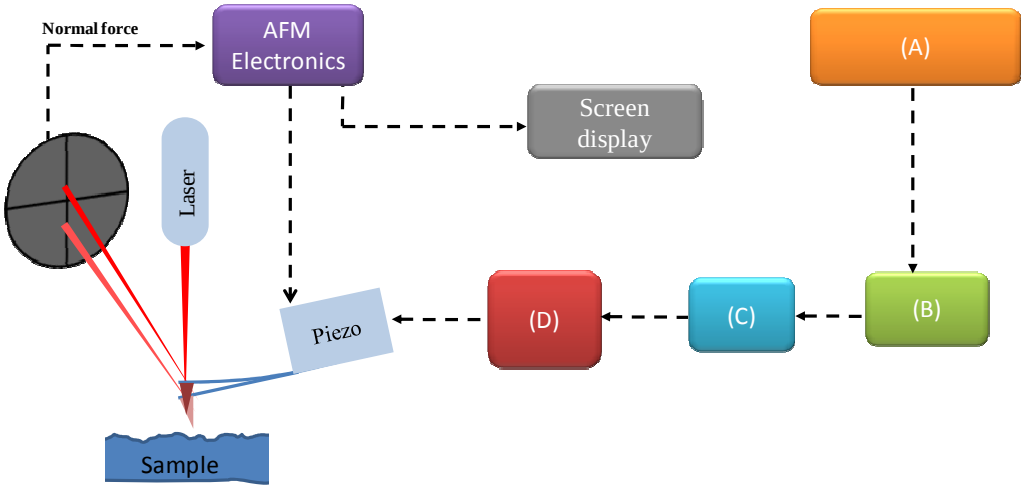

Figure 2.2: Schema representing the implementation of the Circular mode to the AFM. A) The Computer, B) Digital-to-Analog Converter (DAC), C) voltage inverter, D) signal access module (SAM).

3. Circular motion parameters

The Circular mode offers two parameters of control to regulate the velocity of the probes displacement, the voltage amplitude U which sets the radius R of the circular movement, and the voltage angular frequency ω which defines the interval of time needed to make a complete circle. The scanning velocity V is given by the following equation:

$$V = R\omega \qquad 2.5$$

The value of the radius of the circle is calculated based on the displacement of the piezo-actuator to the relative voltage signals applied to it. Our AFM is equipped with a piezo scanner (G scanner) that covers a full displacement range of 110 µm when applying a 440 V signal. In the linear range of the piezo-actuator, depending on the value of the voltage signals

applied the radius of the circle R can be calculated based on a simple mathematical method as in the following:

$$R(\mu m) = \frac{Piezo\ full\ range\ displacement(\mu m) \times applied\ voltage\ (V)}{2 \times Piezo\ full\ range\ voltage\ signal\ (V)} \qquad 2.6$$

Based on the previous equations for the velocity and the diameter, we present in table 2.1 some calculated values of the radii that were achieved at different frequencies with the Circular mode:

Frequency 100 Hz		
Voltage (V)	Radius (µm)	Velocity (µm/s)
0.1	0.0125	7.85
0.5	0.0625	39.25
1	0.125	78.5
2	0.25	157
3	0.375	235.5
4	0.5	314
5	0.625	392.5
6	0.75	471
7	0.875	549.5
8	1	628
9	1.125	706.5
10	1.25	785

Frequency 50 Hz		
Voltage (V)	Radius (µm)	Velocity (µm/s)
0.1	0.0125	3.925
0.5	0.0625	19.625
1	0.125	39.25
2	0.25	78.5
3	0.375	117.75
4	0.5	157
5	0.625	196.25
6	0.75	235.5
7	0.875	274.75
8	1	314
9	1.125	353.25
10	1.25	392.5

Table 2.1: Values of the radius and velocity at various applied voltages and at different scanning frequencies 100 Hz (left) and (right) 50 Hz.

It is worth noticing that for the same radius value the velocity of the probe at 100 Hz is double the velocity at 50 Hz. This clarifies that the velocity can be increased not only by increasing the applied voltage (radius) but also by increasing the frequency of sliding motion.
The radius of the circular motion is a key parameter for our experiments. Indeed, to obtain a sliding motion of the probe, the radius of the circle should be larger than the contact radius of the area formed between the probe and the sample. The contact radius can be determined from the Hertz theory (1-2.1) and could be estimated to be in the range of 2-3 nm in the case of a nanoscale contact for friction measurements conducted on a gold surface (Young modulus of the gold is about 79 GPa), by using a probe of 40 nm radius and under the effect of a classical applied load of 60 nN.
In our experiments, the radius of the circular motion varies in the range of 9 nm to 1.25 µm that is far from the contact 2-3 nm radius estimated by the Hertz theory in realistic conditions. This is confirmed in Figure 2.3 from which we can clearly see the circles obtained by wearing with the Circular mode a gallium arsenide surface.

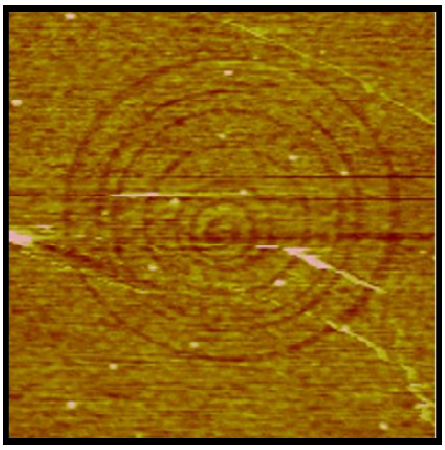

Figure 2.3: 5 µm × 5 µm topographic contact mode image of the circular imprints obtained with the Circular mode at different sliding velocity on a gallium arsenide surface (GaAs), with a silicon nitride tip ($R \approx 40$ nm) and normal cantilever stiffness ($k_N = 0.3$ N/m).

Finally, it is worth mentioning that the circular displacement could be easily implemented in a commercial SPM since one has access to the internal signals of the piezo-actuator. Technically, the commercial SPMs just require a minor software modification for implementing the Circular mode. Moreover, the Circular mode could be employed either with an open-loop or close-loop system, however for the close-loop system the implementation of

the Circular mode necessitates technical modifications of the SPM. The Circular mode on a close-loop system has not been tested.

4. Circular motion in the horizontal plane of the sample

Using the Circular mode at high sliding velocity could be challenging on rough surfaces as the servo loop is not able to correct the deviations of the cantilever at high scanning frequencies. Therefore, conducting experiments with the Circular mode on surfaces with low roughness is easier as no servo loop is required to maintain a constant load while scanning the sample However, if no servo loop is applied there remains a problem related to the tilt of the sample surface, which may lead to deviation of the circular motion of the probe out of the plane the sample. Therefore, by mounting the sample on a micromechanical table (Thorlabs - GN2 - Small Dual-Axis Goniometer, 1/2" Point of Rotation (Fig. 2.4) it can be tilted until the sample surface is perfectly parallel to the horizontal piezo-actuator displacement.

Figure 2.4: Micro mechanical table (Small Dual-Axis Goniometer), employed for adjusting the tilt of the surface in order to have the tip perpendicular to the horizontal plane of the surface.

The adjustment of the tilt is carried out simply by performing scans at a 0° scan angle along the [-X, X] direction of the scanner, and at a 90° scan angle along the [-Y, Y] direction. This shows, by the use of the offset parameter from the real time plane fit offered by the Nanoscope AFM software, the angle of the inclination of the surface (Fig. 2.5).

To insure that the surface is not tilted or bumped in the region were the experiments are conducted, we choose the scan size of the calibration process larger than the maximum circular displacement of the probe (diameter of the circle) used in the experiment (Fig. 2.5).

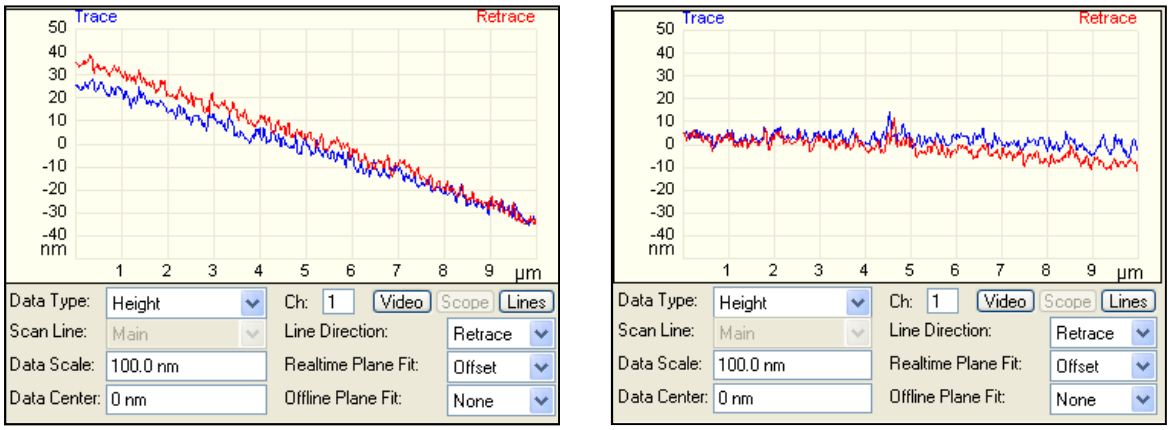

Figure 2.5: Image that represents the inclination angle of the surface during scanning a) before adjusting the micromechanical table b) after adjusting the micromechanical table, were the tip is perpendicular to the plane of the surface.

5. Advantages of the Circular mode

A benefit of the Circular AFM mode is the continuous and constant scanning motion, which allows avoiding inconveniences caused by the rest periods of the probe resulting from the conventional back and forth scanning mode (see section 1-5). Therefore, the Circular mode offers the opportunity to perform measurements in a stationary state.

It also offers advantages such as the possibility to generate high sliding velocities when no servo loop is required to maintain a quasi-constant load. For instance, in our AFM (Dimension 3100, Nanoscope V from Veeco, USA), the horizontal resonance frequency of our piezo-actuator (G scanner) is about 450 Hz. It is technically possible to scan at this frequency and generate at a full-scale scan (110 µm), velocities higher than 100,000 µm/s. The velocities reached with the Circular mode are typically three orders of magnitude higher than scanning velocities generated with the conventional AFM, and are comparable to realistic velocities in macro, micro or nano devices. Collecting data with a high resolution at these realistic velocities offers new opportunities for investigating velocity dependent properties such as friction or wear (at the nanoscale). However, it is not certain if operating under these conditions (high displacements at high frequencies) may or may not damage the piezo-actuators. In our particular operating conditions, the voltage amplitude is limited to 10 V and the frequency is set to 100 Hz leading to displacement velocity of about 1200 µm/s.

Moreover, for an open-loop AFM system, the Circular mode necessitates a far less complicated method for calibrating the piezo-actuator displacement. Indeed, in classical AFM scanning, back and forth scans are realized in the so-called fast scan direction. These consecutive scans are slightly shifted perpendicular to the fast scan direction (called the slow scan direction) and are added one by one to form the image. Because of the non linearity and creep of the piezo-actuator, the voltages applied on the two directions of the piezo-actuator follow a complex equation that requires the calibration of three parameters to generate a voltage function that conducts to a linear scan [135]. In particular, the full calibration of the G scanner (used in our D3100 AFM) requires the calibration of fourteen parameters that are determined through a relatively long and complex calibration.
However, when using the Circular mode, there are no more fast and low scanning directions. The voltage sent to the piezo-actuator is sinusoidal with respect to time for the two horizontal directions. One should then only consider the non-linearity of the scanner sensitivity for each direction leading to a simpler and reliable piezo-actuator calibration. Practically, the calibration of the piezo-actuator for obtaining an accurate circular motion of the probe can be easily realized using two different methods.

1) The first method is the classical calibration method that requires the use of a reference sample such as a calibration grid. In this case, we propose to impose sinusoidal voltages of various amplitudes in either the X or Y direction and to measure the resulting displacement. This method is mostly adapted for low frequency displacements, as an effective servo-loop is required to generate the “height” signal.

2) The second method consists in measuring the circular track resulting from wear or plastic deformation obtained with the Circular mode at a fixed amplitude and frequency. This last method is particularly interesting as it is simple, fast and reliable even if, it is less accurate than the conventional method, due to the error source on the width of the track. This method is especially adapted when the piezo-actuator is used at high frequencies since the servo-loop is generally not efficient at these frequencies. Figure 2.6 clearly shows the evidence of a circular track due to wear generated with the circular motion. Obviously, this method is damaging for both the sample and the probe.

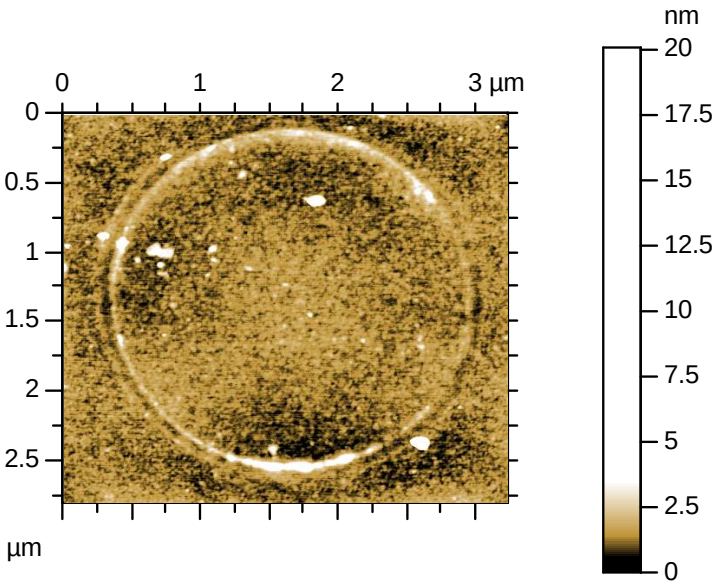

Figure 2.6: Calibration method: Contact AFM topographic image of a gallium arsenide (GaAs) thin film surface (image size: 3 µm × 3 µm). The circular track in the image is created by the circular displacement of the probe relative to the sample in using the Circular mode at a sliding velocity of 1000 µm/s for three consecutive minutes, under a load of 80 nN.

Finally, another interesting feature of the Circular mode is that along with the possibility of combining the Circular mode to the classical modes, as adhesion force mode or friction force mode, consequently, it is possible to measure simultaneously adhesion forces or friction forces while the relative probe/sample displacement is circular.

All the above advantages are determining in physics for quantitative measurements at a local scale i) that require stationary state conditions, ii) that require realistic high velocity displacements or iii) that require adhesion or friction force measurements while the probe is sliding. Such advantages of the Circular mode can have an impact in metrological aspect of nanotribology, nanoadhesion, or in probing properties at the nanoscale.

The main characteristics of the Circular mode are summarized and are compared with the conventional modes in table 2.2.

Item	Circular mode	Back-and-forth mode
Actuating the scanner	• In both directions: sinusoidal voltages, no harmonics • Easy to achieve constant velocities whatever the frequency • Fast calibration process • Smooth and constant scanning • No stop periods (excepted stick-slip), accelerations and decelerations • Easily achievable stationary state	• In the fast scanning frequency quasi triangle voltage, many harmonics • Difficult to achieve displacements at constant velocities especially at high frequencies • Time-consuming calibration process • Strong inversion of scanning direction two times a line • Stop periods, accelerations and decelerations occur at inversion • Unachievable stationary state due to stop periods and inversions of the motion direction
Coupling with other modes	Both modes could be: • Combined with LFM mode, but back and forth conventional mode allows acquiring friction loops to achieve local friction measurements, whereas Circular mode allows measuring friction force at a constant and continuous sliding velocity (servo-loop should inactive) • Combined with force spectrum but this combination is not implemented in commercial AFM • Combined with others SPM modes: STM, SNOM, contact AFM, Tapping mode, etc…	

Table 2.2: A comparison between the characteristics of the conventional mode and the circular AFM mode.

6. Applications of the Circular mode

Wear can be defined as a process in which interaction of the surfaces or bounding faces of a solid with its working environment results in dimensional loss of the solid. A serious issue is that wear rate tends to depend strongly on the magnitude of the loading force, leading to a

dramatic variation of the wear rate as the sliding conditions change. However, for different operating conditions (materials, geometry, roughness, humidity…) and sliding velocities, wear is dominated by different wear mechanisms such as delamination, fatigue, seizure, or surface cracks [136, 137]. Furthermore, wear at the nanometer scale is generally a slow process that results in low depth wear tracks that are difficult to measure. The advantage in achieving high sliding velocities with the Circular mode makes it possible to investigate the evidence of wear at the nanoscale. Indeed, the probe slides over the same distance with less time than in the case of using classical AFM mode, resulting in a faster wear process. For example, an experiment conducted on a gallium arsenide sample with a silicon nitride contact probe (radius R ≈ 40nm, stiffness k_N = 0.3 N/nm)), at a load of 80 nN and a sliding velocity of 1000 µm/s requires 3 minutes to generate a track, which is about 0.5 nm in depth (Fig. 2.7). However, the equivalent experiment when conducted with a conventional AFM at a frequency of 10 Hz needs fifteen minutes. This duration is generally too long to prevent any drift of the piezo-actuators that disturbs the measurements.

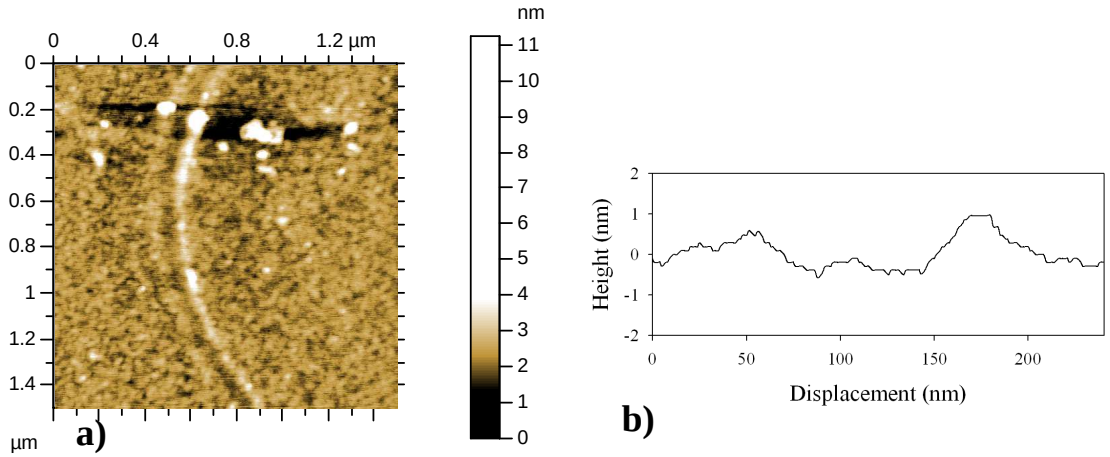

Figure 2.7: Imprints with the Circular mode on a Gallium arsenide (GaAs), analyzed by mountains digital surf Software. The Imprints result from experiments performed with a silicon nitride contact (stiffness k_N = 0.3 N/m) probe at a humidity of RH = 45% (a) Magnified image of the track generated by the circular motion for 3 consecutive minutes, under a load of 80 nN at a sliding velocity of 1000 µm/s. (b) Profile showing the depth of the track.

The well-defined wear track generated by the Circular AFM mode can be used to determine an Archard coefficient that was introduced by Holm and Archard. This coefficient relates the

volume worn per unit sliding distance, to the load, and the indentation hardness. The equation is given by:

$$\Omega = BLD/H \qquad 2.7$$

, where Ω is the total volume worn, D is the sliding distance, L is the load, B represents the Archard coefficient, and H defines the hardness of the contacting surfaces.

The same experiment as the previous one was performed but with a silicon probe (higher stiffness k_N = 5 N/m), the experiment was conducted at a sliding velocity of 1000 µm/s, and Figure 2.8 shows obviously that the silicon probe is easily worn contrary to the silicon nitride probe. Figure 2.8-a, b look the same because the probe is self imaging in this case.

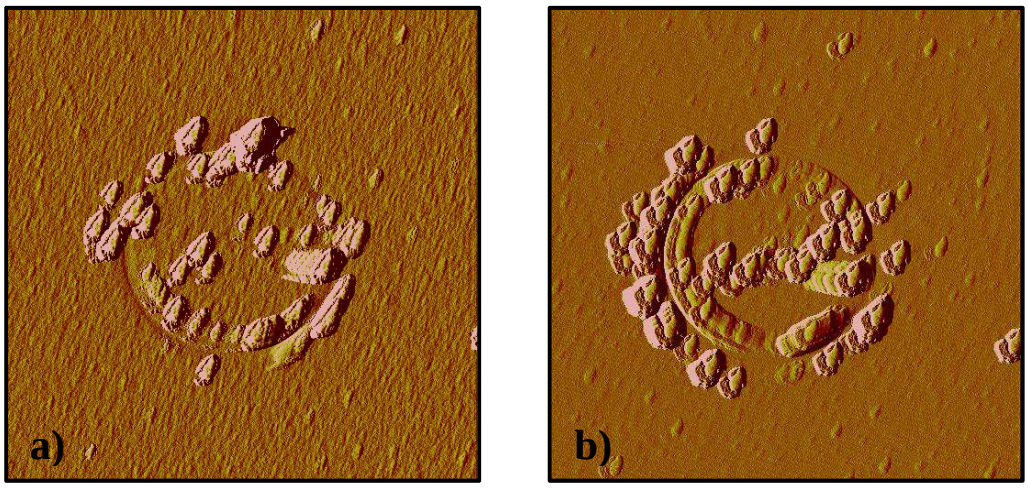

Figure 2.8: 5 µm × 5 µm topographic images (with a tapping tip) of a Titanium surface, circular imprints resulting from performing experiments with a tapping tip (stiffness k_N = 5 N/m) at a humidity of RH = 42% , clearly show wear of the tip a) for a 10 sec sliding motion b) for a extra 20 sec.

In a more general way, the Circular mode could be employed for changing quickly the surface properties that can be modified by the probe-sample interactions. As examples, i) circular features generated by wear tracks, lithography, oxidation or any modifications of the physical surface properties (magnetic, electrostatic…) could be employed for data storage, or ii) the Circular mode could be employed to polish surfaces or for machining surfaces by wear, by combining the Circular mode with a translation displacement. It is possible to generate easily

and rapidly surface features of any forms by this process by using abrasive probes such as diamond coated probe.

Finally, the Circular mode is a useful and profitable tool in other nanoscale applications such as: nanotechnology, nanopolishing, nanolithography, biotechnology, nanoadhesion and nanotribology etc (Annex. 2).

7. Conclusion

In this chapter we highlighted why experimenting with the commercial AFM for investigating at the nanoscale can have some limitations that drastically affect the contact between the probe and the sample. Limitations such as the back and forth displacement of the probe that leads to rest periods allowing the contact to evolve, the limited sliding velocity range, etc. As a result no stationary state and high sliding velocity are attainable. Therefore we implemented our newly developed circular AFM mode that helps overcome the limitations encountered with the commercial AFM. The Circular mode gives high sliding velocities, a constant and continuous sliding motion, combining the mode to other classical modes (force mode) etc.

In the following chapters, we will show that the Circular mode is a powerful tool to get new insights in friction mechanisms at the nanoscale.

Chapter 3. Velocity dependence of adhesion in a sliding nanometer-sized contact – A Circular mode study

Capillary adhesion acts as an additional normal load in a sliding nanometer-sized contact therefore it plays an indirect role in friction mechanisms (section 1-4). In particular, some authors [7, 71, 76, 80, 83] *have attributed the logarithmic decrease of the friction forces with the sliding velocity in a sliding contact between two hydrophilic surfaces, to a decrease of the capillary adhesion. However no experimental evidence has yet been sighted. In this chapter, we present the first experimental evidence of the role of capillary adhesion in friction mechanisms and we propose a model to explain our experimental results.*

1. Combining the Circular mode with the conventional force distance mode

The force mode in the conventional AFM allows acquiring force-mode spectrum. In this mode, the probe follows a back and forth vertical displacement (at a given retracting velocity) and the interaction force F between the tip and the sample, at a given distance, is determined by the cantilever deflection, *ΔZ*, following the Hooke's Law:

$$F = -k_N \Delta Z \qquad 3.1$$

, where k_N is the normal cantilever stiffness (Annex. 1).

The force curve represents the cantilever deflection due to interaction forces versus the piezo-actuator displacement. Figure 3.1 represents steps that can be distinguished on a force curve.

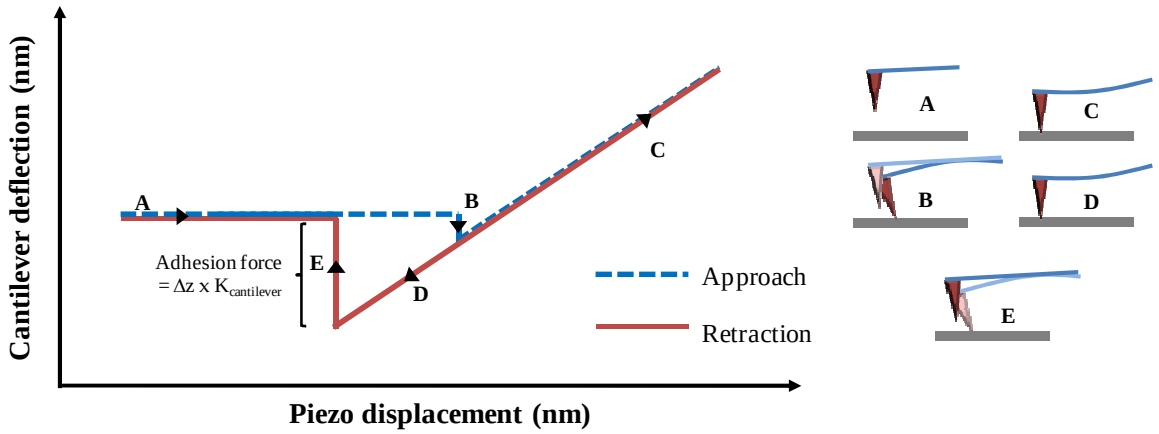

Figure 3.1: Typical force spectra observed experimentally. The curve shows the steps of the cantilever deflection during a single force measurement, A) when the tip is out of contact, B) snap into contact with surface, C) tip is in contact with the surface, D) tip retracting from the surface contact, E) snap off from the surface contact. The value of the cantilever deflection Δz (nm) during snap off multiplied by the normal cantilever stiffness will result in the adhesion force value (nN).

At the beginning of the vertical movement of the tip towards the surface (supposing a scanned tip scanner) the cantilever is not bent, and no forces are acting on the tip due to the large separation distance (A). When the attractive forces start to act on the tip they result in small downward deflections of the cantilever, a snap into contact of the tip to the surface occurs, resulting in a cantilever deflection that when measured corresponds to the attractive forces (B). Then, the tip remains in contact with the surface while adhesion between the tip and the surface develops (C). In the reverse motion of the scanner, the tip is in contact with the surface until the jump off from the surface occurs that corresponds to a Z-piezo-actuator displacement that is different than the snap-in (D to E), and finally, the cantilever gets back to its equilibrium state. The pull off force on the force distance curve is measured quite larger than that of the snap in, which is due to the adhesion forces, capillary forces, and short range forces.

Conversion of the force from voltage to metric units is obtained by setting the slope to one when a probe and a rigid surface are in contact. In this case, no indentation can occur and the cantilever deflection will correspond to the piezo-actuator displacement.

In our experiments, we combined the conventional force mode with the Circular mode. In such case, one can acquire force spectrum (vertical displacement of the probe) while the probe is moving in a circular motion (in the plane of the sample).

Therefore, when in contact, the probe slides on the surface with a circular motion, and the snap-off resulting of the vertical displacement of the probe represents the adhesion force in a sliding nanometer-sized contact. The advantage in using the Circular mode rather than a conventional back and forth displacement is that stationary states are attainable as constant and continuous displacements are performed when measuring with the Circular mode.

A comparison of the combination of the force mode to the conventional back and forth scanning and to the Circular mode is schematically represented in Figure 3.2.

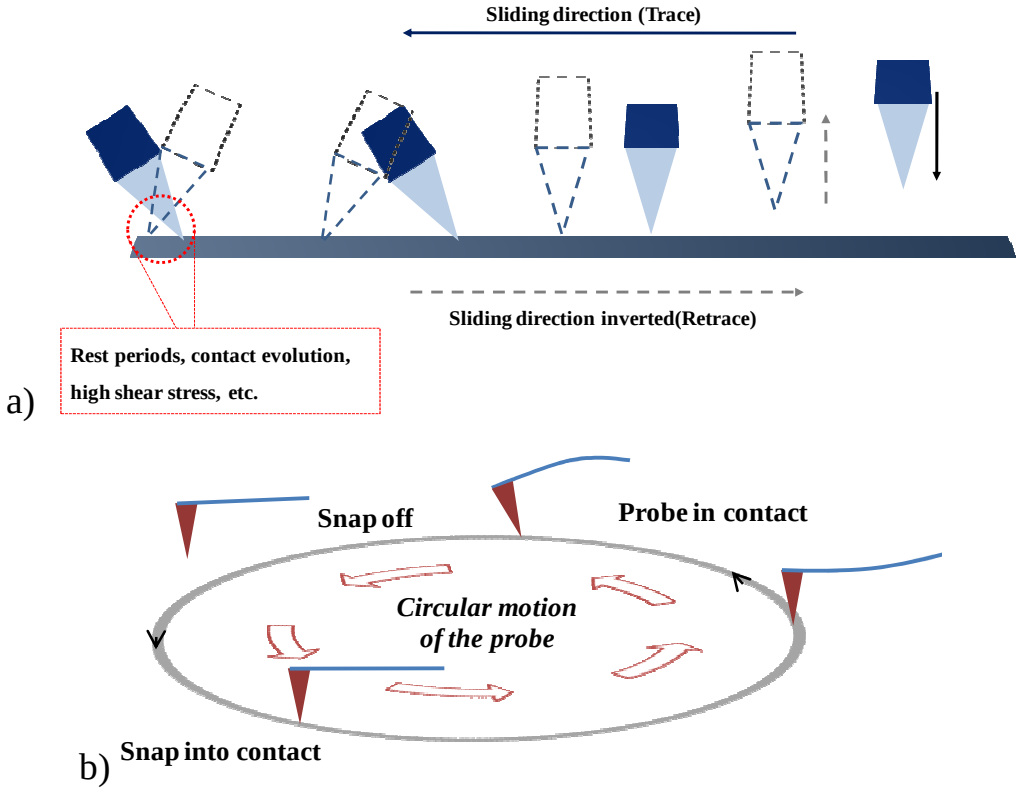

Figure 3.2: Schematic of a) the back and forth sliding motion of a probe with the conventional AFM mode coupled with the adhesion force spectra. The inversion is clear at the end of the track, and this will lead to rest periods, that in turn will lead to an evolution of the probe/sample contact. b) the Circular mode coupled with the adhesion force spectra. The probe slides in a circular motion while performing force spectra, a stationary state is attainable with constant and continuous sliding motion (no acceleration, deceleration, or rest periods).

In conclusion, combining the force mode and the Circular mode allows measuring the adhesion force in a sliding nanometer-sized contact, in a stationary state and at high sliding

velocities. This experimental set-up will be used to investigate the influence of the sliding velocity on the capillary adhesion between different hydrophilic surfaces.

2. Experimental procedure

The following procedures were followed for all experiments reported in the thesis conducted with the Circular mode:

i) Topographic contact mode images (5 µm × 5 µm) are first acquired to select the appropriate portion of the sample to perform the experiment (Fig. 3.3). By analyzing the topographic images, average roughness of each sample was also calculated.

ii) Force volume images were also taken for each sample to investigate the homogeneity of the adhesion forces between the probe and sample (Annex. 3).

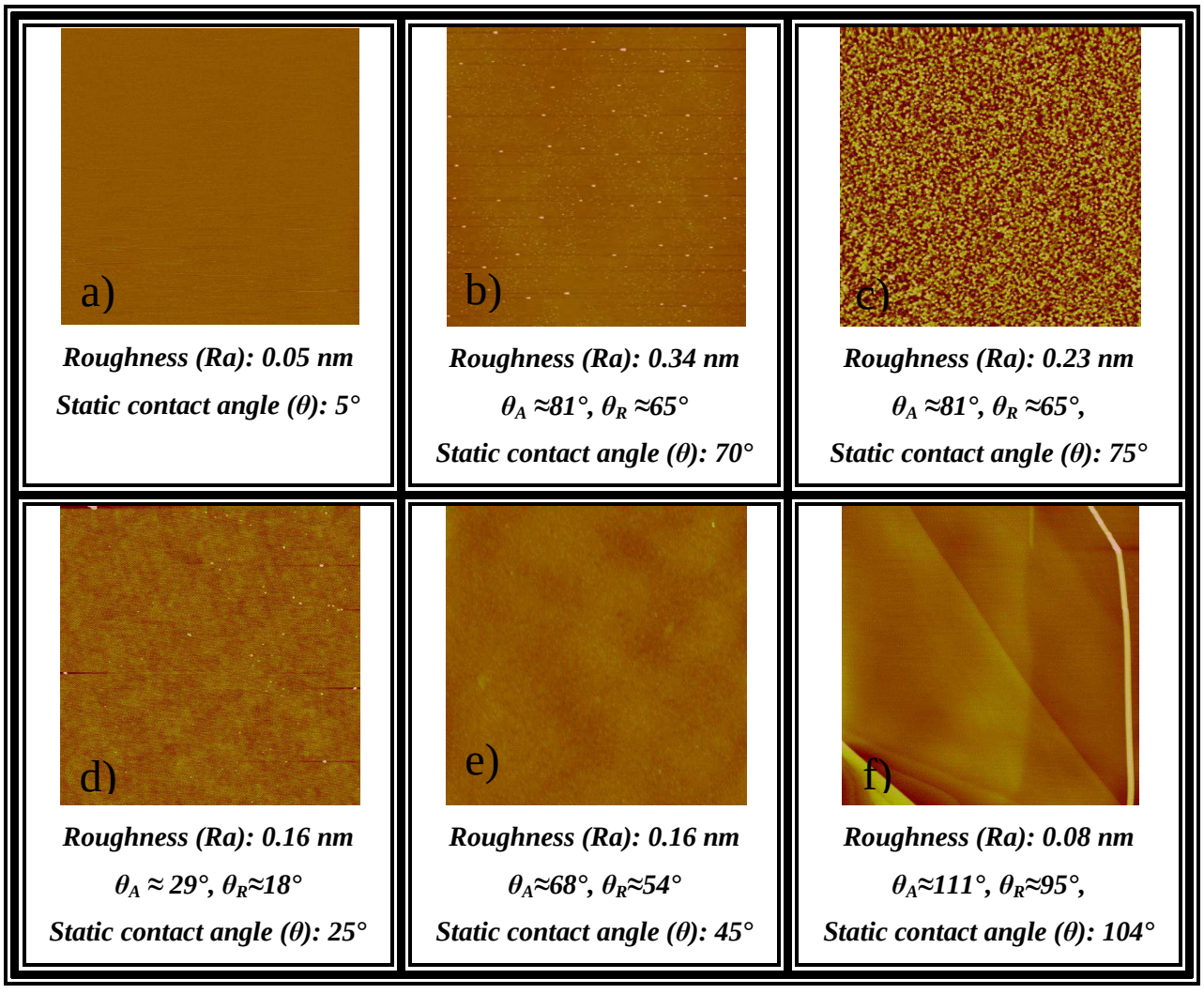

Figure 3.3: 5 µm x 5 µm topographic image of a) mica b) silicon nitride c) gold d) glass e) silicon f) HOPG, surfaces with their respective roughness value and the static (θ), advancing (θ_A) and receding (θ_R) contact angles with water; The surfaces were acquired with contact AFM tip.

iii) After each experiment, topographic AFM images in contact mode are acquired. It is worth mentioning that no wear or plastic deformation was noticed on the surfaces we used after performing experiments with Circular mode (comparable topographic images at the same place of the sample were the experiments were conducted).

iv) Static contact angle measurements with water were also performed to characterize the hydrophilicity of the surfaces. The contact angle was measured for all surfaces by the use of a (Ramé-Hart Contact Angle Goniometer) (Fig. 3.4-a). We used the static sessile drop method and deposited a 2 mL drop of water on a flat surface. The angle formed between the liquid/solid interface and the liquid/vapor interface is the static contact angle. It is simply calculated by drawing on the obtained image a line tangent to the liquid/vapor interface at the contact line.

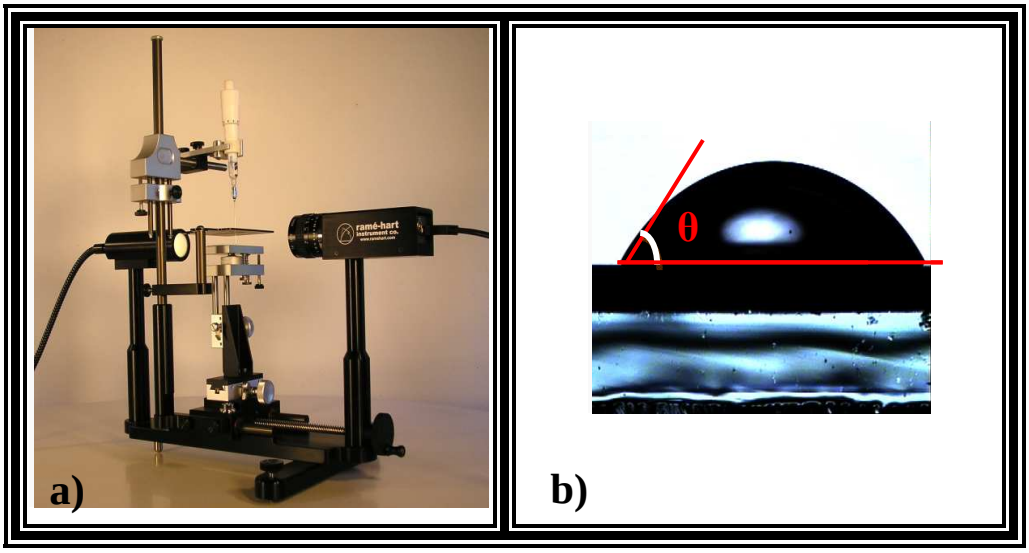

Figure 3.4: (a) Image of the contact angle goniometer, (b) Image of the drop on a gold surface, the measured angle θ corresponds to the angle between the base line (the liquid/solid interface) and the liquid/vapor interface.

All surfaces were cleaned by ethanol in ultrasonic bath for a period of time ranging from 5 to 10 min, whereas, mica and HOPG were cleaved just before performing the experiments.

3. *Experimental data- adhesion force values at different sliding velocities*

Using the Circular mode force measurements were conducted with a triangular cantilever (normal cantilever stiffness $k_N \approx 0.5$ N/m) and a silicon nitride tip. The retracting velocity at

which the force spectra were measured was set to 0.1 µm/s. The adhesion forces corresponding to the cantilever deflection due to the interaction forces during snap off were measured as a function of the sliding velocity. Measurements were conducted on various hydrophilic surfaces such as CVD gold, silicon nitride, silicon wafer, glass and mica, and on various hydrophobic surface such as methyl grafted silicon wafer (Si_{CH3}), and Highly Ordered Pyrolytic Graphite (HOPG).

Figure 3.5 shows typical force spectra obtained at a relative humidity higher than 40 % in air, at room temperature (24°C) with a silicon nitride tip (radius 30-40 nm), on a HOPG hydrophobic sample (104° static contact angle with water) and at different sliding velocities.

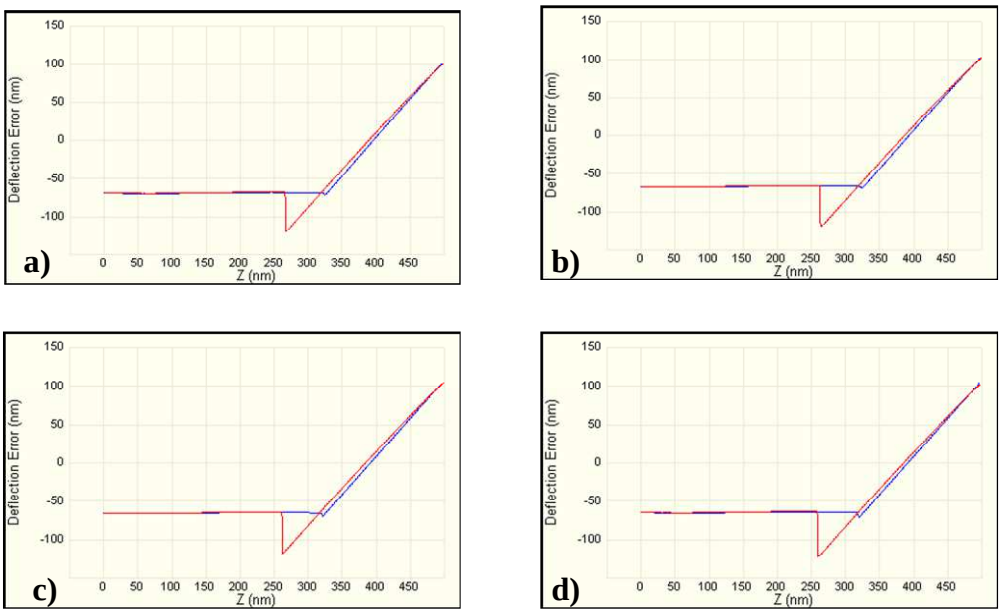

Figure 3.5: Force Spectra acquired on a HOPG (Contact angle θ = 104°, roughness R_a = 0.05 nm) at different sliding velocities a) 0 mm/s, b) 0.1 mm/s, c) 0.3 mm/s, and d) 1 mm/s. As sliding velocity increase, the adhesion force remains constant. The experiment was conducted with a slicon nitride probe of cantilever stiffness of k_N = 0.57 N/m, and at a relative humidity RH = 40%.

The force spectra obtained on a freshly cleaved HOPG sample or other hydrophobic surfaces such as methyl grafted silicon wafer (Si_{CH3}) surfaces clearly show that the adhesion force (cantilever deflection) remains constant whatever the sliding velocity is. This is expected for hydrophobic surfaces as no capillary forces can act for such surfaces. The adhesion force is only the contribution of the attractive van der Waals forces.

However, for hydrophilic surfaces the adhesion force decreases with an increase of the sliding velocity. Figure 3.6 shows typical force curves obtained at a relative humidity higher than 38 % in air, at room temperature (24.4°C) with a silicon nitride tip (radius 30-40 nm), on a hydrophilic CVD gold surface (60° static contact angle with water).

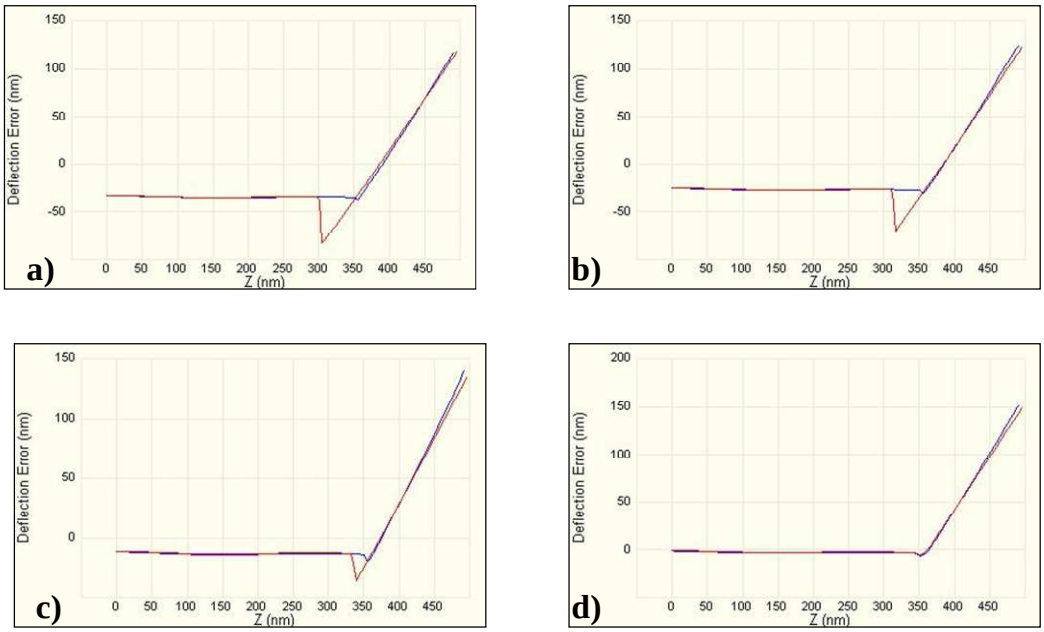

Figure 3.6: Force Spectra acquired on a CVD gold layer (Contact angle θ = 75°, roughness R_a = 0.23 nm) at different sliding velocities a) 0 mm/s, b) 0.1 mm/s, c) 0.3 mm/s, and d) 1 mm/s. As sliding velocity increase, the adhesion force decreases. The experiment was conducted with a slicon nitride probe of cantilever stiffness of k_N = 0.57 N/m, and at a relative humidity RH = 38%.

For adhesion measurements at humidity higher than 30%, capillary condensation can occur in the case of hydrophilic surfaces in contact, which results in capillary forces acting on the probe. These capillary forces are dominant in the adhesion force, at the nanoscale [138, 139]. The decrease of the adhesion force results from a decrease of the capillary adhesion, which means that the capillary meniscus is disturbed while the probe is sliding on the surface. One can assume that at high sliding velocities the capillary meniscus has vanished and that the adhesion force results only from the attractive van der Waals forces acting between the probe and the surface [131].

For further confirmation of the previous assumption, adhesion force measurements were conducted with the Circular mode under argon (to achieve low relative humidity values ≈ 5 -

8 %, at these humidity values a capillary meniscus cannot form) with a home-made chamber. Comparable adhesion force values were obtained from force curves acquired with the same silicon nitride tip on different hydrophilic surfaces (silicon wafer, CVD gold) in air with the Circular mode at high velocity on one hand, and under argon (where no capillary meniscus is formed) as previously suggested [7, 130, 132] on the same sample with no sliding on the other hand (Fig. 3.7)[11].

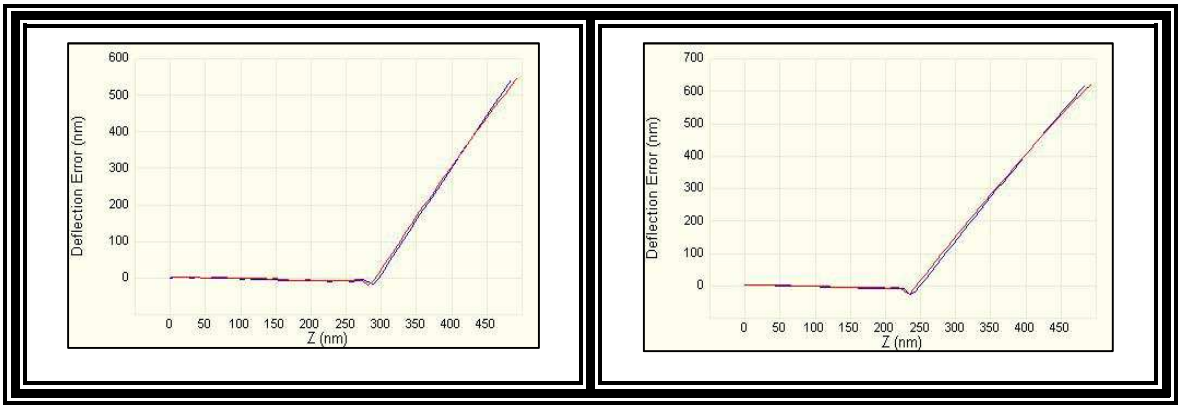

Figure 3.7: Force spectra measured on a gold surface (Contact angle θ = 60°, roughness R_a = 0.23 nm) with the same tip (Silicon nitride R ≈ 30 nm) at different humidities (left) under argon with no velocity and (right) in air at a relative humidity of 44% with a sliding velocity of 1mm/s.

Other reasons could be proposed that could cause a variation of the adhesion force with the sliding velocity.

For instance, the volume of the capillary meniscus will change if the shape of the tip changes. Thus the tip geometry can fundamentally change the capillary force. Therefore, when performing experiments with the Circular AFM mode, any destruction or modification of the tip can be the reason for the decrease of the capillary force. In our experiments, we used an AFM silicon nitride tip (DNP cantilevers from Veeco) whose radius, R (typically R equals to 30-40 nm) was estimated by Environmental Scanning Electron Microscopy (ESEM) imaging (Fig. 3.8). The (ESEM) images were taken before and after the experiments and no change in the geometry or the radius of the probe was noticed at the resolution of the ESEM (Fig. 3.8). Moreover, average adhesion forces calculated from a tenth of force curves at zero sliding

[11] *If one is concerned with the limitations of capillary adhesion in an adhesion force measurement, one can notice that experiments with the circular mode at high sliding velocities can result in the same values of the adhesion force as if the experiments are conducted in vacuum, with no additional equipment.*

velocity were systematically acquired on a reference sample, before and after conducting each experiment on a given surface, and the values were comparable. This procedure eliminates the possibility of attributing the decrease of the adhesion force to any change in the tip form or contamination of the tip.

Plastic deformation of the materials due to the high pressure applied on the materials by the probe could also occur. However, contact topographic AFM images where taken before and after each experiments and did not show any imprints on all the surfaces resulting from plastic deformation or wear[12].

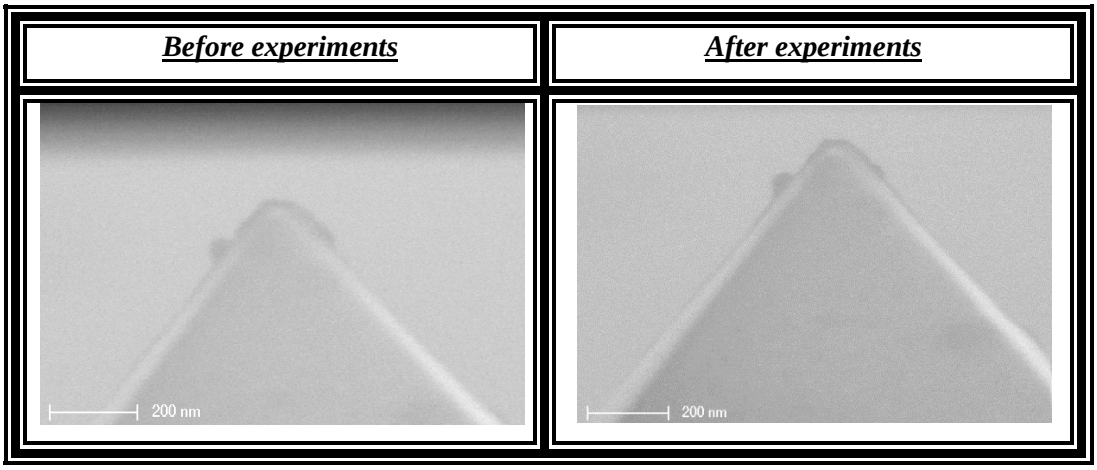

Figure 3.8: ESEM images of silicon nitride tip before and after conducting experiments with the Circular mode on a glass surface

4. Adhesion force dependence on the sliding velocity

Using the Circular mode, we conducted adhesion force measurements versus the sliding velocity on model hydrophilic substrates with different physical-chemistry surface properties, such as gold, glass, silicon wafer, silicon nitride, and freshly cleaved mica. The experiments were conducted at room temperature ($T \approx 25°C$), at relative humidity $RH > 30\%$ and with a silicon nitride probe ($R \approx 30°$).

The behavior of the adhesion force as a function of the logarithm of the sliding velocity on a mica sample (static contact angle with water $\theta = 5°$, $R_a = 0.05$ nm) is presented in Figure 3.9. One can notice three regimes:

[12] *One should be care that wear of a gallium arsenide (GaAs) and titanium surfaces obtained with a silicon nitride probe was used for the calibration process, but these surfaces are not used for our experiments*

- The wet regime (Regime I), at low sliding velocities, the adhesion force is independent of the sliding velocity, and has high values. In this regime, the adhesion force is a contribution of both the capillary and van der Waals forces.
- The intermediate regime (Regime II), that starts at a critical velocity referred to as V_{start} at which the adhesion force starts to linearly decrease with the logarithm of the sliding velocity, this decreasing behavior for the adhesion force has already been suggested by E. Riedo [7] for explaining the friction force dependence on the sliding velocity.
- The dry regime (Regime III), at high sliding velocities, the adhesion force is independent of the sliding velocity. In this regime the adhesion force is only the contribution of the attractive van der Waals force and the capillary forces have vanished.

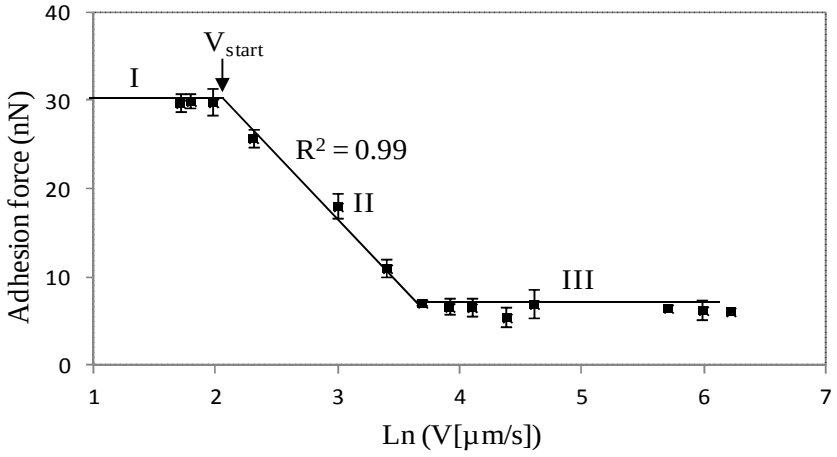

Figure 3.9: Adhesion force (computed from 10 spectra, error bars represent the standard deviation) versus the logarithm of the sliding velocity for a mica surface (relative humidity RH =41%, tip radius is R ≈ 30 nm), the adhesion force follows three regimes. R-squared values R^2 correspond to the best linear fit of the intermediate regime. Lines on the curves are for visual aid of the three regimes

Figure 3.10 shows experiments conducted at the same experimental conditions (tip radius R = 30 nm, humidity, temperature) as that of the previous experiment on mica, and the behavior of the adhesion force on all surfaces results in a similar trend to that observed on mica surface.

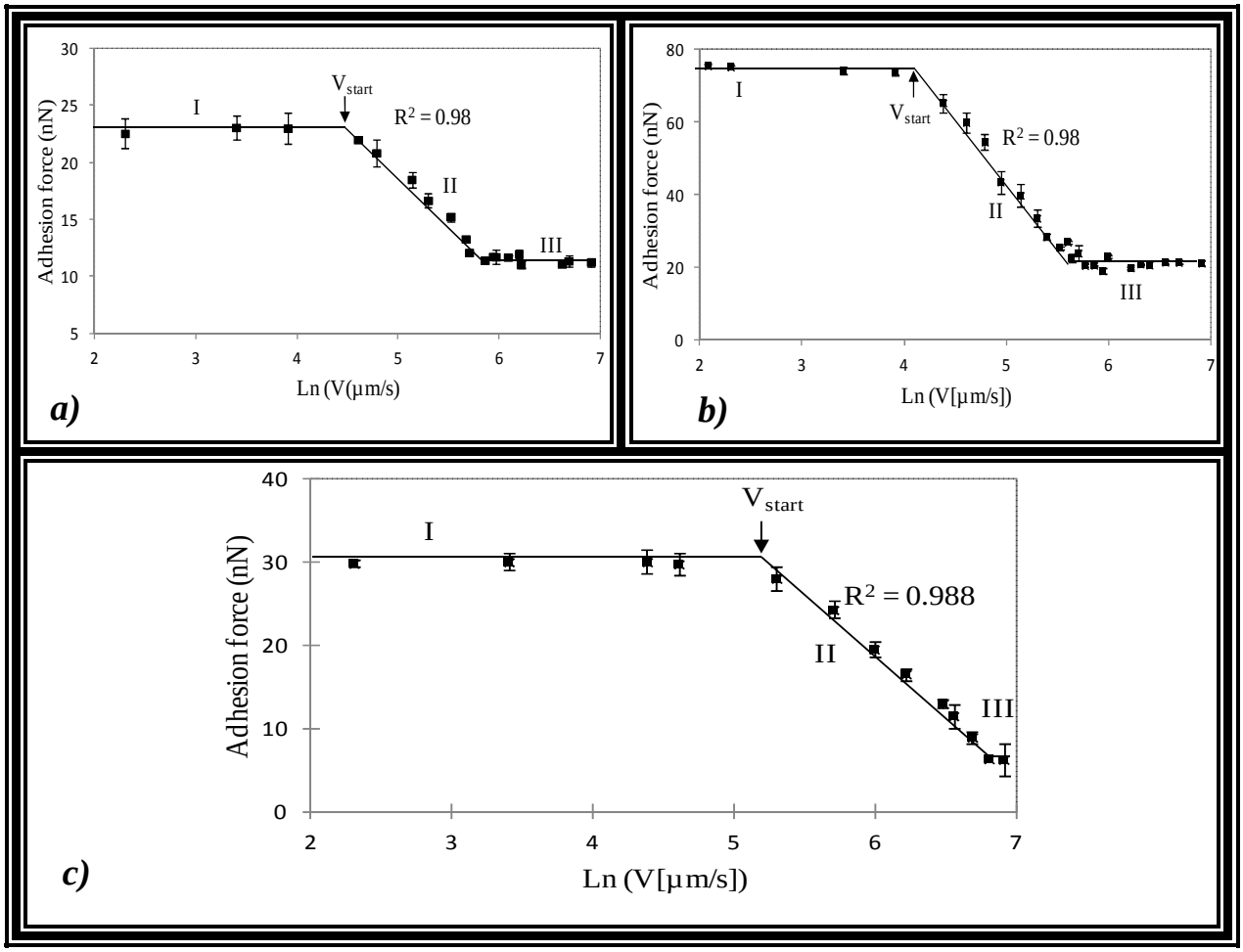

Figure 3.10: Adhesion force versus the logarithm of the sliding velocity with the same probe (R ≈ 30 nm) and the at the same relative humidity (RH = 41%) for a) silicon nitride sample (static contact angle with water θ = 70°), b) silicon wafer sample (static contact angle with water θ = 45°), c) gold surface (static contact angle with water θ = 75°). The adhesion force varies with the ln (V) following three regimes. R-squared values R^2 correspond to the best linear fit of the intermediate regime. Lines on the curves are for visual aid of the three regimes.

Figure 3.10 shows that for hydrophilic surfaces, the trend for the behavior of the adhesion force versus the logarithm of the sliding velocity always follows three regimes: the wet regime, the intermediate regime and the dry regime. We also notice that V_{start} (the logarithm of the sliding velocity at which the second regime begins) decreases when the hydrophilicity of the surfaces is increasing. However, we do not see a clear trend for V_{start} due to the variation of the surface roughness. The evolution of V_{start} with the hydrophilicity of the surface is also expected if we consider that for a given tip radius and at a given relative

humidity, the size of the meniscus increases with the hydrophilicity of the surface. Indeed, it takes more time for the capillary meniscus to reform completely if its volume is high. For our experiments, the size of the capillary meniscus is higher for the mica (lower contact angle) and lower for the gold (higher contact angle). Then the V_{start} is the lowest for the mica sample (volume of the capillary meniscus is high) and the highest for the gold sample (volume of the capillary meniscus is low). We checked that the vertical scanning velocity does not change the trends we observed for the adhesion force and for V_{start}.

Figure 3.11 shows another set of experiments conducted with the same tip (R = 25 nm) and at the same relative humidity (experimental conditions). The behavior of the variation of the adhesion force with the logarithm of the sliding velocity shows similar results to the previous one. In particular, V_{start} still changes with the hydrophilicity the surfaces in the same manner.

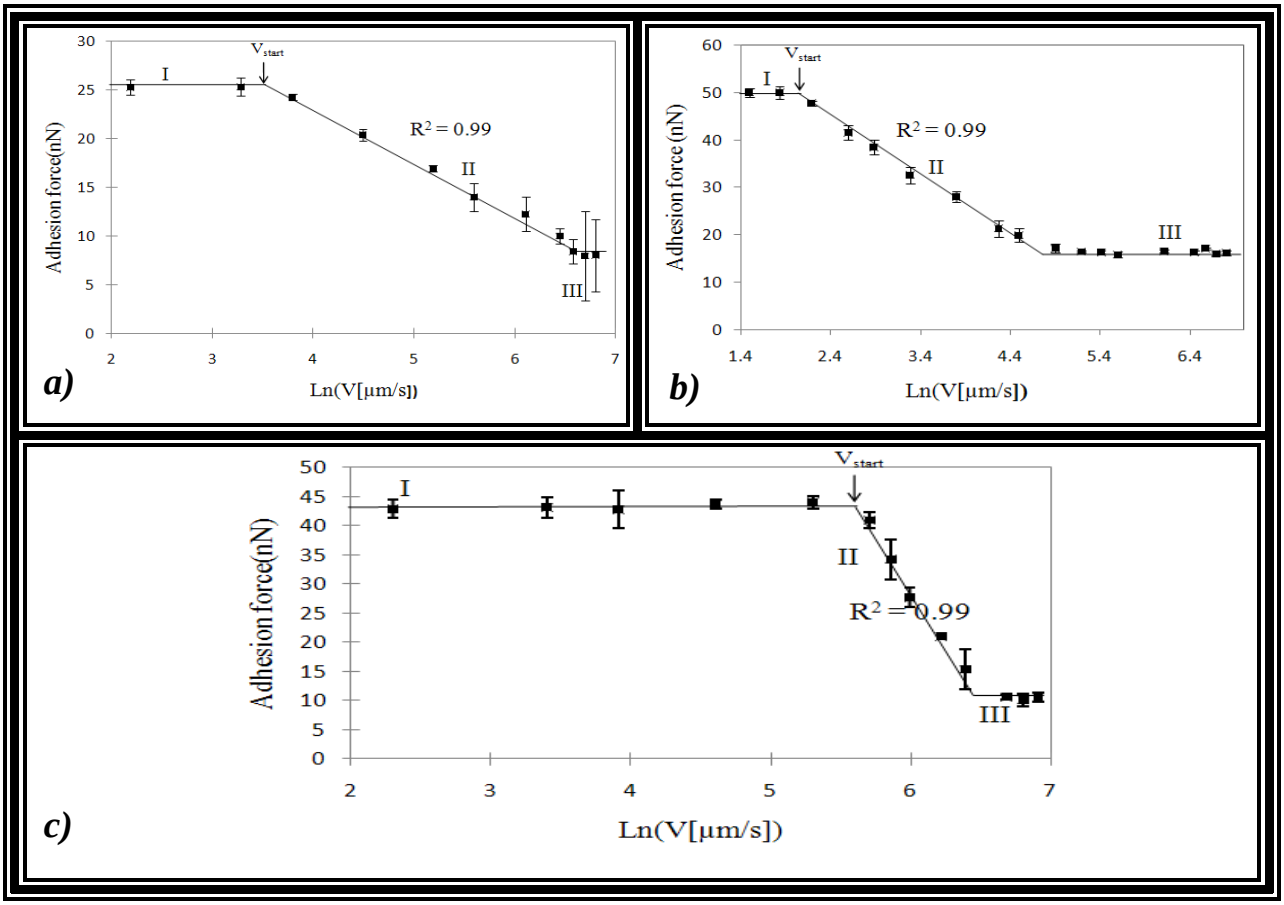

Figure 3.11: Average adhesion force as a function of the logarithm of the sliding velocity with the same probe (R= 35 nm) and at the same relative humidity (RH = 48%) for a) glass (static contact angle with water θ = 25°), b) mica (static contact angle with water θ = 5°), c) gold (static contact angle with water θ = 75°) sample, the adhesion force varies with the ln (V) following three regimes. R-squared values R^2 correspond to the best linear fit of the intermediate regime. Lines on the curves are for visual aid of the three regimes.

Finally, the adhesion force values in the third regime were calculated and compared to those of the van der Waals force values calculated theoretically for a silicon nitride probe in contact with a specific sample. The van der Waals force was calculated based on the equation $A_H R/6d^2$, where A_H is the Hamaker constant and correspond to values from ref [140], R is the probe radius, and d is the smallest separation distance (≈ 0.165 nm) [33]. The results are shown in Table 3.1.

Surface	Probe	A_H (x10^{-20}) in air (J)	F_{vdW} theoretical (nN) [140]	F_{vdW} experimental (nN)
Mica	R = 25 nm	12.8	23.5	19.58
Si_3N_4	R= 30 nm	16.7	30.67	11.21
Glass	R= 25 nm	10.8	16.52	8.38
Silicon wafer	R= 30 nm	16.84	30.92	20.04

Table 3.1: Comparison of the obtained experimental adhesion values of the third regime with the van der Waals force values calculated theoretical for the contact between a probe and its specific sample. The van der Waals force were calculated based on the equation $\frac{A_H R}{6d^2}$, and A_H is the Hamaker constant.

5. *Measurements performed with same physical chemical properties at different humidities*

The three regimes observed in the previous experiments are depending on the evolution of the capillary meniscus with the sliding velocity. Moreover, the evolution of V_{start} can be correlated to the size of the capillary meniscus.

To check this assumption, we measured the variation of the adhesion force with the logarithm of the sliding velocity on the same sample (gold) and by changing the humidity. The results are shown in Figure 3.12.

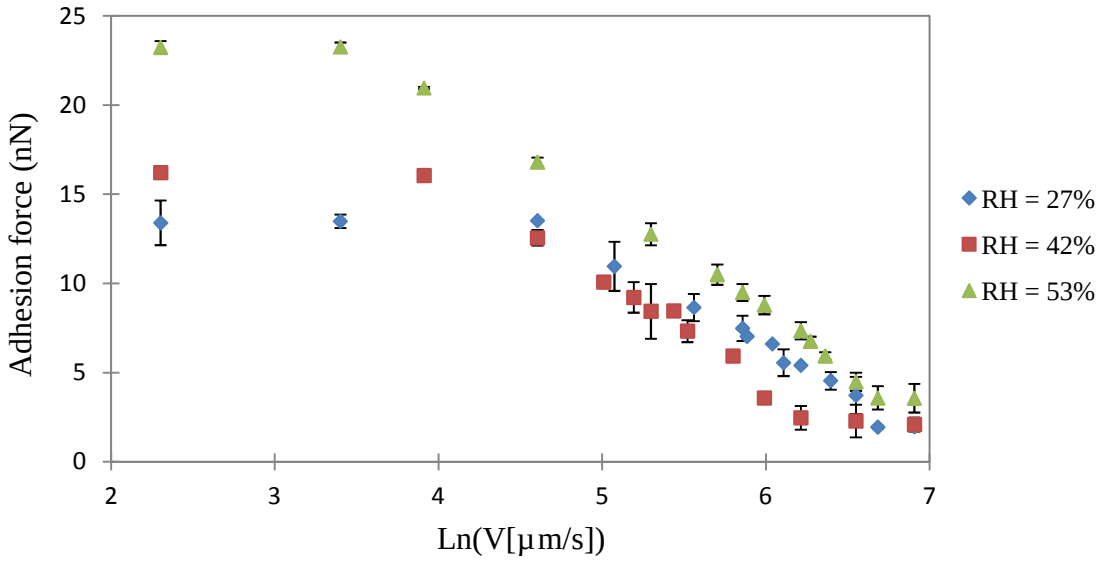

Figure 3.12: Average adhesion force as a function of the logarithm of the sliding velocity with the same probe ($R \approx 40$ nm) on the same CVD gold sample (static contact angle with water $\theta = 75°$). The curves show a change in the V_{start} as the humidity is changing.

We notice that in the first regime, for experiments conducted at higher humidity, the adhesion force is higher; this is in agreement with the literature. Furthermore, The V_{start} (the logarithm of the sliding velocity at with the second regime begins) is decreasing with the increase of the humidity. It has already been shown in the literature that the meniscus size is humidity dependent (section 1-5.3). This suggests that the beginning of the intermediate regime is size meniscus dependent. The trend we observe is also in good agreement with our qualitative assumption (Fig. 3.12).

6. Reversibility of the behavior

We have conducted an experiment to study the variation of the adhesion force with the sliding velocity, by increasing step by step the sliding velocity (in this case, the meniscus is vanishing) and then decreasing it step by step (in this case, the meniscus reforms) (Fig. 3.13). The same variation of the adhesion force with the sliding velocity was observed for both experiments. This confirms that our experiments are conducted in a stationary state and that the decrease of the adhesion force is not related to energy dissipation due to friction, but that it is really related to the capillary meniscus and its vanishing or reformation.

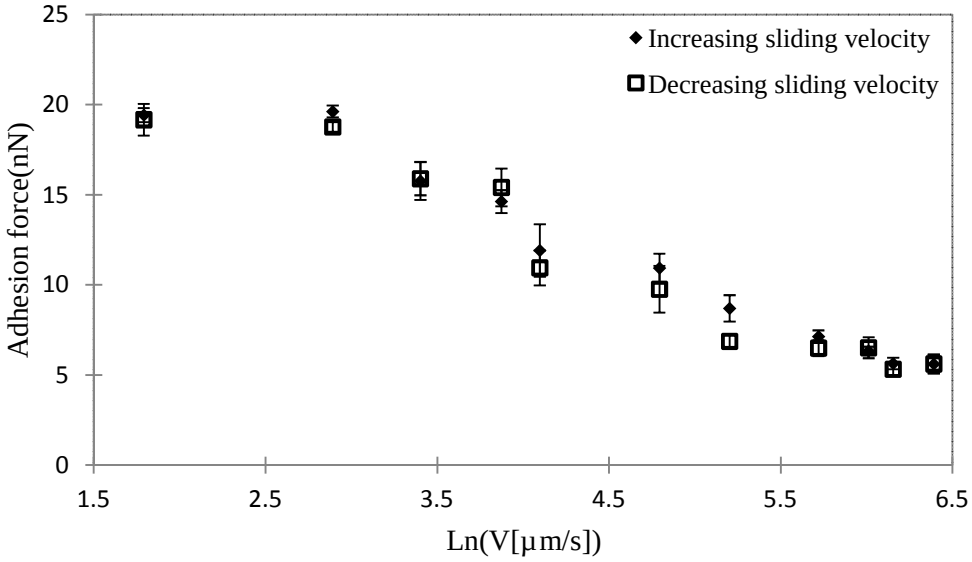

Figure 3.13: Average adhesion force as a function of the logarithm of the sliding velocity with a silicon nitride probe ($R \approx 40$ nm) and the on a gold sample (static contact angle with water $\theta = 75°$) at a humidity of 37%.

7. Theoretical approach of the influence of the sliding velocity on capillary adhesion

Different behaviors of the friction force with the sliding velocity were reported in the literature [7, 8, 80]. In particular, Riedo *et al.* [7] showed a linear increase of the friction forces with a logarithmic increase of the sliding velocity for partially hydrophobic surfaces and a linear decrease of the friction force with the sliding velocity for partially hydrophilic surfaces. The authors attributed the increase of the friction force to stick slip process. They also suggested that the decrease was attributed to a thermally activated nucleation process that can occur in the gaps formed by a multi-asperity contact and that is time or sliding velocity dependent [7].

Indeed, the nucleation time of a capillary bridge in a 1 nm gap between asperities in the case of a silicon AFM probe and a soda lime glass has been experimentally estimated to be of the order of the ms, for temperatures ranging from 299 K to 332 K at a relative humidity of 40 % [99]. While increasing the sliding velocity, the capillary meniscus is disturbed by the relative displacement of surfaces and has less time to reform. As a result, an increase of the sliding velocity leads to a decrease of the capillary force. The capillary adhesion acts as an additional

normal load in the friction mechanism, and a decrease of the capillary adhesion results in a decrease of the friction force.

The model of Riedo et al. is an extrapolation of a model previously proposed by Bocquet et al. [44] that describes the capillary adhesion process in a granular media. The model of Bocquet was determined in considering a macroscopic contact in which multi-asperity contact situation can be reasonably considered. However, Riedo et al. have done the same assumption that supposes the existence of many asperities (multi-asperity contact) on the two surfaces in the vicinity of the contact between the probe and the sample, but at the nanoscale. In this model, the nucleation of a liquid bridge of volume Ω between two asperities, at a temperature T and at a relative humidity R_H, costs a threshold free energy ΔE [44].

$$\Delta E \approx k_B T \ln\left(\frac{1}{R_H}\right)\rho\Omega \qquad 3.2$$

, where ρ is the molecular density of the liquid in units molecules/m^3. Commensurate with this thermally activated process, Szoszkiewicz and Riedo [99] have experimentally estimated the nucleation energy barrier of a capillary bridge in a gap of 1 nm height formed by asperities between a silicon AFM probe and a soda lime glass to be about 1 eV, similar to the values reported by Greiner et al. [8]. If we consider a nucleation process, we can estimate by using the experimental value of ΔE reported in references [99] and equation 3.1 the volume of water, Ω, of the capillary bridge to be 0.4 nm^3. This volume corresponds approximately to a dozen of water molecules which is about 500 times smaller than the number of water molecules needed to form the complete water meniscus around a probe of 25 nm radius [99].

In the previous section, we have presented the first ever-direct experimental measurement of the influence of the sliding velocity on the adhesion force, on both hydrophilic and hydrophobic surfaces, by the use of the Circular mode. The linear decrease observed for the capillary adhesion with a logarithmic increase of the sliding velocity also suggests that a thermally activated process is responsible for it. However to explain such behavior, one can consider either nucleation of water bridges between surfaces close to each other or the growth of the capillary meniscus that are both thermally activated processes in which the meniscus formation has to overcome energy barriers, ΔE, i) to initiate the formation of the capillary bridges or meniscus, ii) to pass over surface defects constraining the meniscus growth [97].

To make a choice between both processes, let's consider the results obtained on an atomically flat surface as a mica surface. Riedo and al. [83] reported an increase of the friction force with the sliding velocity when conducting experiments on a mica surface. In this configuration, she assumes that nucleation cannot occur in the contact as for an atomically flat surface, the asperities are atomic. Therefore, the authors attributed the increase of the friction force with sliding velocity to a stick-slip mechanism. However, this assumption is not confirmed by our experiments conducted on an atomically flat mica surface that have shown a linear decrease of the adhesion force with the logarithmic increase of the sliding velocity (Fig. 3.9) and that cannot be explained by a stick-slip process, or by a nucleation process only. As Riedo et al. [83], we also believe that the capillary condensation that is efficient to explain the behavior of capillary adhesion with the sliding velocity occurs around the contact and not in the mutli-asperities. This assumption is sustained by complementary analysis of the system. In particular, the ESEM images of the probe apex taken before and after each experiment do not clearly show asperities or high roughness at the limitation of the ESEM resolution, and the rough mean square roughness R_q values computed with $1\mu m^2$ Tapping mode™ images are very small (Table 3.2). In addition, the surface roughness depends on its area and should be extremely small in the wet area occupied by the meniscus [141]. Therefore, there is no evidence of high enough asperities in the contact area to generate the nucleation of full water bridges around the contact area.

This behavior of adhesion force with the sliding velocity on an atomically flat surface cannot be explained by a nucleation process. However, a growth process in which the capillary meniscus nucleates and grows from the probe-sample contact can explain it.

	R_q (nm)	θ(°) ±5°	V_{start} (µm/s)	V_{End} (µm/s)	V_{End}/V_{start}
HOPG	0.05	105			
Si_{CH3}	0.20	100			
Mica	0.03	5	5	44	9
Si	0.16	60	60	134	2.25
Si_3N_4	0.34	70	105	270	2.7
Gold	0.23	75	151	596	4

Table 3.2: Material features and experimental data, R_q is the root mean square roughness determined from a $1\mu m^2$ AFM tapping mode™ topographic image, θ is the static contact

angle with water, V_{start}, V_{End} are respectively the sliding velocity at which the intermediate regime starts and ends in the same experimental conditions.

In particular, evidence of the presence of a capillary meniscus throughout the intermediate regime is confirmed experimentally by error bars that show that the adhesion force value in regime II never decreases to the attractive force value. In addition, the trend reported for V_{Start} with the hydrophilicity of the surface (Table. 3.2) shows that the capillary meniscus is disturbed at lower sliding velocities as the hydrophilicity of the surfaces, which governs the volume of the capillary meniscus at its equilibrium state, increases.

In our model we assume that the water vapor molecules have to overcome a total energy barrier that is a distribution of local energy barriers due to local surface defects such as atomic roughness or local chemical heterogeneities (Fig. 3.14-a), while the capillary meniscus is growing,

$$\Delta E'_{tot} = \sum \Delta E'_{local\ defects} \qquad 3.3$$

In the ideal case, if no local defects are present, the growth capillary meniscus process will be thermodynamically favorable and the meniscus will grow instantaneously (Fig. 3.14-b)

Figure 41 represents the decrease of the energy barrier versus the increase of the growth for both cases, when local defects are present and when not.

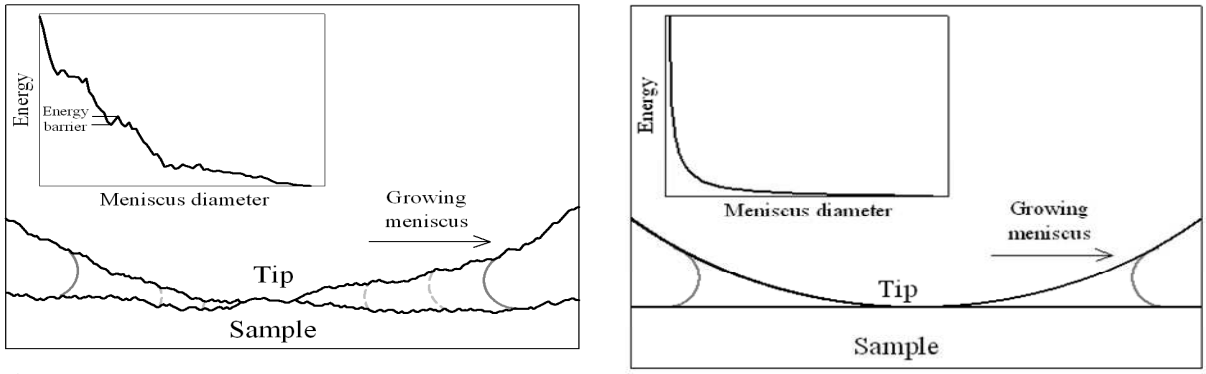

a) **b)**

Figure 3.14: Growing meniscus around the tip-sample contact. The energy barrier becomes higher when the number of surface defects increases during the meniscus growth. There is an increase of the meniscus diameter as the energy decreases. a) An instantaneous decrease of the energy with the increase of the meniscus diameter. b) The energy consists of various energy barriers due to local defects.

The local energy barriers could be also related to the nature of the triple interline region (vapor-liquid-solid interface) that is dependent on the shape of the meniscus, and more importantly on the meniscus contact angle with the surface. This contact line can be distorted by local defects that can be isolated point defects, or surface defects [142, 143] (Fig. 3.15) while the meniscus is growing. A point defect can be due to atomic asperities or atomic roughness or a surface defect related to local chemical heterogeneities.

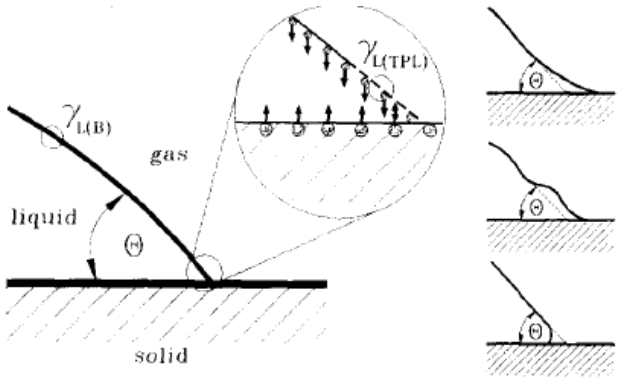

Figure 3.15: The triple line and it distortion in the presence of local defects, image from ref [142].

Furthermore, the growth energy barrier cost (Fig. 3.14), $\Delta E'$, is influenced by these *local* defects, it increases when their number and their size increase [44, 93, 96-98]. The value of $\Delta E'$ is supposed to increase as the edge of the capillary meniscus spreads onto the surfaces while growing (more defects are present). Therefore, one can assume in a first approximation that $\Delta E'$ is proportional to the perimeter of the wet contact area of the meniscus with both the probe and the sample. This perimeter is,

$$A_W = 2\pi R_1 \qquad 3.4$$

, where, R_1 is the radius of the wet contact area of the meniscus with the probe and the sample.

The radius of the wet contact area can be estimated by considering that the capillary force between two hydrophilic surfaces in contact can be express as,

$$F_c = 2\pi R_P \gamma_{Lv}(\cos\theta_S + \cos\theta_P) \qquad 3.5$$

, where R_P is radius of the probe, θ_P and θ_S are the static contact angles with water of the probe and the surface respectively.

The capillary force acting on an area of contact A is also given by

$$F_c = AP_L = \pi R_1^2 P_L \qquad 3.6$$

, where P_L is the Laplace pressure

$$P_L = \gamma_{Lv}\left(\frac{1}{r_1} + \frac{1}{r_2}\right) \approx \frac{\gamma_{Lv}}{R_K} \qquad 3.7$$

R_K is the Kelvin radius, and equating equations (3.5 - 3.6 - 3.7) gives [33]:

$$R_1 = \sqrt{2R_P R_K[\cos\theta_S + \cos\theta_P]} \qquad 3.8$$

The time t to overcome the energy barrier $\Delta E'$, is given by an Arrhenius law [44]:

$$t = t_0 exp\left(\frac{\Delta E'}{k_B T}\right) \qquad 3.9$$

, where, t_0 is a pre-exponential constant. Following this model, the resident time of the meniscus at the vicinity of the defect is proportional to the inverse of the velocity, V:

$$V \propto \frac{1}{t} \propto exp\left(\frac{-\Delta E'}{k_B T}\right) \qquad 3.10$$

Based on our initial assumption that $\Delta E'$ is proportional to the perimeter of the meniscus $2\pi R_l$, we obtain by combining equation 3.10 with equation 3.8 when the meniscus reaches its equilibrium state (i.e at $V = V_{start}$):

$$\ln(V_{start}) \propto \left(\frac{-\Delta E'}{k_B T}\right) \propto -R_1 \propto -\sqrt{[\cos\theta_S + \cos\theta_P]} \qquad 3.11$$

From equation 3.11, we expect that the logarithm of V_{start} is proportional to $-\sqrt{[\cos\theta_S + \cos\theta_P]}$. The experimental data reported on Figure 3.16 for four hydrophilic

surfaces (the data correspond to the experiments shown on Figure 3.9 – 3.10, show a linear trend as predicted by a model integrating the energy barrier of the capillary growth process.

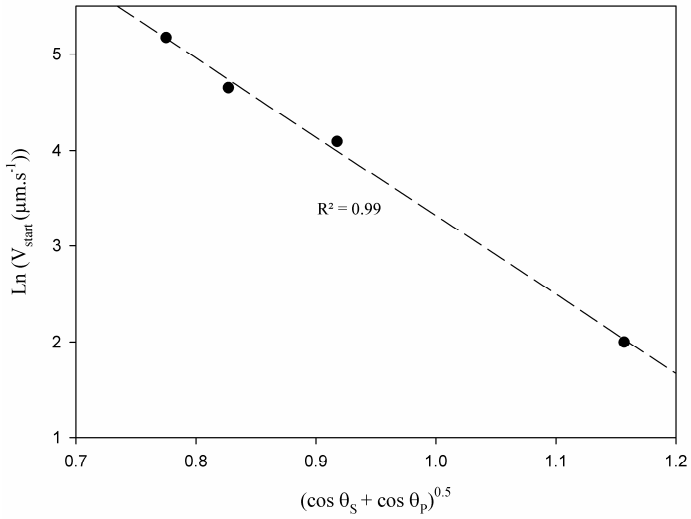

Figure 3.16: Ln (V_{Start}) in function of $[cos\,\theta_S + cos\,\theta_P]^{0.5}$*. All results are obtained at the same relative humidity and with the same tip (41 % RH and 30 nm tip radius). The linear behavior is in good agreement with a model based on a thermally activated growth process.*

8. Conclusion

In conclusion, we have used the Circular mode to perform the first experimental study of the influence of the sliding velocity on capillary adhesion in a sliding nanometer-sized contact. We showed that for hydrophobic surfaces such as HOPG, attractive forces that are mainly van der Waals forces remain constant with the sliding velocity. For hydrophilic surfaces, adhesion forces, mainly due to capillary forces decrease logarithmically with the sliding velocity from a threshold value of the sliding velocity (V_{start}) and vanish at high sliding velocities. This threshold value could be related to the meniscus size rather than to sample roughness. This behavior is observed on a nanometer sized contact between an atomically flat surface and smooth probe, and the kinetics of the capillary condensation are suggested to be related to a thermally activated process that find its origin in either the meniscus growth process or in the nucleation process. However, a model based on the growth process of the capillary meniscus is in good agreement with the experimental data.

Chapter 4. Capillary adhesion versus friction – Preliminary results

The friction force is dependent on the load, and as we have previously shown that the capillary force which acts as an additional external load to the probe is affected by the sliding velocity, it is now interesting to study how friction will change with the sliding velocity. This has been discussed previously in the literature, but in the following we will investigate the influence of sliding velocity on the friction by applying the Circular mode. In addition, the mode allows the possibility of measuring directly and instantaneously the friction coefficient and its variation with sliding velocity can be easily obtained. Such variations on various hydrophilic and hydrophobic surfaces and, the correlation between the friction coefficient and the adhesion force are discussed.

1. Measuring lateral force spectra with the Circular mode

In classical friction measurements the probe is scanned back and forth perpendicular to the main axis of the cantilever. The friction force induces a torsional response of the cantilever that is measured by the lateral force (LFM) signal and the friction force values are computed from the friction loop, i.e. the difference between the LFM signal of the back and the forth displacement (section 1-3.3).

However, when performing a circular motion, it is possible to measure the lateral forces induced by the torsion of the cantilever, simply by adding a lock-in-amplifier (E) (Annex. 4), which measures the average amplitude of the friction force at a selected reference frequency that sets frequency of the circular motion (Fig. 4.1).

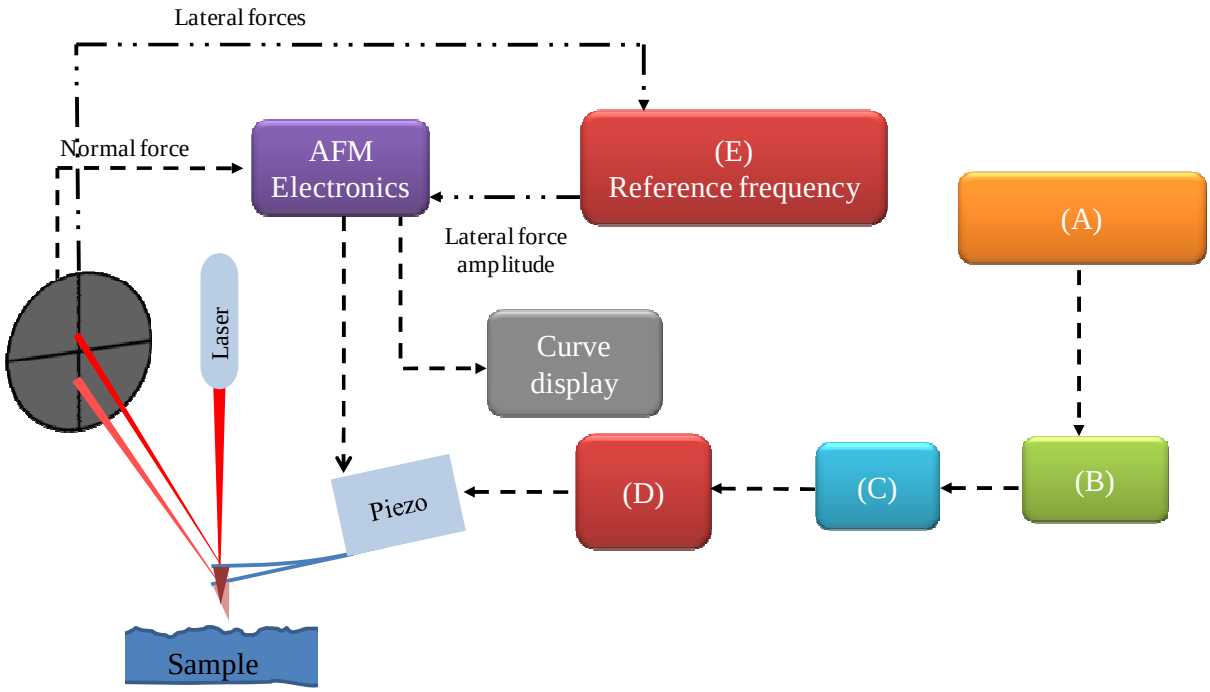

Figure 4.1: Additional instruments to the Circular mode implementation of schema represented in Fig. 2.2; the lock-in-amplifier (E) for measuring the amplitude of the friction force at a selected reference signal.

When using the Circular mode, the friction force should be decomposed in two terms, the parallel F_X and perpendicular F_Y components of the friction force, where the Y direction corresponds to the main cantilever direction (Fig. 4.2). The parallel X component of the friction force generates an alternative torsion of the cantilever and the LFM signal has a sinusoidal shape for which the amplitude is proportional to the friction force and the frequency corresponds to the frequency of the circular motion. Similarly, the perpendicular Y component of the friction force generates an alternative bending of the cantilever and the 'error' signal also has a sinusoidal shape. If the servo-loop is active, this will generate a sinusoidal displacement of the piezo-actuator in the Z axis direction leading to a non constant load and a coupling between normal and friction forces. If the servo-loop is not active, the LFM and 'error' signals have a sinusoidal shape but there is no coupling between the two signals. The bending of the cantilever in the Y direction does not affect the normal load significantly as the external load is not directly applied to the probe.

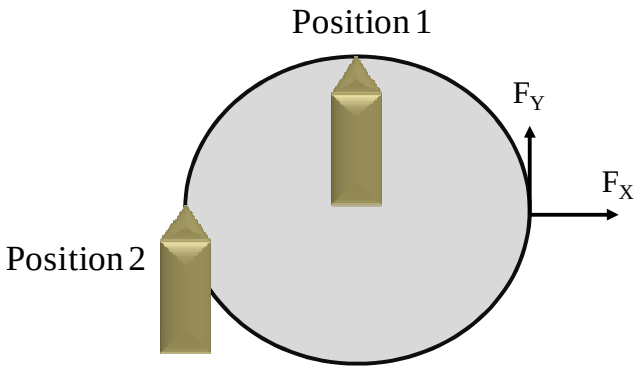

Figure 4.2: The probe moving in a circular motion from position 1 to position 2. When the cantilever is at position 2 during sliding the friction force is equal to F_X the component perpendicular to the main axis of the cantilever that generates an alternative torsion, whereas at Position 1 the friction force is equal to F_Y the component parallel to the main axis of the cantilever and generates an alternative bending of the cantilever.

In addition the local friction force (that corresponds to the lateral force at a given location on the sample) cannot be measured as it is measured in the case of a back and forth conventional scan, because in the Circular mode 1) the sliding direction only occurs parallel to the X axis direction, twice per circular cycle, 2) the friction loop cannot be realized as the probe is always turning in the same direction (no trace and retrace), 3) if the servo-loop is active, there is a coupling between friction and normal forces.

This is not a limitation as if one assumes that the friction force does not depend much on the location, it is possible to measure an average friction force by measuring the amplitude of the LFM signal during circular motion and without using the servo-loop. Previously, authors have suggested similar method using Lateral Force Modulation [144-146].

In our experimental set-up for measuring the friction force, we take advantage of the capability of the Circular mode to be combined to the force mode. This combination allows varying the external normal applied load by imposing a vertical motion (perpendicular to the plane of the sample) to the probe while it is sliding in a circular motion on the plane of the sample. We have direct access to a lateral force spectrum that corresponds to the lateral force (measured by the lock-in amplifier) at different normal loads (which are proportional to the Z piezo-actuator displacement).

It is worth mentioning that acquiring the friction load dependent curve is time consuming when operating with a conventional AFM, whereas it is acquired instantaneously with our experimental set-up. One can also notice that it is possible to directly extract the friction

coefficient value if the friction load dependence is linear or if the Amontons law is verified. In this case, the friction coefficient is given by the slope of the friction force spectrum. Finally, this experimental set-up allows acquiring simultaneously adhesion and friction force spectra (Fig. 4.3).

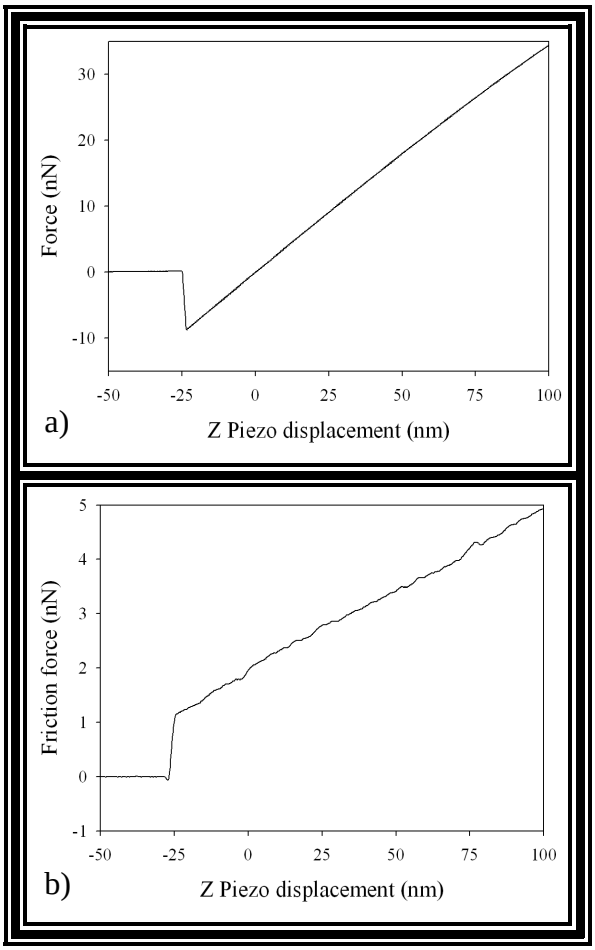

Figure 4.3: Simultaneous acquisitions of a) adhesion and, b) friction force spectra, conducted on a gold sample as a function of the piezo-actuator displacement. The calibration factor of the lateral force is 200 mV/nN (Annex. 1). The friction coefficient is equal to 0.085 at a sliding velocity of 300 µm/s.

All the experiments reported in the next sections are acquired in the air, with a silicon nitride tip (and triangular cantilever) whose normal stiffness is about k_N = 0.4 N/m. The vertical velocity for varying the normal load is set to 0.1 µm/s.

2. Friction with the normal load

Friction spectra were acquired on various hydrophobic surfaces such as HOPG or methyl grafted silicon wafer and glass, and hydrophilic surfaces such as freshly cleaved mica, silicon nitride, silicon, glass and gold surfaces. Figures 4.4 and 4.5 show typical friction force spectra acquired with the Circular mode at low and high sliding velocities for hydrophilic and hydrophobic surfaces respectively.

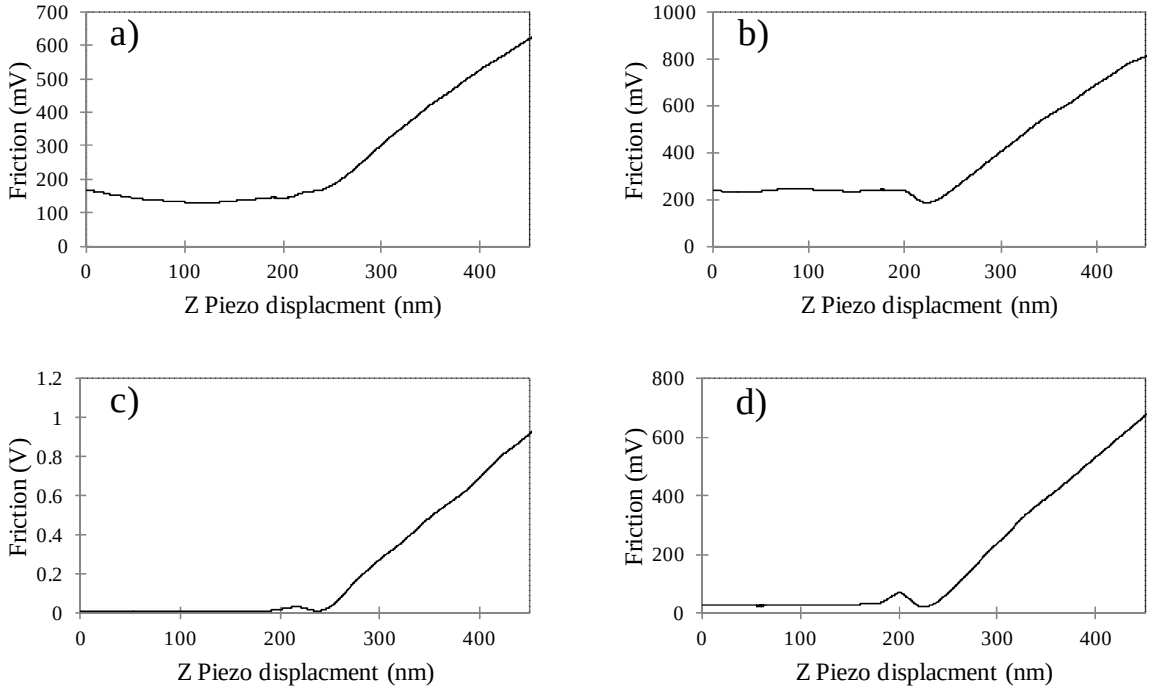

Figure 4.4: Friction spectra obtained with the Circular mode on hydrophobic Si_{CH3} (a and c) and HOPG (b and d) surfaces at high sliding velocities (curves a and b) and at low sliding velocities (curves c and d).

For hydrophobic surfaces, a linear dependence of the friction on the load is clearly observed at low and high sliding velocities (Fig. 4.4)[13].

[13] *One should notice that even when the tip is not in contact with the surface, the lateral force is not zero. This small offset of the baseline of the spectrum could be related to the piezo-actuators motion that vibrates the cantilever when it is in the air.*

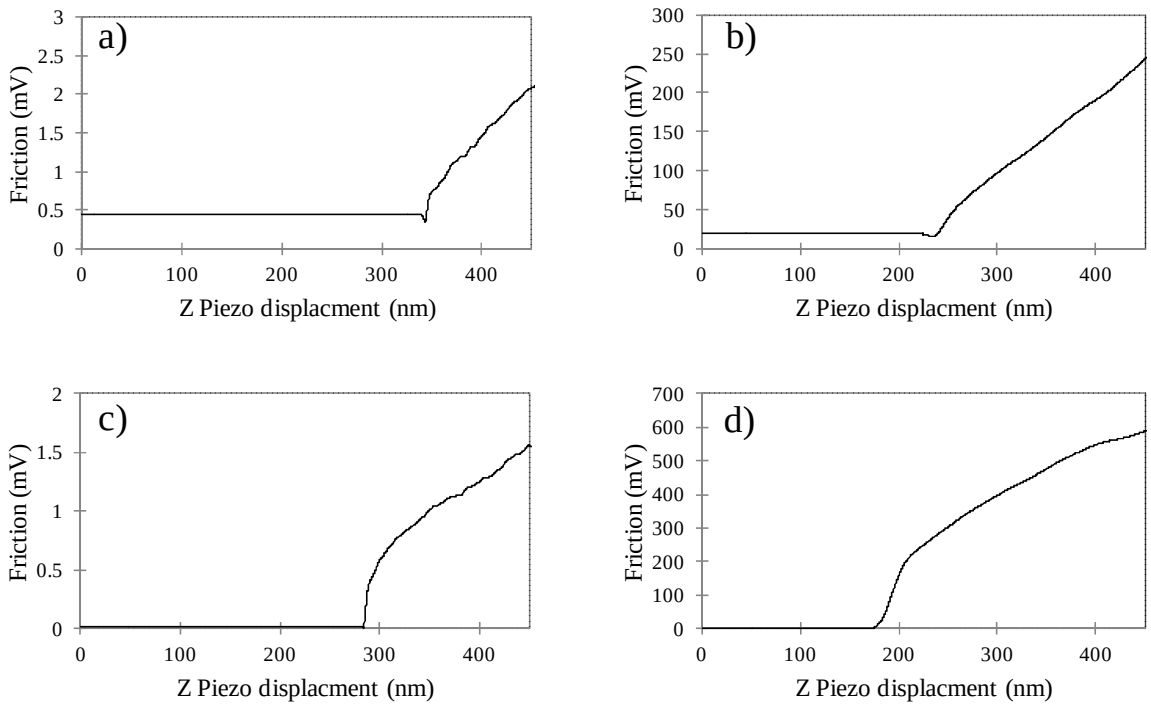

Figure 4.5: Friction spectra obtained with the Circular mode on hydrophilic mica (a and c) and glass (b and d) surfaces at high sliding velocities (curves a and b) and at low sliding velocities (curves c and d).

For hydrophilic surfaces (Fig. 4.5), at low sliding velocities, the curves deviate from a linear trend at low normal loads when the tip is close to the snap-off, whereas at high sliding velocity, the linear dependence is clear. The divergence observed on the hydrophilic surfaces at low sliding velocities could be attributed to the capillary meniscus that disturbs the measurements at very low load. This disturbance is not observed in the case of hydrophobic surfaces as no capillary meniscus is formed.

3. Friction force versus ln (V) at a constant normal load

Figure 4.6 represents the friction force versus the load at different sliding velocities obtained with the Circular mode on a CVD gold surface (R_a = 0.23 nm). (Not all curves have been represented for visual clearance).

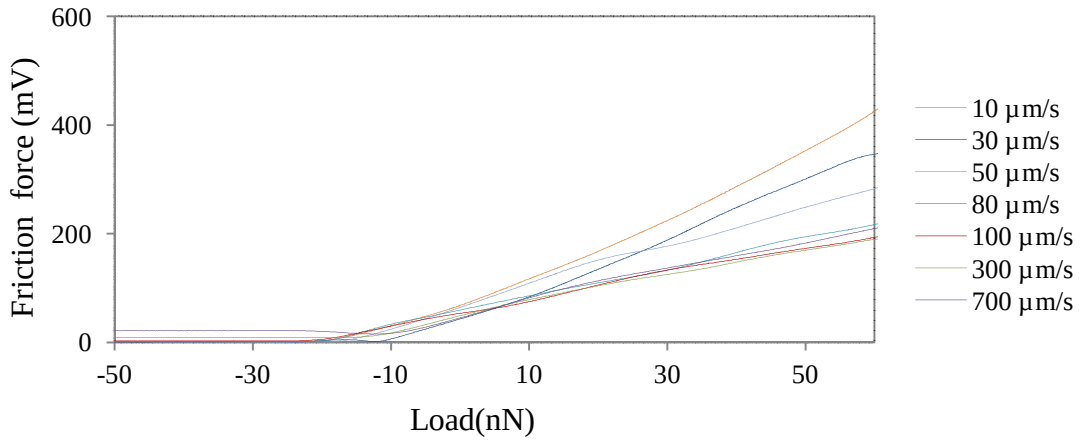

Figure 4.6: Friction spectrum (friction force vs normal load) on a hydrophilic gold surface (static contact angle with water 75°, roughness R_a = 0.23 nm). The results are obtained with a silicon nitride probe (R ≈ 30°) of stiffness k_N = 0.5 N/m, and at relative humidity of 33%.

When varying the sliding velocity, a linear dependence of the friction force on the load is observed at each velocity (the Amontons law is verified). In addition, the slope of the friction versus load curve is decreasing as the sliding velocity is increased. Figure 4.7 represents the variation of the friction force with the logarithm of the sliding velocity at normal constant loads for a CVD gold (R_a = 0.23 nm).

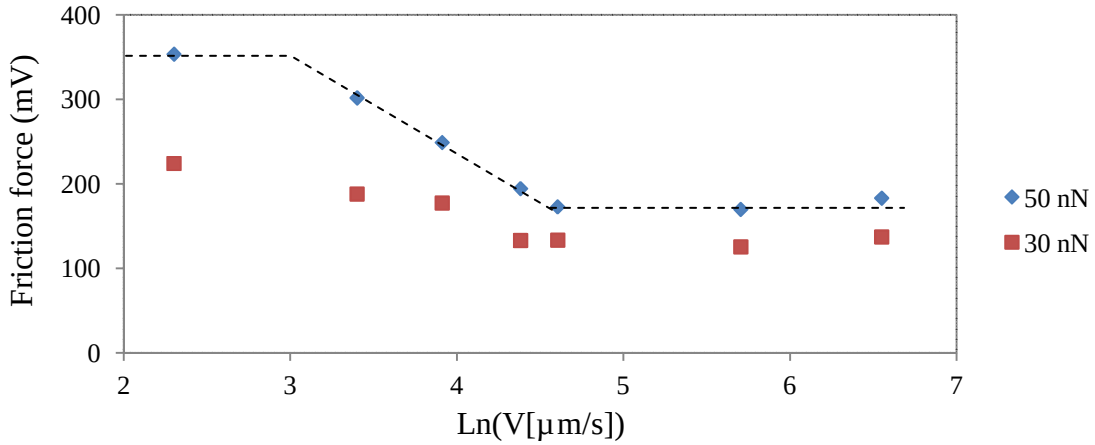

Figure 4.7: Variation of the friction force with the logarithm of the sliding velocity at two different constant normal loads on a gold surface (static contact angle with water 75°, roughness R_a = 0.23 nm). The results are obtained with a silicon nitride probe (R ≈ 30°) and at humidity of 33%. The data are obtained from Figure 4.6.

Three regimes are observed for the trend of friction force with the sliding velocity as it was for the variation of the adhesion force. The linear decrease of the friction force in the intermediate regime has already been observed by Riedo et al [7]. They attributed it to a decrease of the capillary adhesion. Experiments in the previous chapter, experimentally confirm this assumption.

Figure 4.8 represents the variation of the friction force with the load for a freshly cleaved HOPG surface (R_a = 0.05 nm) at different sliding velocity.

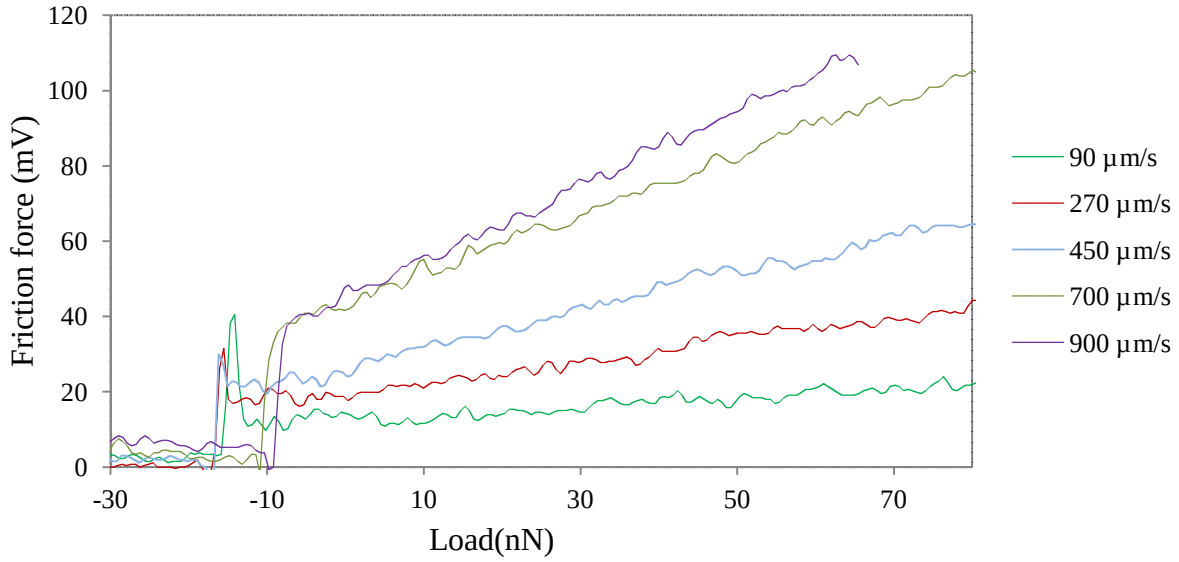

Figure 4.8: Friction spectrum (friction force vs normal load F_N) on a hydrophobic freshly cleaved HOPG surface (static contact angle with water 104°, roughness R_a = 0.05 nm). The results are obtained with a silicon nitride probe (R ≈ 30°), of stiffness k_N = 0.5 N/m, and at relative humidity of 38%.

As for the CVD gold surface (Fig.4.6), the friction dependence on the load follows an Amontons law and the slope is also varying. However, the slope is increasing in this case, and it was decreasing for gold.

Figure 4.9 represents the variation of the friction force with the logarithm of the sliding velocity at normal constant loads for a freshly cleaved HOPG surface (R_a = 0.05 nm).

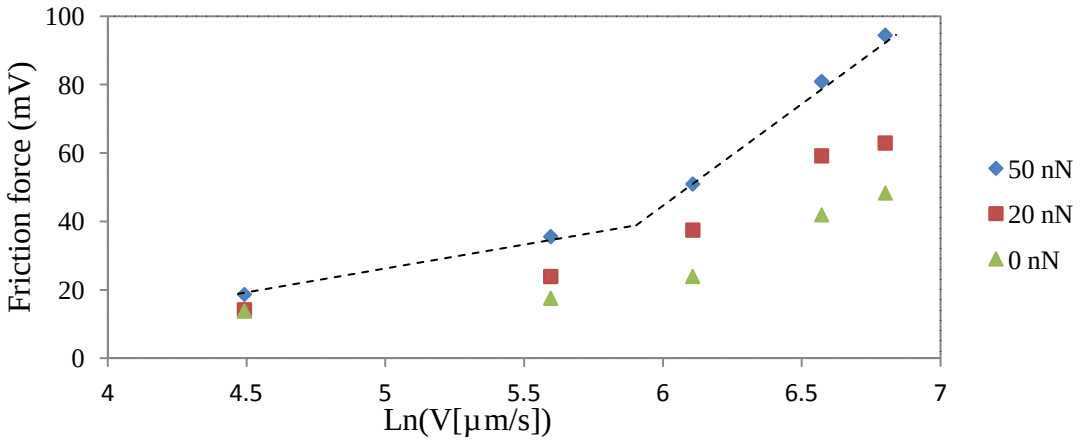

Figure 4.9: Variation of the friction force with the logarithm of the sliding velocity at three different constant normal loads on a freshly cleaved HOPG surface (static contact angle with water 104°, roughness R_a = 0.05 nm). The results are obtained with a silicon nitride probe (R ≈ 30°) and at a humidity of 38%. The data are obtained for Figure 4.8.

The results show two regimes in which the friction force increases linearly with a logarithmic increase of the sliding velocity. The increase of the friction force can be attributed to stick-slip phenomenon. Authors in ref [147] also propose that it could be attributed to a restructuration of the water molecular film under the contact.

Finally, we present in Figure 4.10, the variation of the friction force with the load for a freshly cleaved atomically flat mica surface (R_a = 0.03 nm) at different sliding velocity.

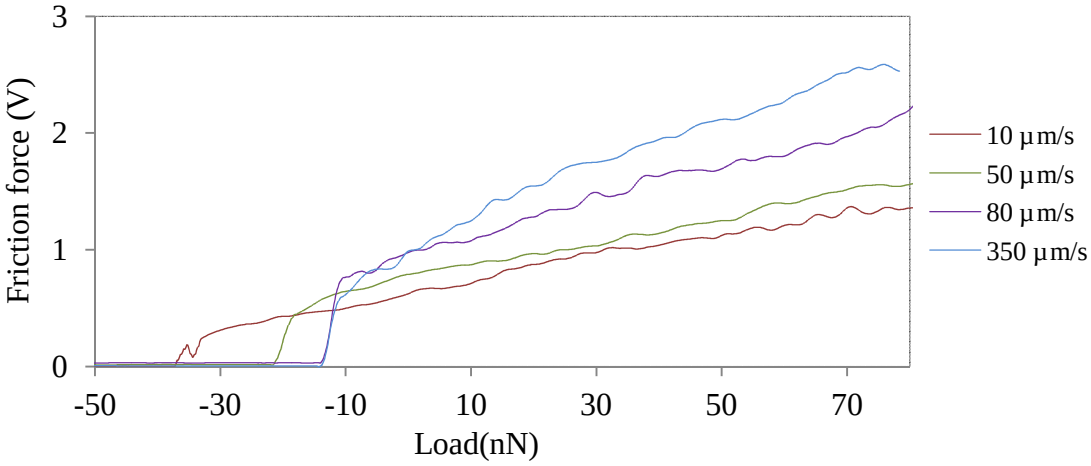

Figure 4.10: Friction spectrum (friction force versus normal load F_N) on a hydrophilic freshly cleaved mica surface (static contact angle with water 5°, roughness R_a = 0.03 nm). The results are obtained with a silicon nitride probe (R ≈ 30°), of stiffness k_N = 0.5 N/m, and at relative humidity of 35%.

As for the atomically flat hydrophobic surface (Fig. 4.8), Figure 4.10 shows for an atomically flat mica surface, a slope that is increasing with the sliding velocity and the Amontons law is still verified

The variation of the friction force at a constant load with the logarithm of the sliding velocity on a mica surface is represented in Figure 4.11.

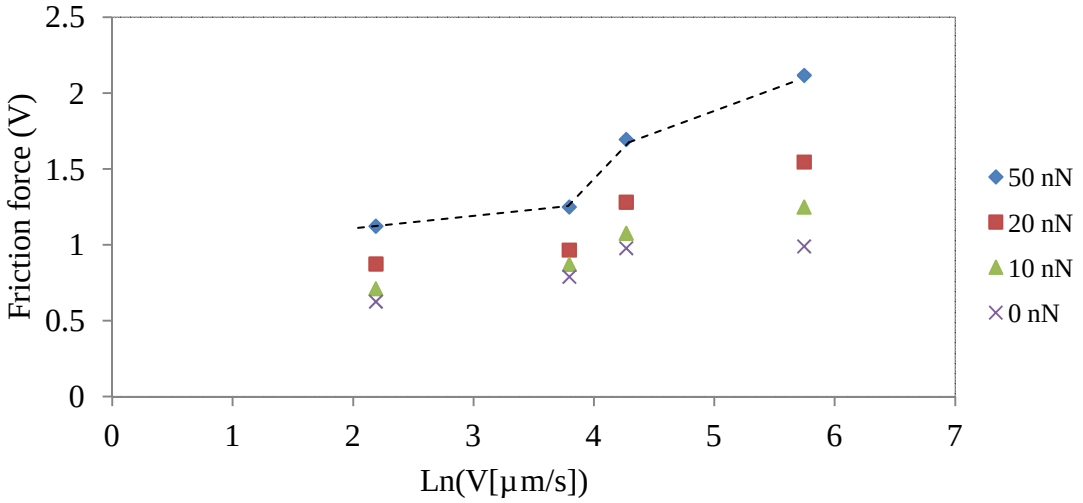

Figure 4.11: Variation of the friction force with the logarithm of the sliding velocity at three different constant normal loads on a mica surface (static contact angle with water 5°, roughness Ra = 0.03 nm). The results are obtained with a silicon nitride probe (R ≈ 30°) and at humidity of 35%. The data are obtained for Figure 4.10.

Figure 4.11 shows an increase of the friction force with a logarithmic increase of the sliding velocity. This trend was also observed by Riedo et al. [83] and it was attributed to stick-slip phenomenon as they assumed that for a monoasperity contact as for a mica surface, capillary adhesion is not velocity dependent. We experimentally showed in the previous chapter that this latter assumption is not valid.

Finally, for hydrophobic or hydrophilic surfaces, the trend of the friction force with the sliding velocity seems to be related either to a stick-slip phenomenon (when the friction force is increasing) or to the capillary adhesion (when the friction force is decreasing). However, the case of an atomically flat hydrophilic mica surface is interesting as it shows that friction force is increasing with the sliding velocity while the adhesion force is decreasing.

In the next section, we propose to investigate this role through the variation of the friction coefficient with the sliding velocity.

4. Variation of the friction coefficient with the sliding velocity

The Circular mode allows computing directly the friction coefficient from the friction spectrum obtained at different sliding velocity, if a linear dependence of friction with the load is verified. All friction coefficient values reported in this section are taken on the linear part of the force spectra (section 4-2).

Figure 4.12 to 4.16 represent the variation of the friction coefficient with the logarithm of the sliding velocity for various surfaces as a gold (R_a = 0.23 nm), glass (R_a = 0.17 nm), HOPG (R_a = 0.05 nm), and mica (R_a = 0.03 nm).

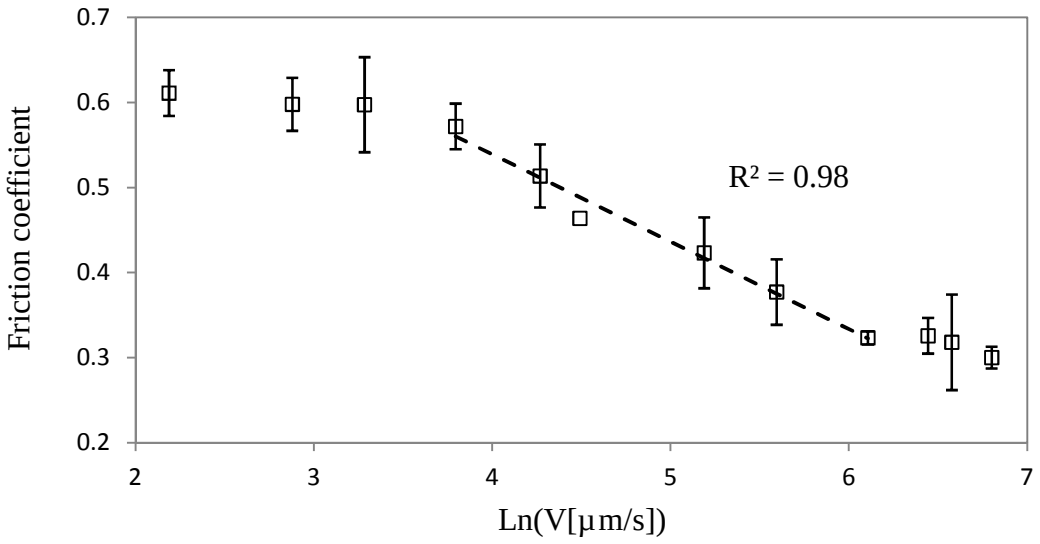

Figure 4.12: The variation of the friction coefficient with the logarithm of the sliding velocity on a gold surface (static contact angle with water 75°, roughness R_a = 0.23 nm). The experiment was carried out with a silicon nitride probe (R ≈ 30 nm) at a relative humidity RH = 41%. The best fit in the intermediate regime is given by a linear fit. The R-squared value, R^2 correspond to the best linear fit of the intermediate regime.

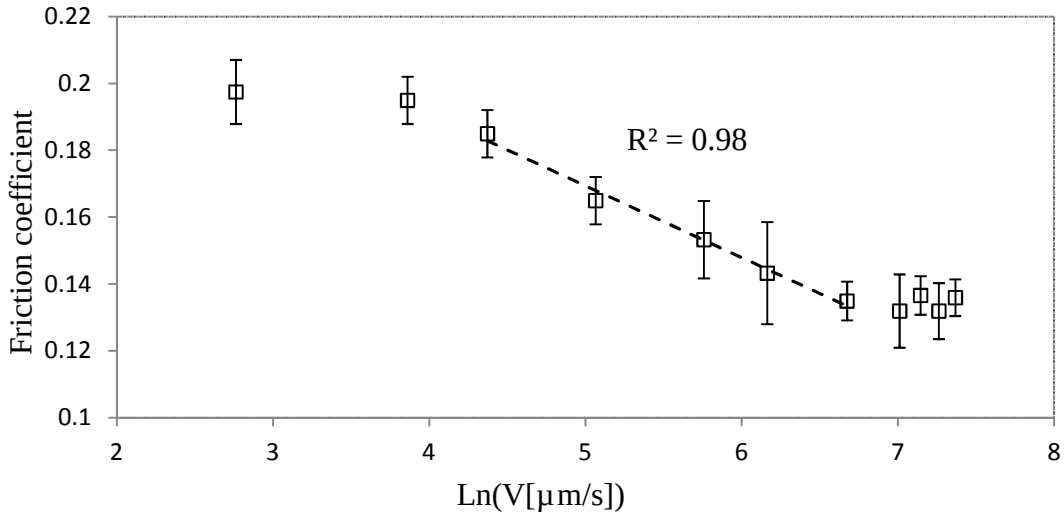

Figure 4.13: The variation of the friction coefficient with the logarithm of the sliding velocity on a glass surface (static contact angle with water 25°, roughness R_a = 0.16 nm). The experiment was carried out with a silicon nitride probe (R ≈ 30 nm) at a relative humidity RH = 38%. The best fit in the intermediate regime is given by a linear fit. R-squared values R^2 correspond to the best linear fit of the intermediate regime.

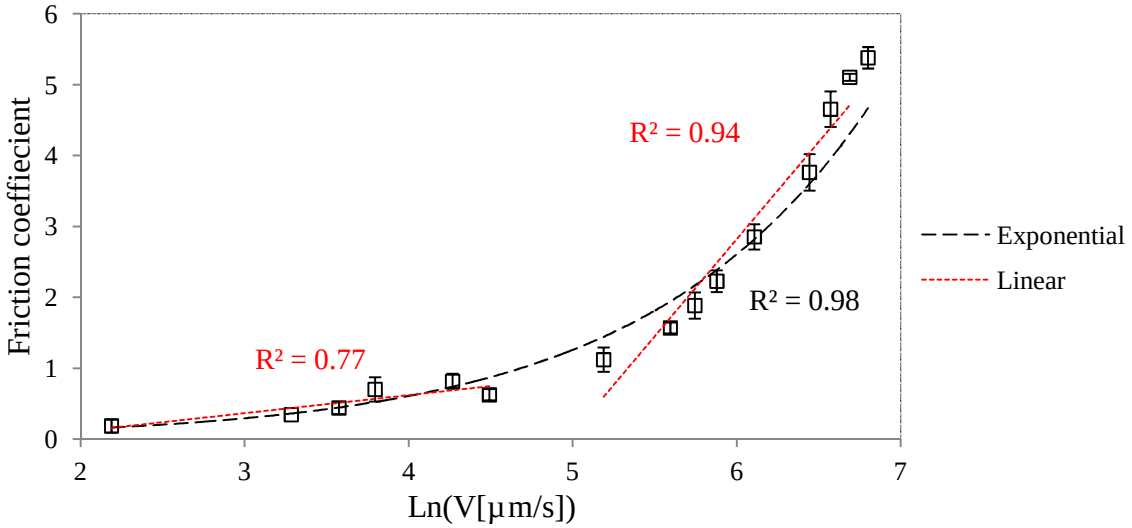

Figure 4.14: The variation of the friction coefficient with the logarithm of the sliding velocity on a freshly cleaved HOPG surface (static contact angle with water 104°, roughness R_a = 0.05 nm). The experiment was carried out with a silicon nitride probe (R ≈ 30 nm) at a relative humidity RH = 34%. The best fit (R^2) is given by an exponential.

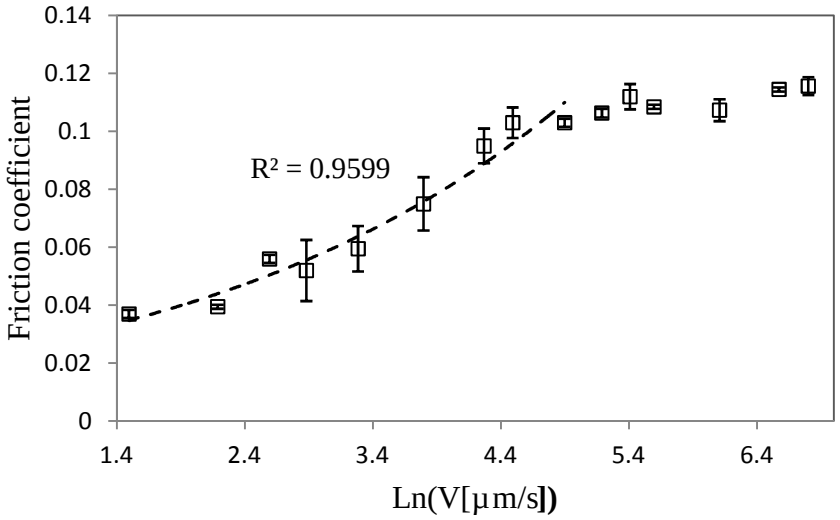

Figure 4.15: The variation of the friction coefficient with the logarithm of the sliding velocity on a freshly cleaved mica surface (static contact angle with water 5°, roughness R_a = 0.03 nm). The experiment was carried out with a silicon nitride probe (R ≈ 30 nm) at a relative humidity RH = 42%. The best fit is given by an exponential.

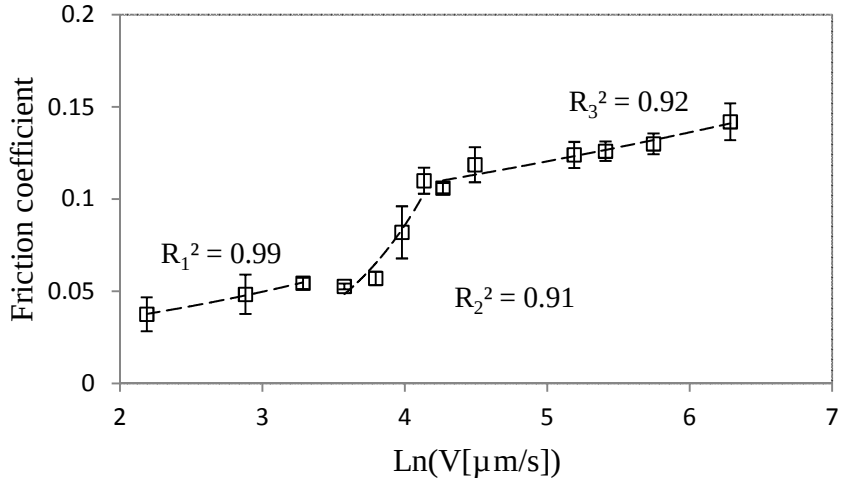

Figure 4.16: The variation of the friction coefficient with the logarithm of the sliding velocity on a freshly cleaved mica surface (static contact angle with water 5°, roughness Ra = 0.03 nm). Experiments were carried out with a silicon nitride probe (R ≈ 30 nm) at a relative humidity RH = 42%. The three regimes can be fitted separately by an exponential that fits best.

In the case of a rough hydrophilic contact (R_a > 0.1 nm), we show that the variation of the friction coefficient with the sliding velocity follows three regimes as in the case of capillary adhesion, (Fig. 4.12 and Fig. 4.13). In the intermediate regime the friction coefficient decreases linearly with the logarithm of the velocity.

However, for smooth hydrophilic surfaces, as freshly atomically flat mica (Ra = 0.03 nm) the friction coefficient increases with the sliding velocity following two or three regimes (Fig. 4.15 and Fig. 4.16); these regimes can be fitted separately by an exponential or linear functions. However, further experiments should be conducted to decide. It is worth noticing that three trends could also be observed on the friction force vs sliding velocity curve in figure 4.11, at a normal load of 50 nN.

The case of an atomically flat HOPG hydrophobic surface (R_a = 0.05 nm) shows that the friction coefficient increases linearly with the sliding velocity (the best fit in Fig. 4.14 is given by an exponential).

Finally, our results show that the friction coefficient is affected by both the roughness of the surface and by the capillary adhesion. A comparison between the behavior with the sliding velocity of the friction coefficient and the capillary adhesion should bring new insights to explain this interplay.

5. Interplay between capillary adhesion and dissipation in a contact

Adhesion force and friction coefficient variations are represented for two different hydrophilic surfaces and hydrophobic surfaces with different roughnesses (Fig. 4.17 to 4.20). On the graphs, the abscissa axis is similar for both quantities (adhesion and friction coefficient), whereas the ordinate axis depend on the parameter that is represented.

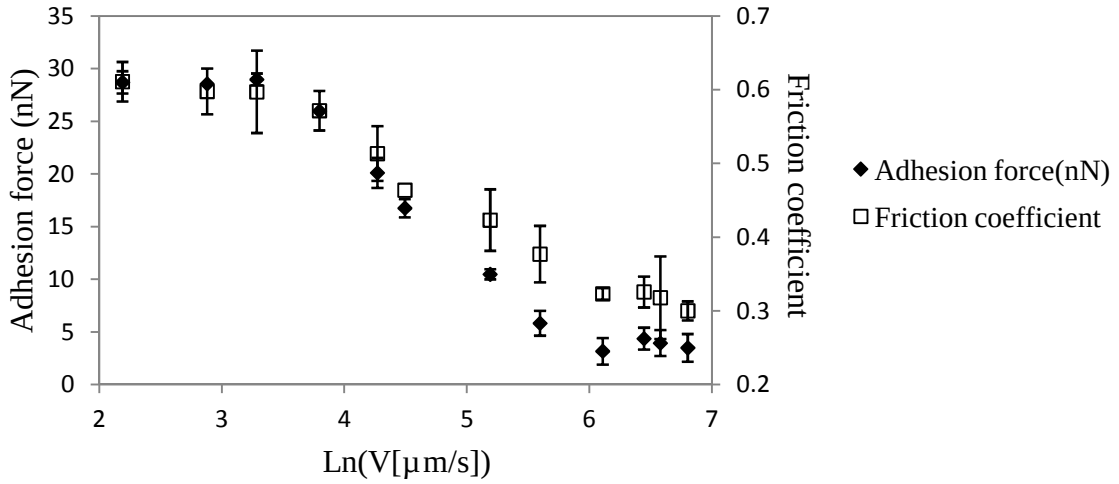

Figure 4.17: Variation of the friction coefficient and the adhesion force with the logarithm of the sliding velocity on a gold sample (R_a = 0.23 nm). The experiment was carried out with a silicon nitride probe (R ≈ 30 nm) at a relative humidity RH = 42%.

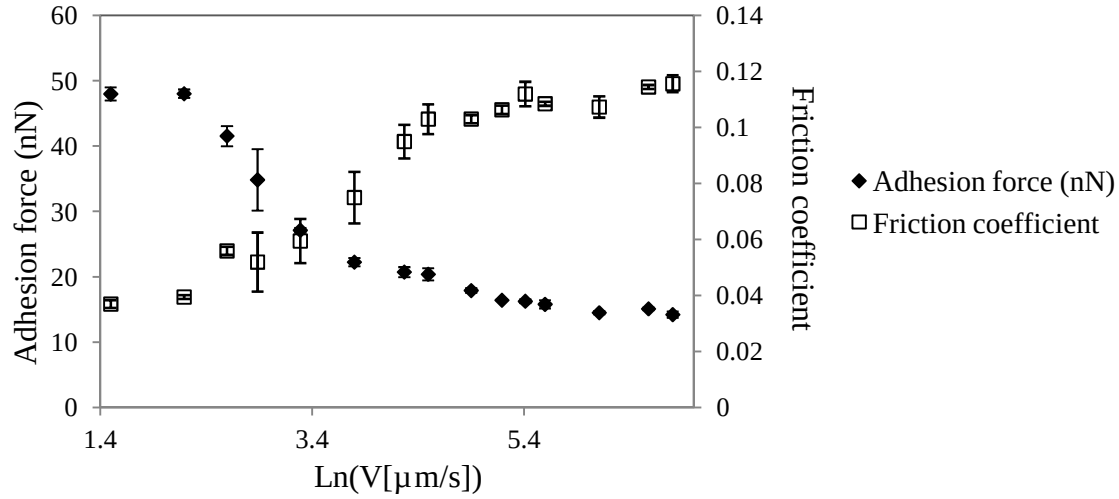

Figure 4.18: Variation of the friction coefficient and the adhesion force with the logarithm of the sliding velocity on a freshly cleaved mica sample. The experiment was carried out with a silicon nitride probe (R ≈ 30 nm) at a relative humidity RH = 40%.

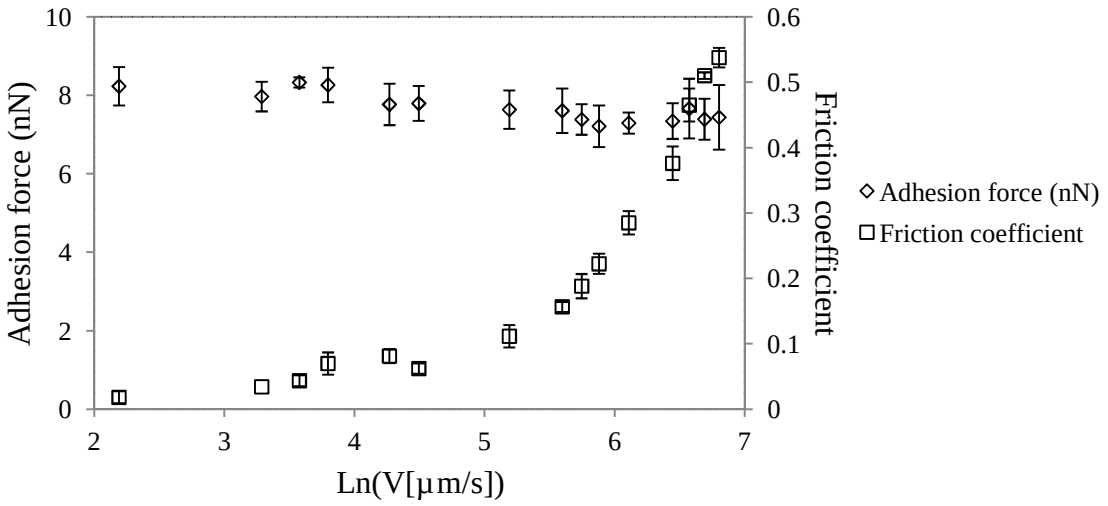

Figure 4.19: Variation of the adhesion force and the friction coefficient with the logarithm of the sliding velocity on a freshly cleaved HOPG sample. The experiment was carried out with a silicon nitride probe (R ≈ 30 nm) at a relative humidity RH = 38 %.

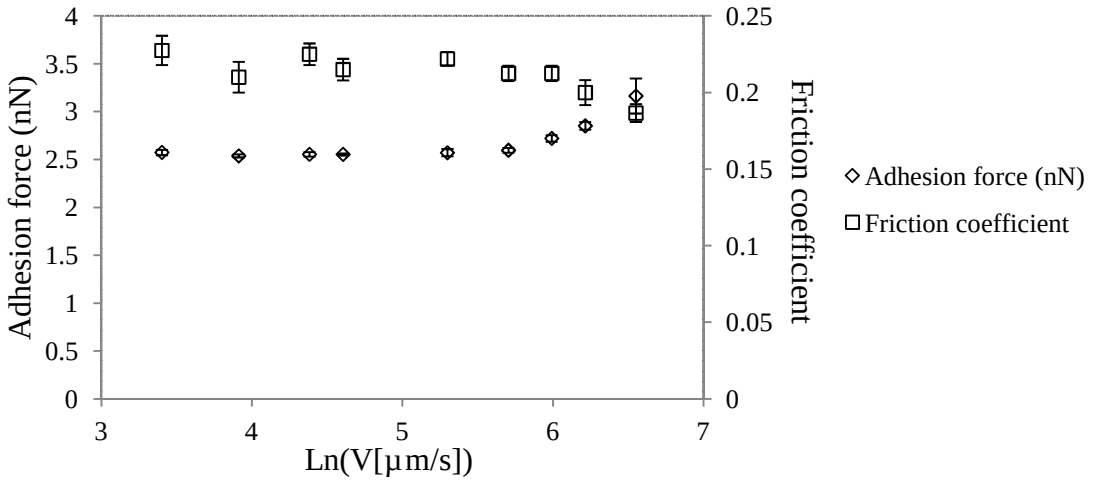

Figure 4.20: Variation of the friction coefficient with the logarithm of the sliding velocity on a silicon wafer grafted CH_3 (Si_{CH3}) surface (static contact angle with water 98°, roughness R_a = 0.2 nm). The experiment was carried out with a silicon nitride probe (R ≈ 30nm) at a relative humidity RH = 40%.

In the case of hydrophilic surfaces, it is clearly shown that the variation of either the adhesion force or the friction coefficient follows three regimes in parallel (Fig. 4.17 - 4.18).

However, for the case of hydrophobic surfaces, while the adhesion force is velocity independent, the friction coefficient is linearly increasing with the sliding velocity for atomically flat HOPG surface (Fig. 4.19) (the best fit for Fig. 4.14 is given by an exponential), whereas, for rough hydrophobic methyl grafted silicon wafer (Si_{CH3}) surface (Fig. 4.20), the friction coefficient seems to be independent of the sliding velocity.

Discussion

Here, we propose qualitative explanations of the previous observed trends for friction coefficient and related to the behavior of capillary adhesion.

In the case of an atomically flat surface (HOPG), we observe a linear increase of the friction coefficient with the sliding velocity (Fig. 4.14). In this case no capillary meniscus is formed as HOPG is a hydrophobic surface, but a thin layer of water still exists. This confined layer could cause shearing while the probe is sliding on the surface [148] as represented in Figure 4.21.

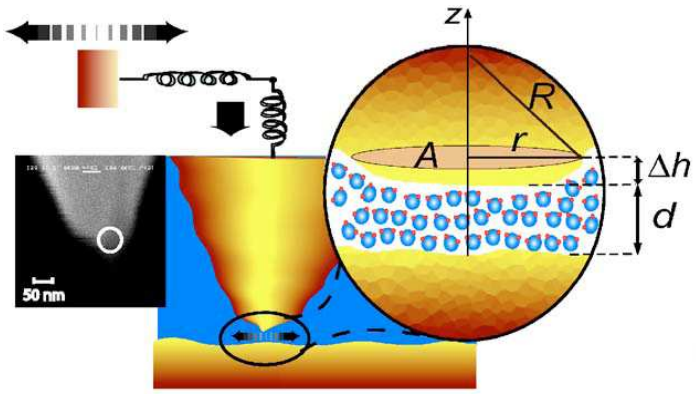

Figure 4.21: AFM used to measure the normal and lateral forces between a nanosize untreated silicon probe and flat solid surfaces (HOPG) in de-ionized water. Fig from ref [148].

From this model, the authors of ref. [148] have expressed the friction coefficient with the viscosity η, the sliding or shearing velocity, V_{shear}, and the thickness of the water film, d :

$$\mu \alpha \eta \frac{V_{shear}}{d} \qquad 4.1$$

Considering that the viscosity of a confined water film is not velocity dependent in the case of HOPG [148], the equation 4.1 predicts a linear increase of the friction coefficient with the sliding velocity, as it was observed in our experimental data. The idea of a structuration of water beneath a contact has also been reported by K.B. Jinesh et al. [147].

In the case of a hydrophilic atomically flat surface such as mica, the friction coefficient is increasing and it follows three regimes as capillary adhesion. In the first regime the friction coefficient slightly increases (this is confirmed on figure 4.16). In the intermediate regime, it is increasing linearly with the sliding velocity while the capillary adhesion is decreasing with the logarithmic increase of the sliding velocity. When the capillary meniscus has vanished (this corresponds to a third regime), a slight increase of the friction coefficient is still observed (this is also confirmed on the experiment reported on Figure 4.22).

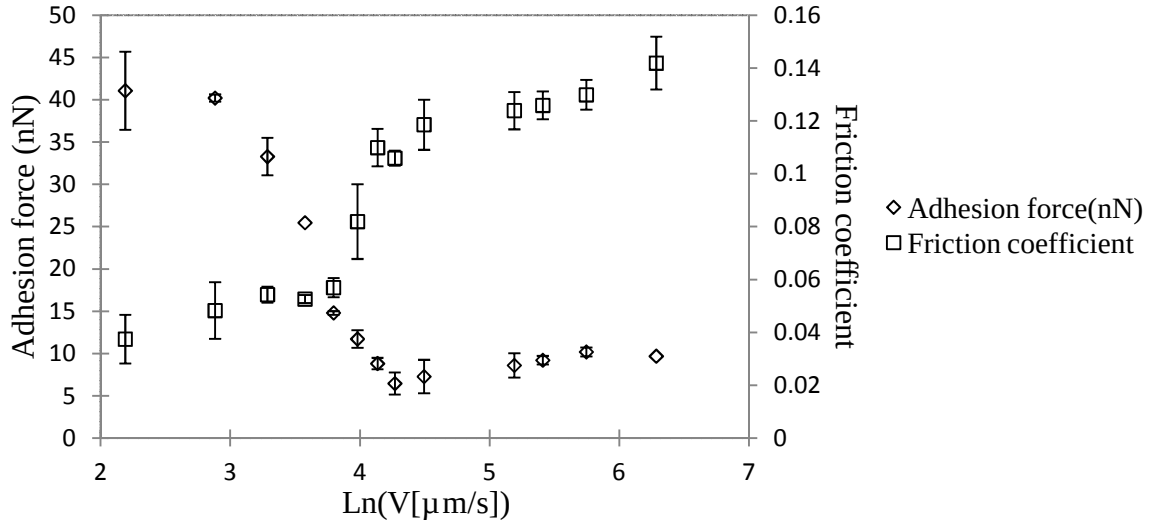

Figure 4.22: Variation of the friction coefficient and the adhesion force with the sliding velocity, on a mica sample with a silicon nitride probe (R ≈ 30 nm) at a relative humidity RH = 42%.

We consider that in the case of the mica surface a thin confined water layer is present as for the case of HOPG, at the difference that a capillary meniscus coexists in the intermediate regime. Therefore, the regimes that are observed for mica could be related to energy dissipation in both the capillary meniscus when existing and the shear thickening of the water layer below the probe. One should not forget that contaminations due to ions dissolved by water for a mica surface may also play a role [149]. Further experiments that could clearly show the trends of the friction coefficient in the first and second regime are required.

For a hydrophilic rough surface, the friction coefficient is decreasing with the logarithm of the sliding velocity and the followed trend is comparable to the adhesion force one. We can assume that the dissipation occurs in the meniscus itself as the water molecules are prisoned in between the asperities and cannot reconstruct. Therefore, while the volume of the capillary meniscus is decreasing, the capillary adhesion is decreasing leading to a change of the nature of the contact and to a decrease of the friction coefficient. However, the non sliding velocity dependence of the friction coefficient in the third regime needs further theoretical and experimental developments to be confirmed and explained.

Finally, on hydrophobic rough surfaces as methyl grafted silicon wafer (Si_{CH3}), the friction coefficient is not sliding velocity dependent while the adhesion force is constant. This trend is similar to the one observed for hydrophilic rough surfaces in the third regime where no capillary meniscus exists. It is worth noting that for high sliding velocities the adhesion force can be seen to slightly increase, and this can be related to the in-homogeneity of the grafting on the surface.

General Conclusion

The scope of this thesis was based on investigating the influence of the sliding velocity on capillary adhesion that is known to play an indirect role in friction mechanisms at the nanoscale. This goal was reached by implementing an innovative experimental setup called the "AFM Circular mode " to the commercial AFM. The Circular mode allowed us to overcome the limitation encountered with the commercial AFM, by offering capabilities to perform measurements in a stationary state, and with high sliding velocities. An advantage was the possibility to combine the Circular mode to the force mode (the vertical scanning velocity was set to 0.1 µm/s), allowing to obtain force distance spectra (adhesion force) while the probe is sliding on the surface. Experiments were conducted at ambient conditions on various types of surfaces. The obtained results showed no dependence of the adhesion force on the sliding velocity for the case of a hydrophobic surface (HOPG, methyl grafted silicon wafer), whereas for the case of a hydrophilic surface (freshly cleaved mica surface, gold, silicon wafer, silicon nitride, glass), a decrease of the adhesion force with the sliding velocity was observed. In the latter case, the observed decrease of the adhesion force with the logarithm of the sliding velocity follows a three regime trend; Regime I, at low sliding velocities, the adhesion force is a contribution of capillary and van der Waals forces; Regime III, at high sliding velocities, the adhesion force is a contribution of the van der Waals or attractive forces only, and the capillary forces have vanished. Regime II, at intermediate sliding velocities the adhesion forces decreases linearly with the logarithm of the sliding velocity starting from a threshold sliding velocity V_{start}. We experimentally showed that V_{start} decreases with an increase of either the humidity or the hydrophilicity of the surface, that are both environmental parameters on which the volume of the capillary meniscus in its equilibrium state depends.

A somewhat similar behavior has been previously observed by *Riedo et al. [7]* for a study of the friction force with the sliding velocity. They reported for the variation of friction force with the logarithm of the sliding velocity a positive slope for partially hydrophobic surfaces, and a negative slope on partially hydrophilic surfaces. They suggested that the overall friction force is given by a superposition of the stick and slip related increase, and a thermally activated nucleation process in the gaps of a multi-asperity contact related decrease of friction with velocity. However, for atomically flat mica which is a hydrophilic surface, it was

assumed that on this surface there is a mono-asperity contact in which no nucleation of the capillary meniscus can occur and the friction force increases with the sliding speed due to the domination of stick slip process.

However, we also performed experiments on a mica surface, and we found a decrease of the adhesion force with the logarithm of the sliding velocity. These observed behaviors are not explicable by a nucleation process.

To address this issue and to explain, the logarithmic dependence of the adhesion force on the sliding velocity, and the dependence of V_{start} with the hydrophilicity of the surfaces and the humidity, we developed a model based on a thermally activated growth process, in which the capillary meniscus nucleates and grows from the probe-sample contact. In this model, we consider that water molecules have to overcome a distribution of energy barriers to condensate. These energy barriers are resulting from local defect as atomic roughness or chemical heterogeneities encountered at the perimeter of the wet contact area while the meniscus is growing. The total energy barrier is therefore assumed to be proportional to the perimeter and can be expressed as a function of environmental parameters (hydrophilicity of the surface, and relative humidity). Our model based on the growth process clearly justifies the obtained experimental results.

In this first part we clearly, experimentally, showed that capillary adhesion is sliding velocity dependent. In particular, a control of the volume of the meniscus or indirectly the capillary force may lead to a control of the nanotribological properties of the surfaces. This control may be operated for example, in modulating the temperature of the contact [8] or in designing nanostructured materials made of patches with different hydrophilic properties.

Based on our results, we found it interesting to explore how capillary adhesion may affect the friction mechanisms. To achieve the goal of studying the interplay between capillary adhesion and sliding friction, we used the Circular mode that can be combined to the force mode to extract rapidly the dependence of friction force on the load. An average friction force can be measured while the probe is sliding in a circular motion and while normal load varies due to the vertical motion of the probe. The obtained dependency on various substrates validates the Amontons law for all surfaces used in our experiments. From the curves, we noticed that the slopes of the friction spectra were changing with the sliding velocity. So by studying the friction force versus the sliding velocity at a constant normal load we observed that the friction force is decreasing for hydrophilic rough surfaces, whereas it is increasing for atomically flat hydrophilic or hydrophobic surfaces. In addition, the friction coefficient can be measured directly. Therefore, we investigated the influence of the sliding velocity on the

friction coefficient, and a decrease following three regimes, similar to the sliding velocity dependence of the capillary adhesion, was observed for hydrophilic surfaces that possess a roughness higher than 0.1 nm. Whereas, an increase of the friction coefficient was observed on atomically flat surfaces that posses a roughness lower than 0.1 nm.

In purpose of finding a correlation, the variation of the friction coefficient with the sliding velocity was compared to the variation of the adhesion force with the sliding velocity. Nevertheless, it is often assumed that the friction coefficient should increase with the sliding velocity, here in our experiments we show that it is not always the case, and that different parameters such as roughness or capillary adhesion can play a role. However, the mechanisms governing these behaviors of the friction coefficient with the sliding velocity are still no clear.

To better comprehend these mechanisms further studies should be conducted that relay on the innovative experimental set-up and the clear understanding of the interplay between friction and capillary adhesion with the sliding velocity.

Annex 1. Atomic Force Microscopy

1. Principle of the AFM

Binnig, Quate and Gerber invented the first Atomic Force Microscope (AFM) in 1986 [52]. The first commercially available Atomic Force Microscope was introduced in 1989. The AFM is one of the foremost tools for measuring interaction forces at the nanoscale between a nanometer sized probe and a surface. It is dependent on, i) the probe that is the most sensitive component, which is composed of a nanometer sized tip attached to the end of a cantilever, and it interacts directly with sample surface, ii) the photo detector that senses the angular deflection of the reflected laser beam due to the deflection of the cantilever following the probe-sample interaction, iii) the feedback loop that controls the separation distance between the surface and tip in order to keep the cantilever deflection or the interaction forces constant, iv) and the 3D scanner that permits accurate and precise relative displacements of the probe or sample, down to 10 pm. A schematic diagram of the AFM is represented in (Fig. A1.1).

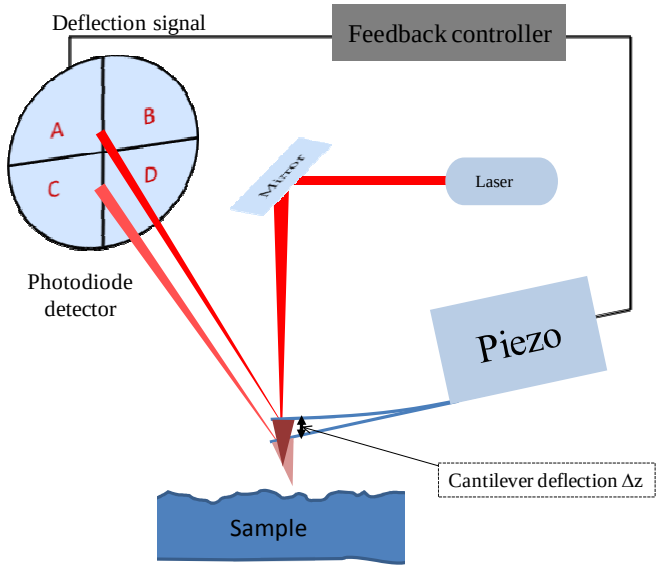

Figure A1. 1: Schematic diagram of a scanned-probe AFM. In the case of scanned sample, it is the tip that is scanned instead of the probe. The components are Laser diode, cantilever, mirror, position-sensitive photodetector, feedback electronics, and scanner.

2. The AFM probe – Measuring interaction forces

The AFM probe composed of a nanometer sized tip mounted on to the end of a cantilever, the approach into close contact with the sample make it one of the most important units of the AFM apparatus.

When the first AFM was made, a very small diamond fragment was carefully glued to one end of a tiny piece of gold foil. Today, the tip–cantilever assembly is typically fabricated from silicon or silicon nitride by using technologies such as Silicon micromachining techniques that are based on a series of deposition, photolithography, and etching steps. The use of these techniques for fabrication of AFM probes, benefited the scientists by the low cost of fabrication, the simultaneous batch fabrication of thousand of cantilevers, and the sharper tips obtained [150, 151]. Based on the sharpness of the tip measured by the radius of curvature, the shape of the tip that is generally either a pyramid, a cone or a ball, with radius values up to 90 nm, and the cantilever resonant frequency (depending on the type of operation selected: contact or non-contact mode), The cantilever assembly contribute in obtaining good uniformity of characteristics and reproducibility of results.

There are essentially two designs for cantilevers, the triangular or "V" shaped and the single-arm kind (Fig. A1.2). The length, width, and thickness of the beam(s) determine the mechanical properties of the cantilever and have to be chosen depending on the mode of operation needed and on the sample being investigated. Cantilevers are essentially classified by their force (or spring) constant and resonance frequency: low-resonance frequency cantilevers ("V" shaped, with spring constant ranging from 0.06 to 0.35 N/m, and a resonant frequency ranging from 18 to 65 KHZ) are more suitable for imaging in contact and resonance mode (Tapping Mode™) in liquid, whereas stiff and high-resonance frequency cantilevers (single-arm kind, with spring constant of about 40 N/m, and a resonant frequency about 300 KHz) are more appropriate for resonance mode (Tapping Mode™) in air [152].

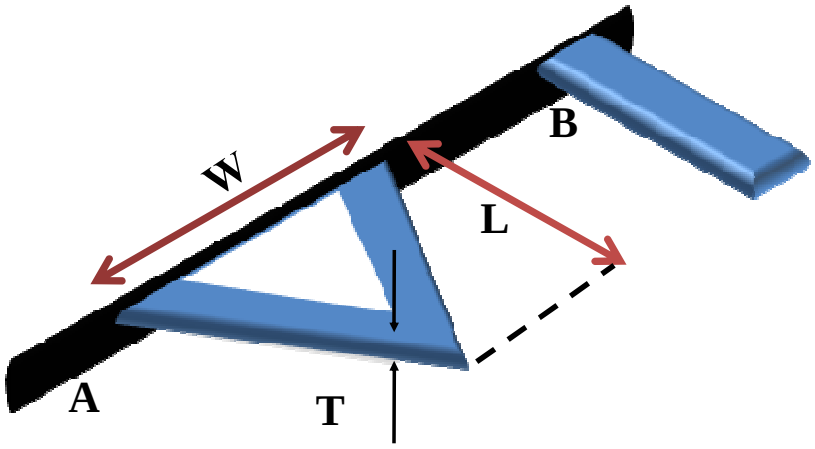

Figure A1. 2: Triangular (A) and single-beam (B) cantilevers. The mechanical properties, such as the force constant and resonant frequency, depend on the values of width (W), length (L), and thickness (T).

Various techniques have been applied to the calculation of cantilever spring constants for AFM applications. Methods that have been used for this purpose include dimensional techniques, which are based on the cantilever's material properties, geometry, and dimensions [153], methods in which the spring constant is calculated by adding mass to the probe [154], techniques that require pressing the probe against a very stiff surface and subsequently against a reference spring of known compliance [155]; and thermal methods, which treat the cantilever as a simple harmonic oscillator [156, 157].

The probe senses the interaction forces acting between the tip and the sample, that result in deflections of the cantilever, the normal forces act on the tip and deflect the cantilever up or down, and also the lateral ones (i.e. friction) which tend to twist (torsion) the cantilever. Moreover, the magnitude of the deflection of the cantilever, with the knowledge of the normal cantilever stiffness (k_N), allows the calculation of the value of the interaction forces. As for our measurements (normal and lateral interaction forces), we have conducted them by the use of a silicon nitride probe (Si_3N_4) with a triangular cantilever, and the cantilever stiffness was measured by employing the thermal noise method (Fig. A1.3).

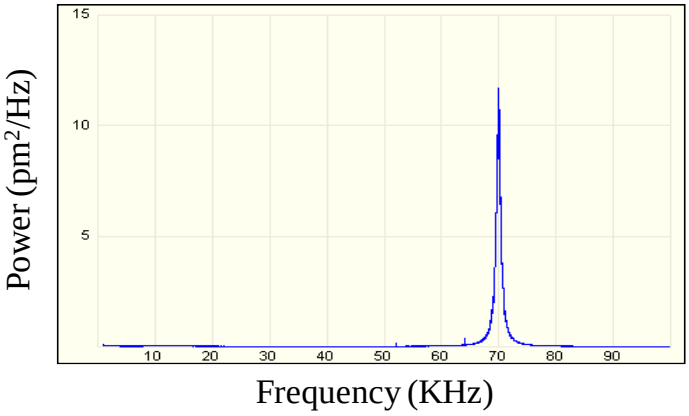

Figure A1. 3: Curve showing the resonance frequency of the cantilever, obtained with a 3100 DI AFM nanoscope controller V from a silicon nitride probe (DNP from Bruker).

3. The Photodiode detector – measuring cantilever deflection

Since the invention of the AFM, methods such as optical inter-ferometry [158, 159], have been proposed to monitor the cantilever deflection. However, due to its accuracy and sensitivity to Angstrom-level movements, the laser beam deflection system continues to be the most widely used [160][14].

In this method, a laser beam is reflected from the backside of the cantilever (often coated by a thin metal layer to increase the reflectivity coefficient) onto a position-sensitive photo detector (PSPD). The photo detector is made of four segment photo detectors that allow detecting the normal and torsion bending of cantilever due to the respective normal and torsional forces acting on the tip (Fig. A1.4).

Any small deflection of the cantilever will tilt the reflected beam and change its position on the photo detector. This leads to a change in the output voltage of the photo diode.[15] Because the distance between cantilever and detector is generally three orders of magnitude greater

14 This same detection system has been used to monitor the cantilever deflection in cantilever-based sensors 161. Brunt, T.A., et al., Measuring surface stress induced by electrode processes using a micromechanical sensor. Journal of the Chemical Society, Faraday Transactions, 1996. ***92****(20): p. 3807-3812.*

15 The forces acting on the cantilever can be deduced from the measurement of the PSPD output voltage, provided that the photo diode sensitivity and the cantilever spring constants are known.

than the length of the cantilever, the amount of bending or torsion of the cantilever is magnified giving rise to an extremely high sensitivity [162].

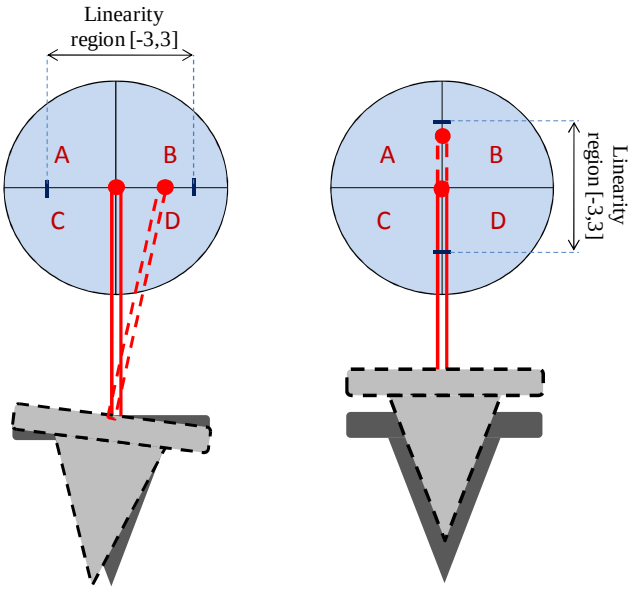

Figure A1. 4: Schematic representation showing the effect of cantilever movement with the photo detector represented by the square with quadrants labeled A, B, C & D. Torsional bending of the cantilever (left) leads to a change in lateral deflection and (right) vertical displacement of the cantilever leads to a change in vertical deflection.

As shown on Figure A1.4, the laser should remain in the range of [-3V, +3V], when the laser is out off this region, effect of nonlinearity is observed and this has previously been cited in [163]. The vertical (Eq. A1. 1) or horizontal (Eq. A1. 2) difference can be computed by the following equation:

$$Normal\ deflection\ = \frac{(A+B)-(C+D)}{(A+B)+(C+D)} \qquad \text{A 1.1}$$

$$Torsional\ deflection\ = \frac{(A+C)-(B+D)}{(A+B)+(C+D)} \qquad \text{A 1.2}$$

The intensity difference between the upper and lower segments of the four-quadrant photodetector is proportional to the normal deflection (topography), whereas the intensity difference between the left and right segments is proportional to the torsion of the cantilever (torsion or lateral force).

4. The Piezoelectric tube

The 3D scanner is present in two configurations: the scanned sample AFM in which the scanner is attached to the sample and it is moved under the tip, or scanned tip AFM in which the piezoelectric scanner is rigidly attached to the probe and moves it over the sample surface which stands still. The AFM scanner consists of piezoelectric materials, usually ceramic actuators. The application of a voltage on the inner and outer surfaces of the ceramics causes there length to increase or decrease, depending on the polarity of the voltage applied. The scanner configuration consists of combining independently five piezoelectric electrodes in a hollow tube that are responsible for the movement along three axes X, Y, or Z.

For a horizontal displacement in the X direction, the two opposite X and -X electrodes are feed by an opposite voltage that causes the piezo-actuator to bend, whereas for achieving a vertical displacement, it is sufficient to apply voltage to the Z electrode that causes the piezo-actuator to extend or retract. However, a nonlinear displacement for the electrodes based on the voltage applied can be observed, which then necessitates a calibration procedure of the piezo-actuator. In our work we have taken advantage of the piezoelectric tube, by applying our own tension signals, which allowed us to generate lateral displacements and to generate the circular motion (Circular mode).

5. The Feedback loop

The AFM not only measures the force on the sample but also uses the feedback to control the force on the sample allowing acquisition of images at very low forces. The feedback loop consists of the tube scanner, the cantilever and the optical lever, and a feedback circuit (a compensation network, which in AFM is a computer program) that monitors the cantilever deflection and attempts to keep it constant by varying the voltage applied to the scanner and hence adjusts the height of the probe or sample. Indeed, features on the sample surface deflect the cantilever, and so the feedback loop keeps the deflection constant by adjusting the probes or the samples height. One point of interest is that the faster the feedback loop can correct deviations of the cantilever deflection, the faster the AFM can acquire images; therefore, a well-adjusted feedback loop should result in performance with a negligible error.

The feedback system must be optimized for each new sample. This is accomplished by adjusting various gains in the AFM’s feedback circuit.

Integral gain and proportional gain control the response time of the feedback loop. The feedback loop tries to keep the output (separation distance between tip and sample) of the AFM equal to the set-point reference chosen. It does this by moving the piezo-actuator along the Z direction (up or down). Piezoelectric transducers have a characteristic response time to the feedback voltage applied. The gains are simply values that magnify the difference read at the detector. This causes the computer to think that the AFM output is further away from the set point reference than it really is. The computer essentially overcompensates for this by sending a larger voltage signal to the Z piezo-actuator than it truly needed. This causes the piezo-actuator to move faster in Z.

On should optimize the 'integral gain' and 'proportional gain' so that the height image shows the sharpest contrast and there are minimal variations in the amplitude image (the error signal).

6. Topographic image and resolution

By monitoring the interaction forces between the tip and the surface when the cantilever is scanned over the sample the image is formed. As mentioned previously the feedback loop gives the AFM advantage of controlling force on the sample, allowing image acquisition at very low forces [160, 164]. The AFM piezo-actuator electric tube moves the tip across the sample or vice versa over consecutive lines to form the image. In particular, the scanner is driven by the AFM electronics across the first line of the scan and back (X-axis) or so called fast-scan direction. It then steps in the perpendicular direction (Y-axis) or so called the slow scan direction[16], to the second scan line, moves across it and back, then to the third line, and so forth they are repeated as many times as the operator needs the image to contains lines. The difference between this pattern and the traditional raster pattern[17] is that the data are not acquired in opposite directions.

While scanning the probe over the surface, the tip or sample is moved up and down depending on the signals sent by the feedback circuit to keep the interaction forces constant, and by storing these vertical signals (vertical displacement of the piezo-actuator) the topographic

16 No data are collected in the perpendicular direction to minimize line-to-line registration errors coming from scanner hysteresis

17 A raster pattern is the rectangular pattern of image capture and reconstruction in television. By analogy, the term is used for raster graphics, the pattern of image storage and transmission used in most computer bitmap image systems.

image is formed (Fig. A1.5) with lines 215 or 512. The collected data are sampled digitally at equally spaced intervals according to the number of data points allocated per line of the scan, which usually range from 256, 512, 1024 or 2048 with recent AFMs. The data is usually represented by colors ranging from black to white across 256 levels corresponding to the information acquired by the microscope (that can be height, force, phase, and so on) (Fig. A1.5).

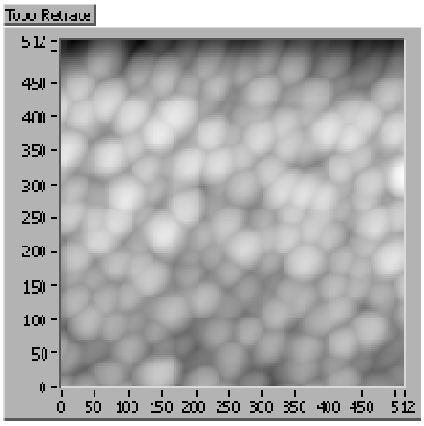

Figure A1. 5: Topographic image with the scale that showing the number of lines (512 in this case) that form the image.

One can extract information from the topographic such as the roughness of the sample (R_a or Rms), when roughness analysis is applied to an image, statistical values are calculated according to the relative heights of each pixel in the image. Regarding basic roughness measurements, average roughness (R_a) is one of the most commonly used roughness statistics.

7. Calibration

Calibration of the lateral force sensitivity is necessary to obtain quantitative friction force measurements with the AFM. Various methods have been introduces for this purpose, and one of the first interesting methods was described by Fujisawa et al. [165]. He used a lateral force curve characterized by a sticking regime and a sliding one to calibrate the sensitivity [166], the calibration depends on establishing a relation between the static part of the loop and the output voltage of the PSPD. However during slippage, the nonlinearities in the piezo-actuator movement and the deformation of the tip make this method inaccurate. Modifications to this method have been introduced by Piétrement et al. [167], who combined a lock-in-amp

technique to the lateral force curve measurements. The calibration method was based on modulated lateral force microscopy related to the exact knowledge of the probes lateral displacement

Ruan and Bhushan [168] suggested in a two-step calibration procedures that friction could be measured by scanning in the direction parallel to the long axis of the cantilever, and then by employing the calibrated normal forces, and assuming a symmetric tip, the frictional force will correspond to the force given by the vertical spring constant multiplied by the vertical piezo-actuator movement needed to keep the cantilever deflection constant. Unfortunately, this method neglects the bending of the cantilever, which has been shown to affect the measured friction force [169, 170], and so it cannot be considered as a quantitative method.

A direct one-step technique was proposed by Feiler et al. [171] to determine experimentally the friction force from the lateral voltage signal. The calibration procedure requires simultaneous measurement of the vertical and lateral deflection of the AFM cantilever due to the direct applied force on a lever attached to the cantilever. Calibration factors for both vertical and lateral deflections can be measured from the constant compatible slopes of the force-distance curves. It's worth mentioning that by employing a similar lever arrangement Toikka *et al.* [172] previously attempted to measure the torsional spring constant from the lever twist due to the gravitational moment exerted on a glass fiber glued perpendicular to the cantilever. However, the value they obtained was several orders of magnitude smaller than their calculated value. Since the cantilever twist due to gravity may readily be shown to be negligible. Others have also proposed methods based on direct application of a force acting on an object (lever) attached to the cantilever [173-178].

Liu et al. [179] proposed an optical geometry approach in which the geometry of the optical path of the laser spot from the cantilever to the photodiode is used. They determine the lateral deflection sensitivity by moving the position sensitive-detector (PSD) of and FFM a known amount in the lateral direction along X in, which is converted to an equivalent lateral tip displacement depending on the optical geometry of the instrument and the cantilever shape, dimensions and material properties (lateral cantilever spring constant). This was the first method proposed which gives a direct measure of the lateral sensitivity of the photodiode. However, the procedure is not easy, and it must be repeated if the optical path is changed.

However, Ogletree *et al.*[39], developed a direct calibration method known by the wedge method, which is the most common way to compute a conversion factor α in N/V to convert

the output detector voltage to friction force [180]. In the wedge method the friction loops are acquired on samples with different well-defined slopes using different applied loads. Since the ratio of normal and lateral forces changes with surface slope, one can obtain α by comparing width and offset of the friction loops on the different slopes, nevertheless, this approach was later refined by others [181-183]. To calibrate our friction measurements we have adopted the method proposed by Ogletree. We will explain our LFM calibration procedure in the following:

First we start by interpreting the LFM signals on (Fig. A1.6), they represent the topographic, and slope and the Lateral force signals obtained on a gold[18] surface. The images are different, and there is no direct relation between the topographic and LFM signals. However, there exists a similarity between the LFM signal and the slope image along the X axis (perpendicular to the main axis of the cantilever).

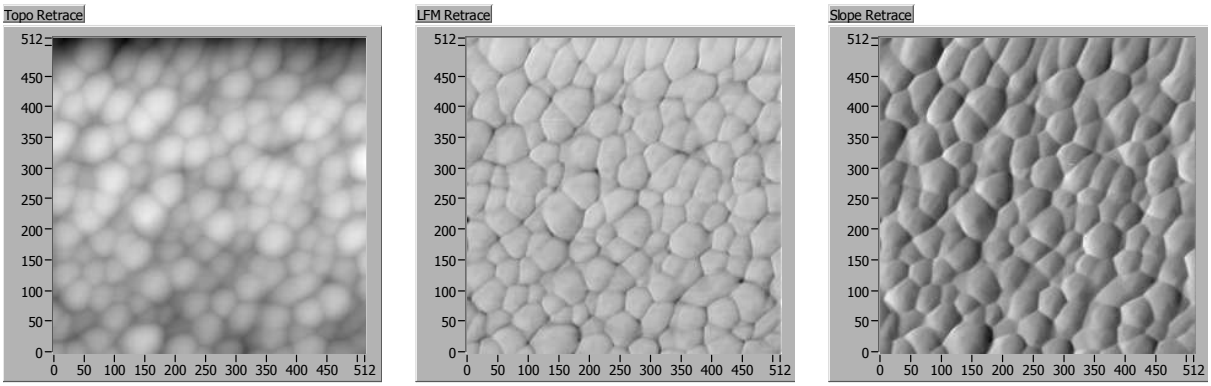

Figure A1. 6: 1 µm × 1 µm topographic image (A), lateral force image (B), and the slope (C) image obtained on a gold surface, by scanning along the X-axis. The image in the trace direction is similar to the observed retrace images.

To realize the calibration of the LFM signals, we commence by a geometrical representation of the contact, and then we represent the forces acting on the probe by decomposing the lateral signal between a sliding probe and a surface (Fig. A1.7). We also denote the sliding direction, by forward from left to right and backwards from right to left.

18 The gold surface was chosen for two reasons: Gold is a noble metal. Thus the appearance of an oxide layer is unlikely, which can affect the local friction properties. And it possesses relatively important local topographic variation.

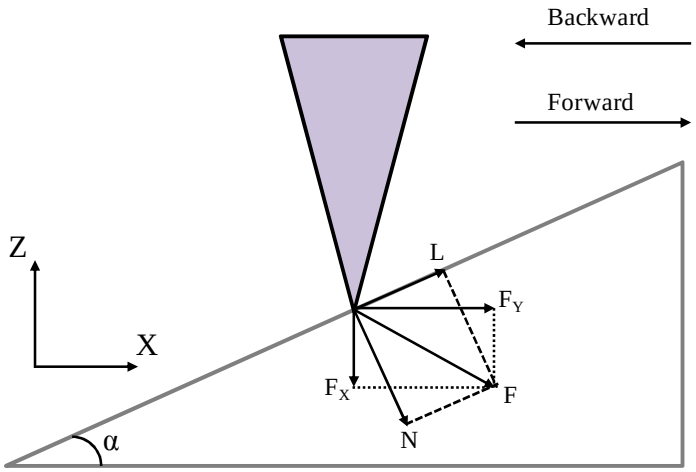

Figure A1. 7: Geometrical representation of the contact between a sliding tip and inclined surface, with the forces acting on the tip.

The total force *F* is the sum of the normal and lateral forces applied on the tip. The force can be decomposed into the components of the X and Z axis in function of the inclination angle α, the components are given by:

$$F_{X\pm} = N\sin\alpha \pm L\cos\alpha \qquad \text{A 1.3}$$

$$F_{Z\pm} = N\cos\alpha \mp L\sin\alpha \qquad \text{A 1.4}$$

where (+) stands for the sliding in the forward direction (uphill) and (–) stands for backwards direction (downhill), by introducing the coefficient of friction μ = *L/N* to the previous equations we get:

$$\frac{F_{X+}}{F_{Z+}} = \frac{\tan\alpha + \mu}{1 - \mu\tan\alpha} \qquad \text{A 1.5}$$

for the signal in the forward direction and

$$\frac{F_{X-}}{F_{Z-}} = \frac{\tan\alpha - \mu}{1 + \mu\tan\alpha} \qquad \text{A 1.6}$$

for the backward direction. Typically, on small scales, the slopes are generally low (<<0.5). So one can neglect the term $\mu\, tan\alpha$ as compared to 1, and the expression for the lateral force resulting from and back and forth sliding is:

$$F_{X\pm} = F_{Z\pm} \tan\alpha \pm \mu F_{Z\pm} \quad \text{A 1.7}$$

The LFM signal is composed of two terms, the $\mu\ F_Z$ term that describes the influence of the friction on the LFM signal, and the term $F_Z\ tan\alpha$ that represents the projection of the normal force of the contact on the X axis. Since we are interested in the friction force, it is possible to separate the two components. When the sliding direction is changed the friction component changes sign, however, the topographic component does not change, by performing the addition and difference of the F_x in both directions, we get parameters which are respectively dependent of the slope of the surface and the friction force.

$$F_{X+} - F_{X-} \approx 2\,\mu F_Z \quad \text{A 1.8}$$

$$F_{X+} + F_{X-} \approx 2\,F_Z \tan\alpha \quad \text{A 1.9}$$

However if we don't neglect the term $\mu\ tan\alpha$, then the expression form (eq. 1.9 and eq. 1.10) becomes:

$$F_{X+} - F_{X-} \approx 2\,\mu F_Z \frac{(\tan\alpha)^2 + 1}{1 - (\mu \tan\alpha)^2} \quad \text{A 1.10}$$

$$F_{X+} + F_{X-} \approx 2\,F_Z \tan\alpha \frac{1 + \mu^2}{1 - (\mu \tan\alpha)^2} \quad \text{A 1.11}$$

However the term $(tan\,\alpha)^2$ is generally very low compare to 1, this leads to the simplified expressions:

$$F_{X+} - F_{X-} \approx 2\,\mu F_Z \quad \text{A 1.12}$$

$$F_{X+} + F_{X-} \approx 2\,F_Z \tan\alpha\,(1 + \mu^2) \quad \text{A 1.13}$$

We saw that the lateral forces are composed of topographic and friction components, now for calibrating the lateral force signal, assuming the LFM signal has a linear relationship with the lateral force, by introducing a calibrating factor we can get:

$$LFM = CF_X + C_0 \qquad \text{A 1.14}$$

The lateral force is composed of two terms,

$$F_{X+} = F_{Z+} \tan\alpha + \mu F_{Z+} \qquad \text{A 1.15}$$

From equations A1.14 and A1.15we obtain,

$$LFM_+ = CF_Z \tan\alpha + C\,\mu F_Z + C_0 \qquad \text{A 1.16}$$

The LFM signal is sensitive to the normal force, the inclination angle of the surface, and the coefficient of friction. However, by assuming the variations of the normal force and the coefficient of friction are negligible compared to the variation of the inclination angle of the surface, equation A1.16 can lead to,

$$\Delta LFM_+ = CF_Z \Delta \tan\alpha \qquad \text{A 1.17}$$

The value of *C* is calculated under the condition of knowing the slope of the surface,

$$\tan\alpha = \frac{\Delta Z}{\Delta X} \qquad \text{A 1.18}$$

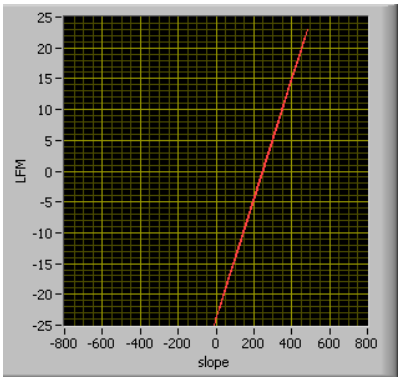

Figure A1. 8: There exists a linear relation between the LFM signal and the local slope of the surface.

In our experimental results, we multiply the resulting calibration factor to the friction force obtained in (V/nm) to convert it to (nN).

Annex 2. Circular AFM mode for investigating polymer nanotribological or nanoadhesive properties

The efficiency of the Circular mode, for investigating nanoadhesive and nanotribolgical surface properties of polymer surfaces was tested. We first performed measurements on a Polydimethylsiloxane (PDMS), which is a visco-elastic silicon based organic polymer. Figure A2.1 shows the variations of the adhesion force and friction coefficient with the sliding velocity.

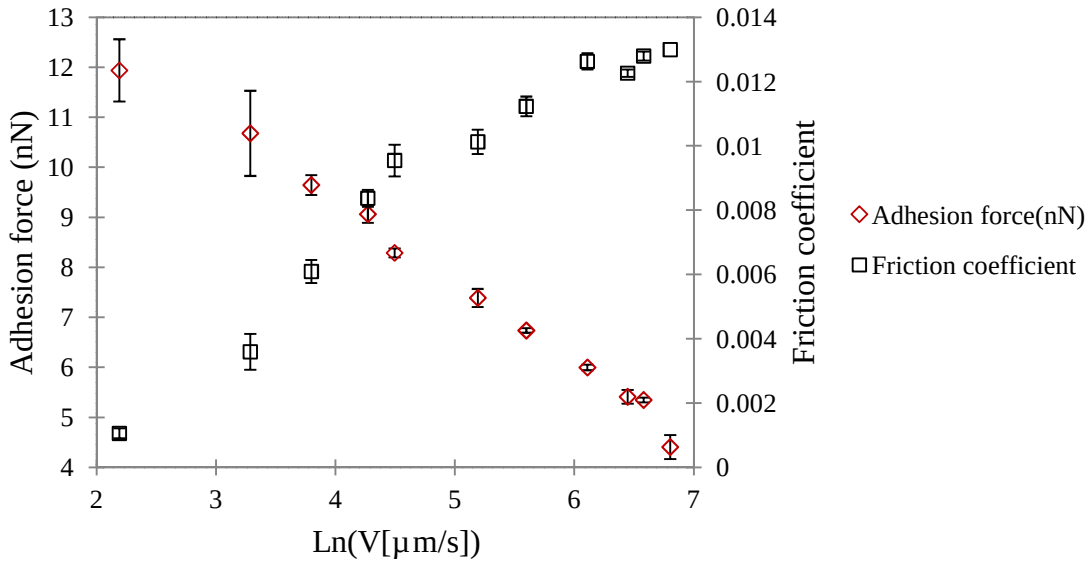

Figure A2. 1: Influence of the sliding velocity on the friction coefficient and on the adhesion force, on a cross-linked PDMS surface. A decrease of the adhesion due to visco-elasticity of the surface, while an increase of the friction coefficient rubber friction.

We notice that the adhesion force is decreasing with the logarithm of the sliding velocity. A simple explanation for the observed behavior can be given based on the visco-elastic

properties of the polymer. The Young modulus of PDMS is typically in the range of 100 kPa to 3 MPa at ambient temperature, and it is velocity dependent. The Young modulus will increase as the velocity is increased. In this case the surface becomes as a more rigid one, and the indentation depth and thus the contact area in between the probe and the surface are decreasing. This decrease of the contact area leads to a decrease of the adhesion force.

Figure A2.1 shows that the friction coefficient is increasing with the increase of the sliding velocity. This behavior has been explained by Bo Persson et al. that consider energy dissipation in rubber friction [184-186]. The friction force between rubber and a hard surface has a contribution commonly described as the hysteretic component. The hysteretic component results from the internal friction of the rubber. During sliding the probe exert oscillating forces on the rubber surface, leading to cyclic deformations of the rubber, and to energy ‘‘dissipation’’ via the internal damping of the rubber.

Further experiments were conducted on a thermoplastic polymer, such as polypropylene, which is a rough (R_a = 36 nm on a 5 µm × 5 µm surface size) and hydrophobic surface (Young modulus is 1 GPa).

The variation of the adhesion force and the friction coefficient with the sliding velocity are represented in Figure A2.2

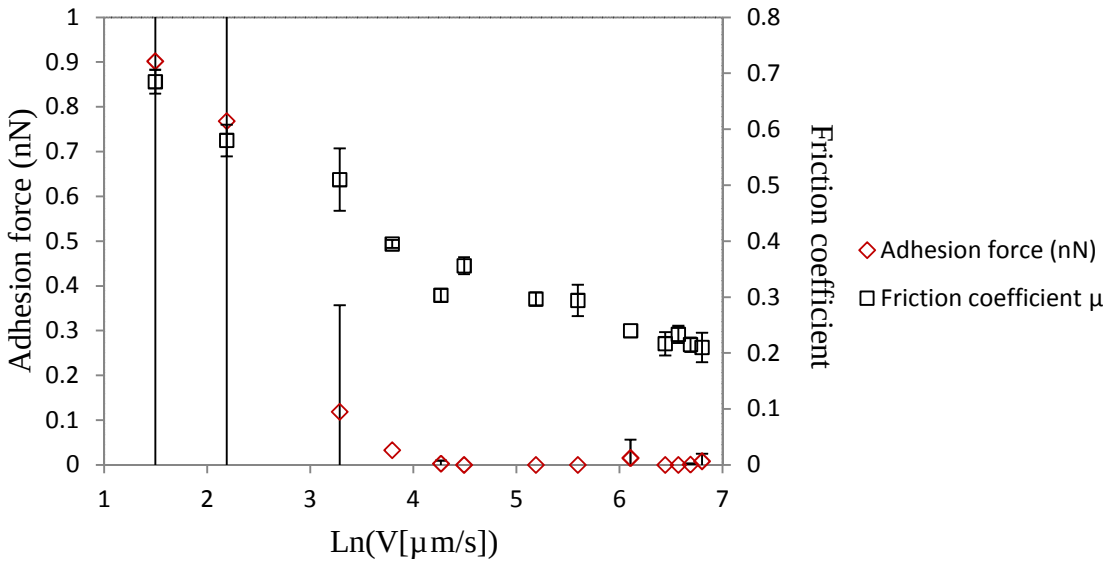

Figure A2. 2: Influence of the sliding velocity on the friction coefficient and on the adhesion force, on a polypropylene surface. Variation of the adhesion with sliding velocity depending on hydrophobicity of the surface, while an increase of the friction coefficient with the sliding velocity is observed, and the exact mechanism are still not clear.

The behavior of the adhesion force may be attributed possibly to a transition between JKR and DMT, even if wear was observed in these experiments (see Fig. A2. 3).

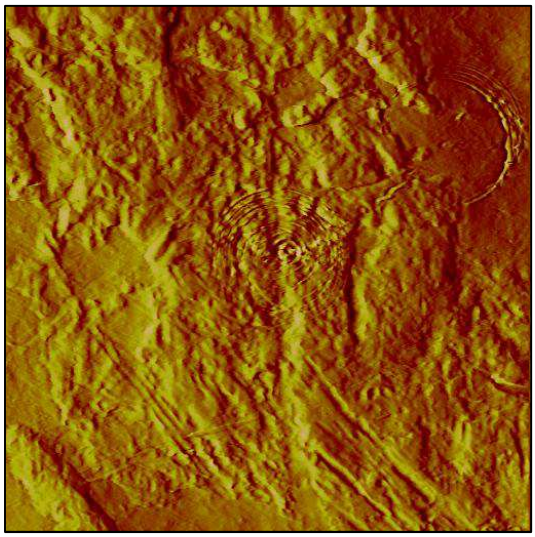

Figure A2. 3: 10 µm × 10 µm deflection error image obtained with contact tip on a Polypropylene surface showing circular imprints, after performing the experiments with the Circular mode.

Annex 3. Force Volume Mode

1. Force volume mode

A simple force curve records the force felt by the tip or the particle attached to the cantilever as it approaches and retracts from a point on the sample surface. Because most surfaces being examined are not homogeneous, it is often of interest to collect an array of force curves. Such an array produces information about the lateral distribution of different surface and/or material properties. Such an array of force curves is called a force volume which contains an array over the entire sample area. Force curves are measured at every point corresponding to a pixel (unique X-Y position) of the AFM image. Force curves from an array of X-Y points are combined into a three-dimensional array, or "volume," of force data (Fig. A3.1). Force volumes can be collected in any environment in which the microscope normally operates.

When the tip comes into contact with the surface during a force volume cycle, the point of contact provides the topography of the sample at that X-Y position. This can be used to produce a low (lateral) resolution height image of the surface, which is extremely useful when attempting to uncouple the interaction force data from topographic information [187]. Since the tip is not dragged across the surface of the sample while obtaining the data, lateral forces are very small.

The force volume allows investigating surface properties. For example, by the use of a simple force curve, one can measure the force needed to deform or indent the surface, and investigate the elastic properties of the material. Then a force volume can be used to produce micro-elasticity maps of the sample that show local variations in surface stiffness.

Another example is the adhesion maps that can be used to investigate the distribution of hydrophilic and hydrophobic regions on a surface which would differ in amount of acting force on the tip due to the presence of a capillary bridge on hydrophilic surfaces at ambient conditions.

Force volume imaging is a powerful AFM technique that can be used to investigate material, adhesive, electrical, magnetic and chemical properties of samples by recording an array of

force curves over an entire area. A topographic image is also recorded with minimal damage to the surface. The information in the force volume measurement may be decoupled from topographic data to offer new insight into material and surface properties.

A fundamental problem in force volume mode is the relatively long acquisition time that can easily amount to tens of minutes and can give rise to excessive drift.

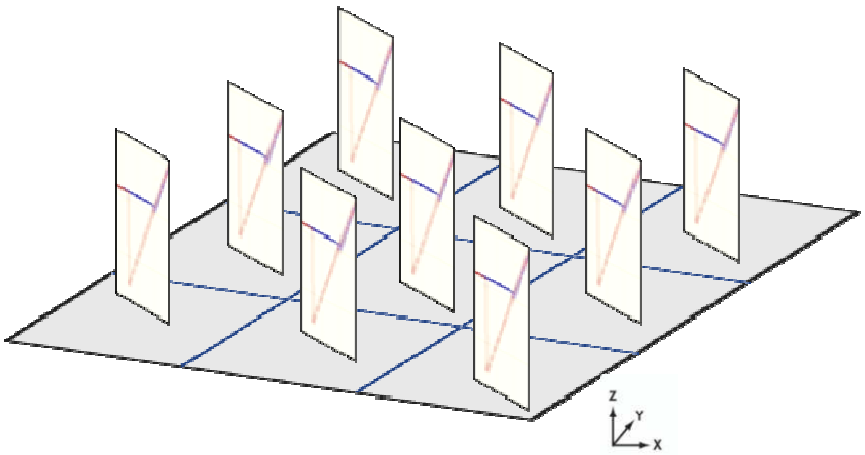

Figure A3. 1: A force volume data set – an array of regularly spaced force curves yields three-dimensional force information. In a force volume data set, the force curves will vary with X-Y position.

Annex 4. Lock-In-Amplifier

1. The lock-in technique

The lock in amplifier, otherwise known as the phase sensitive amplifier, uses a phase sensitive detection method for selecting (seeing) small signals in the presence of overwhelming noise. The lock-in amplifier is able to respond only to the portion of the input signal that occurs at a selected reference frequency. Typically, an experiment is performed at a fixed frequency (from an oscillator or function generator), and the lock-in detects the response from the experiment at the reference frequency. The lock-in-amp offers important adjustment parameters such as: The time constant that defines frequencies below which a filter will pass signals, indeed, the output from a phase sensitive detector passes through a low pas filter. Usually these filters are specified by the frequency at which their transmission is 3dB down on the pass band. But since this value is very low for a lock in amplifier output filter, then the frequencies are specified instead by a time constant which is inversely proportional to the -3dB frequency. Experimentally the time constant is used for stabilization. Typically, when there is noise at the input, there is noise on the output, and so by increasing the time constant, the output becomes more steady and easier to measure. Another interesting parameter in the lock-in-amp is the sensitivity that can maintain the output between 30% and 100% of the full scale. We used a model 7270 DSP lock in amplifier (Fig. A4.1) that allows fast data processing in our experiments, with a frequency range of 1 mHz to 250 kHz.

Figure A4. 1: Model 7270 DSP lock in amplifier, used for extracting the LFM signal with the Circular mode.

Table of Symbols

F : Force (N)

F_F : Friction force (N)

F_N: Normal force (N)

F_{P0}: Pull off force (N)

F_{el}: Electrostatic force (N)

F_{vdW}: Van der Waals force (N)

F_C: Capillary force (N)

μ : Friction coefficient

A : Area of contact (m^2)

a_H: Hertzian contact radius (m)

σ : Shear stress (N/m^2)

σ_0 : Intrinstic material shear strength (N/m^2)

P : Pressure (N/m^2)

P_m : Average normal pressure (N/m^2)

H : Hardness of the material (N/m^2)

a: Contact radius (m)

δ : Indentation depth (m)

R : Radius of curvature of a probe or a surface (m)

E : Young Modulus (N/m^2)

v : Poisson ratio

γ: Surface energy (J/m^2)

γ_{LV}: Liquid- vapour surface enetgy (J/m^2)

λ : Maugis parameter

$\in$: Range of action of surface force at equilibrium distance (m)

q : Electric charge (c)

d: Distance (m)

φ: Electric potential (V)

W: Interaction potential (V)

C: Interaction constant (V)

ρ: Density (g/cm^3)

Y(x): Periodic potential

ε_n: Static dielectric constant

A_H: Hamaker's constant (J)

n: Refrective index

R_K: Kelvin radius (m)

ξ: Full distribution of heights (m)

P_L: Laplace pressure (N/m^2)

S_{vdw}: Van der Waals free energy

A_W: Wet contact area (m^2)

k: Stiffness (N/m)

k_{eff}: Effective spring constant (N/m)

k_T: Lateral stiffness of the tip (N/m)

k_C: Lateral stiffness of the cantilever (N/m)

k_N: Normal stiffness (N/m)

V: Velocity (m/s)

p: Propability

T: Temperature (°C)

k_B: Boltzman constant

F_0: Lateral frequency (Hz)

U: Voltage (V)

Y_0: Periodic potential amplitude

ω: Angular frequency (Hz)

ΔZ: Vertical cantilever deflection (m)

ΔE: Energy barrier (J/mol)

r_a: Radius of a capillary bridge (m)

F_{adh}: Adhesion force (N)

Ω: Volume (m^3)

θ: Contact angle (°)

RH: Relative Humidity (%)

L: Load (N)

∅: Diffusion coefficient

D: Sliding distance (m)

REFERENCES

1. Braun, O.M. and J. Roder, *Transition from stick-slip to smooth sliding: An earthquakelike model.* Physical Review Letters, 2002. **88**(9): p. 096102.
2. Crassous, J., M. Ciccotti, and E. Charlaix, *Capillary Force between Wetted Nanometric Contacts and Its Application to Atomic Force Microscopy.* Langmuir, 2011. **27**(7): p. 3468-3473.
3. Halsey, T.C. and A.J. Levine, *How Sandcastles Fall.* Physical Review Letters, 1998. **80**(14): p. 3141.
4. Szlufarska, I., M. Chandross, and R.W. Carpick, *Recent advances in single-asperity nanotribology.* Journal of Physics D-Applied Physics, 2008. **41**(12).
5. O.Noel, P.-E. Mazeran, and H. Nasrallah, PCT-FR2011-051024 2010.
6. Wei, Z. and Y.-P. Zhao, *Experimental Investigation of the Velocity Effect on Adhesion Forces with an Atomic Force Microscope.* Chinese Physics Letters, 2004. **21**(4): p. 616.
7. Riedo, E., et al., *Kinetics of Capillary Condensation in Nanoscopic Sliding Friction.* Physical Review Letters, 2002. **88**(18): p. 185505.
8. Greiner, C., et al., *Local Nanoscale Heating Modulates Single-Asperity Friction.* Nano Letters, 2010. **10**(11): p. 4640-4645.
9. E. Rabinowicz, Friction and wear of materials. Number 2nd Edition. Wiley, New York, 1995.
10. B, N., J. Persson, Sliding Friction: Physical Principles and Applications. Number 2nd Edition. Springer, Heidelberg, 2000.
11. Singer, I.L. and H.M. Pollack, *Fundamentals of Friction: Macroscopic and Microscopic Processes (Kliwer, Dordrecht, 1992).*
12. Wolf, D.E. and P. Grassberger, *Workshop on Friction, Arching, Contact Dynamics, edited by D.E. Wolf and P. Grassberger (World Scientific, singapore, 1997).*
13. Greenwood, J.A., *Constriction resistance and the real area of contact.* British Journal of Applied Physics, 1966. **17**(12): p. 1621.
14. Bowden, F.P. and D. Tabor, *The Friction and Lubrication of Solids. F. P. Oxford Univ. Press, 1950.* 1950.
15. Greenwood, J.A. and J.B.P. Williamson, *Contact of Nominally Flat Surfaces.* Proceedings of the Royal Society of London. Series A, Mathematical and Physical Sciences 1966.
16. Bhushan, B., *Introduction To Tribology*: John Wiley and Sons (Aug 2002).
17. Dowson, D., *History of tribology.* London; New york, Longman., 1978.
18. Bharat Bhushan and B.K. Gupta, *Handbook of Tribology: Materials, Coatings, and Surface Treatments*. 1997: Krieger Publishing Company, Malabar, Florida U.S.A.
19. Mate, C.M., *Tribology on the Small Scale: A Bottom Up Approach to Friction, Lubrication, and Wear*. 2007, Oxford: Oxford University Press.
20. Kendall, K. and D. Tabor, *An Ultrasonic Study of the Area of Contact between Stationary and Sliding Surfaces.* Proceedings of the Royal Society of London. A. Mathematical and Physical Sciences, 1971. **323**(1554): p. 321-340.
21. Dieterich, J.H. and B.D. Kilgore, *Direct observation of frictional contacts: New insights for state-dependent properties.* Pure and Applied Geophysics, 1994. **143**(1): p. 283-302.
22. Carpick, R. and M. Salmeron, *Scratching the Surface: Fundamental Investigations of Tribology with Atomic Force Microscopy.* Chemical Reviews, 1997. **97**(4): p. 1163-1194.

23. Bowden, F.P. and T.P. Hughes, Proc. R. Soc. Lond. A, 172, 0280., 1939.
24. Greenwood, J.A. and J.B.P. Williamson, *Contact of Nominally Flat Surfaces.* Proceedings of the Royal Society of London. Series A. Mathematical and Physical Sciences, 1966. **295**(1442): p. 300-319.
25. H. Hertz, J. Reine Angew. Math. 92 156 (1881).
26. Johnson, K.L., K. Kendall, and A.D. Roberts, *Surface Energy and the Contact of Elastic Solids.* Proceedings of the Royal Society of London. A. Mathematical and Physical Sciences, 1971. **324**(1558): p. 301-313.
27. Harkins, W.D., *Cohesion, Internal Pressure, Adhesion, Tensile Strength, Tensile Energy, Negative Surface Energy, and Molecular Attraction.* Proceedings of the National Academy of Sciences, 1919. **5**(12): p. 562-568.
28. Derjaguin, B.V., V.M. Muller, and Y.P. Toporov, *Effect of contact deformations on the adhesion of particles.* Journal of Colloid and Interface Science, 1975. **53**(2): p. 314-326.
29. Enachescu, M., et al., *Observation of proportionality between friction and contact area at the nanometer scale.* Tribology Letters, 1999. **7**(2): p. 73-78.
30. Daniel, M., *Adhesion of spheres: The JKR-DMT transition using a dugdale model.* Journal of Colloid and Interface Science, 1992. **150**(1): p. 243-269.
31. Maugis, D. and B. Gauthier-Manuel, *JKR-DMT transition in the presence of a liquid meniscus.* Journal of Adhesion Science and Technology, 1994. **8**(11): p. 1311-1322.
32. D.S, D., *Yielding of steel sheets containing slits.* Journal of the Mechanics and Physics of Solids, 1960. **8**(2): p. 100-104.
33. Israelachvili, J., *Intermolecular and Surface Forces.* Intermolecular and Surface Forces (1977).
34. Burnham, N.A. and R.J. Colton, *Scanning Tunneling Microscopy and Spectroscopy: Theory, Techniques, and Applications,*. VCH, Weinhelm1993. p. 191.
35. Smythe, W.R., *Static and dynamic electricity*. 1939, New York: London McGraw-Hill.
36. F. London, *The General Theory of Molecular Forces.* Trans. Faraday Soc., 33, 8-26, (1937).
37. Hamaker, H.C., *The London--van der Waals attraction between spherical particles.* Physica, 1937. **4**(10): p. 1058-1072.
38. Argento, C. and R.H. French, *Parametric tip model and force--distance relation for Hamaker constant determination from atomic force microscopy.* Journal of Applied Physics, 1996. **80**(11): p. 6081-6090.
39. Müser, M., *Valentin L. Popov: Contact Mechanics and Friction: Physical Principles and Applications.* Tribology Letters. **40**(3): p. 395-395.
40. Versluys, J., Inst. Mitt. Bodenkunde, 7, 117., (1917).
41. Batel, W., Refract. J., 468., (1955).
42. Pietsch, W. and H. Rumpf, Chem. Ing. Tech., 39, 885., (1967)
43. Schubert, H., Chem. Ing. Tech., 45, 396., (1973).
44. Bocquet, L., et al., *Moisture-induced ageing in granular media and the kinetics of capillary condensation.* Nature, 1998. **396**(6713): p. 735-737.
45. Rabinovich, Y.I., et al., *Measurement of oil-mediated particle adhesion to a silica substrate by atomic force microscopy.* Journal of Adhesion Science and Technology, 2002. **16**(7): p. 887-903.
46. Fournier, Z. and et al., *Mechanical properties of wet granular materials.* Journal of Physics: Condensed Matter, 2005. **17**(9): p. S477.
47. Tabor, D. and R.H.S. Winterton, *Surface Forces: Direct Measurement of Normal and Retarded van der Waals Forces.* Nature, 1968. **219**(5159): p. 1120-1121.

48. Israelachvili, J.N. and D. Tabor, *The Measurement of Van Der Waals Dispersion Forces in the Range 1.5 to 130 nm.* Proceedings of the Royal Society of London. A. Mathematical and Physical Sciences, 1972. **331**(1584): p. 19-38.
49. Israelachvili, J., N., Adams, G. E. J. , Chem. Soc. Faraday Trans. 74:, 975–1001 (1978).
50. Mazuyer, D., et al., *Friction Dynamics of Confined Weakly Adhering Boundary Layers.* Langmuir, 2008. **24**(8): p. 3857-3866.
51. Israelachvili, J. and et al., *Recent advances in the surface forces apparatus (SFA) technique.* Reports on Progress in Physics, 2010. **73**(3): p. 036601.
52. Binnig, G., C.F. Quate, and C. Gerber, *Atomic Force Microscope.* Physical Review Letters, 1986. **56**(9): p. 930.
53. Binnig, G. and H. Rohrer, *Surface imaging by scanning tunneling microscopy.* Ultramicroscopy, 1983. **11**(2-3): p. 157-160.
54. G. Binnig, et al., Physica 109&110B, 2075 (1982).
.
55. Mate, C.M., et al., *Atomic-scale friction of a tungsten tip on a graphite surface.* Physical Review Letters, 1987. **59**(17): p. 1942.
56. Fei, H. and et al., *In situ tensile testing of nanofibers by combining atomic force microscopy and scanning electron microscopy.* Nanotechnology. **22**(36): p. 365708.
57. Doan, Q., *Electron beam energy and Ge nanocrystal size effects on the minority carrier diffusion length measured by the nano-electron beam induced current technique.* J. Appl. Phys. **110**(2): p. 024514.
58. Troyon, M., et al., *A Scanning Force Microscope Combined with a Scanning Electron Microscope for Multidimensional Data Analysis.* Microsc. Microanal. Microstruct., 1997. **8**(6): p. 393-402.
59. Lockwood, A.J. and et al., *Friction-formed liquid droplets.* Nanotechnology. **22**(10): p. 105703.
60. Gibson, C.T., G.S. Watson, and S. Myhra, *Lateral force microscopy -- a quantitative approach.* Wear, 1997. **213**(1-2): p. 72-79.
61. Gnecco, E., et al., *Velocity Dependence of Atomic Friction.* Physical Review Letters, 2000. **84**(6): p. 1172.
62. Zhong, W., et al., *First-principles theory of atomic-scale friction.* Physical Review Letters, 1990. **64**(25): p. 3054.
63. McClelland, G.M., in Adhesion and Friction, edited by M. Grunze and H.J. Kreuzer, Springer-Verlag Series, Berlin (1990), page 1.
64. Fujisawa, S. and et al., *The two-dimensional stick-slip phenomenon with atomic resolution.* Nanotechnology, 1993. **4**(3): p. 138.
65. G.A. Tomlinson, Phil. Mag. S. 7, 905 (1929).
66. Zwörner, O., et al., *The velocity dependence of frictional forces in point-contact friction.* Applied Physics A: Materials Science & Processing, 1998. **66**(0): p. S263-S267.
67. Helman, J.S., W. Baltensperger, and J.A. Hol/yst, *Simple model for dry friction.* Physical Review B, 1994. **49**(6): p. 3831.
68. Gourdon, D., et al., *The dependence of friction anisotropies on themolecular organisation of LB films as observed by AFM.* Tribology Letters, 1997. **3**(4): p. 317-324.
69. Prioli, R., et al., *Influence of velocity in nanoscale friction processes.* Applied Physics A: Materials Science & Processing, 2003. **76**(4): p. 565-569.

70. Fusco, C. and A. Fasolino, *Velocity dependence of atomic-scale friction: A comparative study of the one- and two-dimensional Tomlinson model.* Physical Review B, 2005. **71**(4): p. 045413.
71. Opitz, A., et al., *Nanofriction Mechanisms Derived from the Dependence of Friction on Load and Sliding Velocity from Air to UHV on Hydrophilic Silicon.* Tribology Letters, 2005. **20**(3): p. 229-234.
72. Riedo, E., et al., *The 2/3 Power Law Dependence of Capillary Force on Normal Load in Nanoscopic Friction.* The Journal of Physical Chemistry B, 2004. **108**(17): p. 5324-5328.
73. Opitz, A., et al., *Friction of thin water films: a nanotribological study.* Surface Science, 2002. **504**: p. 199-207.
74. Israelachvili, J.N. and R.M. Pashley, *Molecular layering of water at surfaces and origin of repulsive hydration forces.* Nature, 1983. **306**(5940): p. 249-250.
75. Chen, J., et al., *Velocity Dependence of Friction and Hydrogen Bonding Effects.* Physical Review Letters, 2006. **96**(23): p. 236102.
76. Bouhacina, T., et al., *Tribological behavior of a polymer grafted on silanized silica probed with a nanotip.* Physical Review B, 1997. **56**(12): p. 7694.
77. Eyring, H., *The Activated Complex in Chemical Reactions.* The Journal of Chemical Physics, 1935. **3**(2): p. 107-115.
78. Glosli, J.N. and G.M. McClelland, *Molecular dynamics study of sliding friction of ordered organic monolayers.* Physical Review Letters, 1993. **70**(13): p. 1960.
79. Scherge, M. and J.A. Schaefer, *Microtribological investigations of stick/slip phenomena using a novel oscillatory friction and adhesion tester.* Tribology Letters, 1998. **4**(1): p. 37-42.
80. Liu, H., S. Imad-Uddin Ahmed, and M. Scherge, *Microtribological properties of silicon and silicon coated with diamond like carbon, octadecyltrichlorosilane and stearic acid cadmium salt films: A comparative study.* Thin Solid Films, 2001. **381**(1): p. 135-142.
81. Hones, P., R. Sanjines, and F. Levy, *Characterization of sputter-deposited chromium nitride thin films for hard coatings.* Surface and Coatings Technology, 1997. **94-95**: p. 398-402.
82. Riedo, E., et al., *Nanotribology of carbon based thin films: the influence of film structure and surface morphology.* Surface Science, 2001. **477**(1): p. 25-34.
83. Elisa, R. and G. Enrico, *Thermally activated effects in nanofriction.* Nanotechnology, 2004. **15**(4): p. S288.
84. Riedo, E., et al., *Interaction Potential and Hopping Dynamics Governing Sliding Friction.* Physical Review Letters, 2003. **91**(8): p. 084502.
85. Fogden, A. and L.R. White, *Contact elasticity in the presence of capillary condensation: I. The nonadhesive Hertz problem.* Journal of Colloid and Interface Science, 1990. **138**(2): p. 414-430.
86. *"CIA- The world fact book".* Central Intelligence Agency. Retrieved 2008-12-20.
87. Hornbaker, D.J., et al., *What keeps sandcastles standing?* Nature, 1997. **387**(6635): p. 765-765.
88. Haul, R., *S. J. Gregg, K. S. W. Sing: Adsorption, Surface Area and Porosity. 2. Auflage, Academic Press, London 1982. 303 Seiten, Preis: $ 49.50.* Berichte der Bunsengesellschaft für physikalische Chemie, 1982. **86**(10): p. 957-957.
89. Evans, R. and P. Tarazona, *Theory of Condensation in Narrow Capillaries.* Physical Review Letters, 1984. **52**(7): p. 557.

90. Srinivasan, U., et al., *Alkyltrichlorosilane-based self-assembled monolayer films for stiction reduction in silicon micromachines.* Journal of Microelectromechanical Systems 1998. **7**(2): p. 252-260.
91. Weeks, B.L., M.W. Vaughn, and J.J. DeYoreo, *Direct Imaging of Meniscus Formation in Atomic Force Microscopy Using Environmental Scanning Electron Microscopy.* Langmuir, 2005. **21**(18): p. 8096-8098.
92. Christenson, H.K., *Capillary Condensation due to van der Waals Attraction in Wet Slits.* Physical Review Letters, 1994. **73**(13): p. 1821.
93. Kohonen, M.M., N. Maeda, and H.K. Christenson, *Kinetics of Capillary Condensation in a Nanoscale Pore.* Physical Review Letters, 1999. **82**(23): p. 4667.
94. Langmuir, I., *The Evaporation of Small Spheres.* Physical Review, 1918. **12**(5): p. 368.
95. Beaglehole, D., et al., *Inadequacy of Lifshitz theory for thin liquid films.* Physical Review Letters, 1991. **66**(16): p. 2084.
96. Restagno, F., et al., *Metastability and Nucleation in Capillary Condensation.* Physical Review Letters, 2000. **84**(11): p. 2433.
97. Frédéric Restagno and al., *Thermally activated dynamics of capillary condensation.* Journal of Physics: Condensed Matter, 2000. **12**(8A): p. A419.
98. Butt, H.-J., *Capillary Forces: Influence of Roughness and Heterogeneity.* Langmuir, 2008. **24**(9): p. 4715-4721.
99. Szoszkiewicz, R. and E. Riedo, *Nucleation Time of Nanoscale Water Bridges.* Physical Review Letters, 2005. **95**(13): p. 135502.
100. Sirghi, L., R. Szoszkiewicz, and E. Riedo, *Volume of a Nanoscale Water Bridge.* Langmuir, 2005. **22**(3): p. 1093-1098.
101. D'Amour, J.N., et al., *Capillary Aging of the Contacts between Glass Spheres and a Quartz Resonator Surface.* Physical Review Letters, 2006. **96**(5): p. 058301.
102. Stone, W., *Some phenomena of the contact of solids.* Phil. Mag. Vol. 9. 1930. 610-620.
103. Tomlinson, G.A., Phil. Mag. 6 (1928), p. 695.
104. Tomlinson, G.A., Phil. Mag., 10, pp.541-544 (1930).
105. Zimon, A.D., Adhesion of Dust and PowdersConsultants Bureau, New York (1982).
106. Ando, Y., *The effect of relative humidity on friction and pull-off forces measured on submicron-size asperity arrays.* Wear, 2000. **238**(1): p. 12-19.
107. Thundat, T., et al., *Role of relative humidity in atomic force microscopy imaging.* Surface Science Letters, 1993. **294**(1-2): p. L939-L943.
108. Xiao, X. and L. Qian, *Investigation of Humidity-Dependent Capillary Force.* Langmuir, 2000. **16**(21): p. 8153-8158.
109. Farshchi-Tabrizi, M., et al., *On the Adhesion between Fine Particles and Nanocontacts: An Atomic Force Microscope Study.* Langmuir, 2006. **22**(5): p. 2171-2184.
110. Paajanen, M., et al., *Experimental humidity dependency of small particle adhesion on silica and titania.* Journal of Colloid and Interface Science, 2006. **304**(2): p. 518-523.
111. Sugawara, Y., et al., *Effects of humidity and tip radius on the adhesive force measured with atomic force microscopy.* Wear, 1993. **168**(1-2): p. 13-16.
112. Jones, R., et al., *Adhesion Forces between Glass and Silicon Surfaces in Air Studied by AFM:â€‰ Effects of Relative Humidity, Particle Size, Roughness, and Surface Treatment.* Langmuir, 2002. **18**(21): p. 8045-8055.
113. He, M., et al., *Critical phenomena of water bridges in nanoasperity contacts.* The Journal of Chemical Physics, 2001. **114**(3): p. 1355-1360.

114. Fuji, M., et al., *Effect of Wettability on Adhesion Force between Silica Particles Evaluated by Atomic Force Microscopy Measurement as a Function of Relative Humidity.* Langmuir, 1999. **15**(13): p. 4584-4589.
115. Yang, C., U. Tartaglino, and B.N.J. Persson, *A multiscale molecular dynamics approach to contact mechanics.* The European Physical Journal E: Soft Matter and Biological Physics, 2006. **19**(1): p. 47-58.
116. Colbeck, S.C., *Capillary bonding of wet surfaces - the effects of contact angle and surface roughness.* Journal of Adhesion Science and Technology, 1997. **11**: p. 359-371.
117. Butt, H.-J., M. Farshchi-Tabrizi, and M. Kappl, *Using capillary forces to determine the geometry of nanocontacts.* Journal of Applied Physics, 2006. **100**(2): p. 024312-5.
118. Yang, C., U. Tartaglino, and B.N.J. Persson, *Influence of Surface Roughness on Superhydrophobicity.* Physical Review Letters, 2006. **97**(11): p. 116103.
119. Lundgren, M., et al., *Molecular Dynamics Study of Wetting of a Pillar Surface.* Langmuir, 2003. **19**(17): p. 7127-7129.
120. Lundgren, M., N.L. Allan, and T. Cosgrove, *Modeling of Wetting: A Study of Nanowetting at Rough and Heterogeneous Surfaces.* Langmuir, 2006. **23**(3): p. 1187-1194.
121. Wenzel, R.N., *RESISTANCE OF SOLID SURFACES TO WETTING BY WATER.* Industrial & Engineering Chemistry, 1936. **28**(8): p. 988-994.
122. Cassie, A.B.D. and S. Baxter, *Wettability of porous surfaces.* Transactions of the Faraday Society, 1944. **40**: p. 546-551.
123. Chow, T.S., *Wetting of rough surfaces.* Journal of Physics: Condensed Matter, 1998. **10**(27): p. L445.
124. Patankar, N.A., *On the Modeling of Hydrophobic Contact Angles on Rough Surfaces.* Langmuir, 2003. **19**(4): p. 1249-1253.
125. Gulbinski, W., et al., *Study of the influence of adsorbed water on AFM friction measurements on molybdenum trioxide thin films.* Surface Science, 2001. **475**(1-3): p. 149-158.
126. Rabinovich, Y.I., M.S. Esayanur, and B.M. Moudgil, *Capillary Forces between Two Spheres with a Fixed Volume Liquid Bridge: Theory and Experiment.* Langmuir, 2005. **21**(24): p. 10992-10997.
127. Tian, H. and T. Matsudaira, *The Role of Relative Humidity, Surface Roughness and Liquid Build-Up on Static Friction Behavior of the Head/Disk Interface.* Journal of Tribology, 1993. **115**(1): p. 28-35.
128. Hooton, J., et al., *An Atomic Force Microscopy Study of the Effect of Nanoscale Contact Geometry and Surface Chemistry on the Adhesion of Pharmaceutical Particles.* Pharmaceutical Research, 2004. **21**(6): p. 953-961.
129. Jang, J., J. Sung, and G.C. Schatz, *Influence of Surface Roughness on the Pull-Off Force in Atomic Force Microscopy.* The Journal of Physical Chemistry C, 2007. **111**(12): p. 4648-4654.
130. Mazeran, P.-E., *Effect of sliding velocity on capillary condensation and friction force in a nanoscopic contact.* Materials Science and Engineering: C, 2006. **26**(5-7): p. 751-755.
131. O. Noel., P.-E., Mazeran, and Nasrallah, H., *Velocity dependence of adhesion in a sliding nanometer-sized contact. Phys. Rev. Lett, 2011, (IN PRESS).*
132. Sirghi, L., *Effect of capillary-condensed water on the dynamic friction force at nanoasperity contacts.* Applied Physics Letters, 2003. **82**(21): p. 3755-3757.
133. Scherge, M., X. Li, and J.A. Schaefer, Tribology Letters, 1999. **6**(3): p. 215.

134. Nasrallah, H., P.-E. Mazeran, and O. Noel, *Circular mode: A new scanning probe microscopy method for investigating surface properties at constant and continuous scanning velocities.* Review of Scientific Instruments. **82**(11): p. 113703-6.
135. Elings; Virgil B and Gurley; John A, *Method of driving a piezoelectric scanner linearly with time* 1991, Digital Instruments, Inc.
136. Mate, C.M., *Tribology on the small scale a bottom up approach to friction, lubrication, and wear*: Oxford ; New York : Oxford University Press, 2008.
137. Loubet, J.L., et al., *Triboscopic description of local wear phenomena under an AFM tip.* Thin Solid Films, 1994. **253**(1-2): p. 194-198.
138. Sedin, D.L. and K.L. Rowlen, *Adhesion Forces Measured by Atomic Force Microscopy in Humid Air.* Analytical Chemistry, 2000. **72**(10): p. 2183-2189.
139. Israelachvili, J.N., *Intermolecular and surface forces*. second edition ed. 1991.
140. Cappella, B. and G. Dietler, *Force-distance curves by atomic force microscopy.* Surface Science Reports, 1999. **34**(1-3): p. 1-104.
141. Mazeran, P.E. and M. Beyaoui, *Initiation of sliding of an elastic contact at a nanometer scale under a scanning force microscope probe.* Tribology Letters, 2008. **30**(1): p. 1-11.
142. Jaroslaw, D., *The significance and magnitude of the line tension in three-phase (solid-liquid-fluid) systems.* Colloids and Surfaces A: Physicochemical and Engineering Aspects, 1996. **116**(1-2): p. 43-54.
143. de Gennes, P.G., *Wetting: statics and dynamics.* Reviews of Modern Physics, 1985. **57**(3): p. 827.
144. Colchero, J., *Lock?in technique for measuring friction on a nanometer scale.* Appl. Phys. Lett., 1996. **68**(20): p. 2896.
145. Mazeran, P.-E. and J.-L. Loubet, *Normal and lateral modulation with a scanning force microscope, an analysis: implication in quantitative elastic and friction imaging.* Tribology Letters, 1999. **7**(4): p. 199-212.
146. Mazeran, P.-E. and M. Beyaoui, *Initiation of Sliding of an Elastic Contact at a Nanometer Scale Under a Scanning Force Microscope Probe.* Tribology Letters, 2008. **30**(1): p. 1-11.
147. Jinesh, K.B. and J.W.M. Frenken, *Capillary Condensation in Atomic Scale Friction: How Water Acts like a Glue.* Physical Review Letters, 2006. **96**(16): p. 166103.
148. Li, T.-D., et al., *Structured and viscous water in subnanometer gaps.* Physical Review B, 2007. **75**(11): p. 115415.
149. Ulcinas, A., et al., *Shear Response of Nanoconfined Water on Muscovite Mica: Role of Cations.* Langmuir. **27**(17): p. 10351-10355.
150. Albrecht, T.R., et al., *Microfabrication of cantilever styli for the atomic force microscope.* Journal of Vacuum Science & Technology A: Vacuum, Surfaces, and Films, 1990. **8**(4): p. 3386-3396.
151. Tortonese, M., *Cantilevers and tips for atomic force microscopy.* IEEE Eng Med Biol Mag., 1997 Mar-Apr;. **16(2)**: p. 28-33.
152. Cleveland, J.P., et al., *A nondestructive method for determining the spring constant of cantilevers for scanning force microscopy.* Review of Scientific Instruments, 1993. **64**(2): p. 403-405.
153. John, E.S., et al., *Method for the calibration of atomic force microscope cantilevers*. Vol. 66. 1995: AIP. 3789-3798.
154. Cleveland, J.P., et al., *A nondestructive method for determining the spring constant of cantilevers for scanning force microscopy*. Vol. 64. 1993: AIP. 403-405.
155. Akihiro, T. and et al., *A method for determining the spring constant of cantilevers for atomic force microscopy.* Measurement Science and Technology, 1996. **7**(2): p. 179.

156. Jeffrey, L.H. and B. John, *Calibration of atomic?force microscope tips*. Vol. 64. 1993: AIP. 1868-1873.
157. Butt, H.J. and M. Jaschke, *Calculation of thermal noise in atomic force microscopy.* Nanotechnology, 1995. **6**(1): p. 1.
158. G. M. McClelland, R. Erlandsson, and S. Chiang, in Review of Progress in Quantitative Non-Destructive Evaluation, edited by D. O. Thompson and D. E. Chimenti (Plenum, New York, 1987), Vol. 6, p. 1307.
159. Martin, Y., C.C. Williams, and H.K. Wickramasinghe, *Atomic force microscope?force mapping and profiling on a sub 100?Å scale*. Vol. 61. 1987: AIP. 4723-4729.
160. Meyer, G. and N.M. Amer, *Erratum: Novel optical approach to atomic force microscopy.* Applied Physics Letters, 1988. **53**(24): p. 2400-2402.
161. Brunt, T.A., et al., *Measuring surface stress induced by electrode processes using a micromechanical sensor*. Journal of the Chemical Society, Faraday Transactions, 1996. **92**(20): p. 3807-3812.
162. S.M. Hues, R.J.C., E. Meyer and H.-J. Guntherodt,, *Scanning probe microscopy of thin film.* MRS Bulletin 1993: p. 41–49.
163. Noel, O., *Phénomènes d'adhésion à une échelle locale; une approche par AFM*. 2003, Université de Haute Alsace: Mulhouse.
164. Alexander, S.H., L.; Marti, O.; Schneir, J.; Elings, V., *An atomic-resolution atomic-force microscope implemented using an optical lever.* Journal of Applied Physics, 1989. **65**: p. 164-167.
165. Fujisawa, S., et al., *Lateral force curve for atomic force/lateral force microscope calibration.* Applied Physics Letters, 1995. **66**(4): p. 526-528.
166. Carpick, R.W., D.F. Ogletree, and M. Salmeron, *Lateral stiffness: A new nanomechanical measurement for the determination of shear strengths with friction force microscopy.* Applied Physics Letters, 1997. **70**(12): p. 1548-1550.
167. Piétrement, O., J.L. Beaudoin, and M. Troyon, *A new calibration method of the lateral contact stiffness and lateral force using modulated lateral force microscopy.* Tribology Letters, 1999. **7**(4): p. 213-220.
168. Ruan, J.-A. and B. Bhushan, *Atomic-Scale Friction Measurements Using Friction Force Microscopy: Part I---General Principles and New Measurement Techniques.* Journal of Tribology, 1994. **116**(2): p. 378-388.
169. Cain, R.G., S. Biggs, and N.W. Page, *Force Calibration in Lateral Force Microscopy.* Journal of Colloid and Interface Science, 2000. **227**(1): p. 55-65.
170. Attard, P., A. Carambassis, and M.W. Rutland, *Dynamic Surface Force Measurement. 2. Friction and the Atomic Force Microscope.* Langmuir, 1998. **15**(2): p. 553-563.
171. Feiler, A., P. Attard, and I. Larson, *Calibration of the torsional spring constant and the lateral photodiode response of frictional force microscopes.* Review of Scientific Instruments, 2000. **71**(7): p. 2746-2750.
172. Toikka, G.H., Robert A.; Ralston, John, *The application of lateral force microscopy to particle removal in aqueous polymer solutions.* Journal of Adhesion Science and Technology, 1997. **11**: p. 1479-1489.
173. Bogdanovic, G., A. Meurk, and M.W. Rutland, *Tip friction -- torsional spring constant determination.* Colloids and Surfaces B: Biointerfaces, 2000. **19**(4): p. 397-405.
174. Pettersson, T., et al., *Comparison of different methods to calibrate torsional spring constant and photodetector for atomic force microscopy friction measurements in air and liquid.* Review of Scientific Instruments, 2007. **78**(9): p. 093702-8.
175. Reitsma, M.G., *Lateral force microscope calibration using a modified atomic force microscope cantilever*. Review of Scientific Instruments, 2007. **78**(10): p. 106102-3.

176. Cannara, R.J., M. Eglin, and R.W. Carpick, *Lateral force calibration in atomic force microscopy: A new lateral force calibration method and general guidelines for optimization.* Review of Scientific Instruments, 2006. **77**(5): p. 053701-11.
177. Ecke, S., et al., *Measuring normal and friction forces acting on individual fine particles.* Review of Scientific Instruments, 2001. **72**(11): p. 4164-4170.
178. Quintanilla, M.A.S. and D.T. Goddard, *A calibration method for lateral forces for use with colloidal probe force microscopy cantilevers.* Review of Scientific Instruments, 2008. **79**(2): p. 023701-11.
179. Liu, E., B. Blanpain, and J.P. Celis, *Calibration procedures for frictional measurements with a lateral force microscope.* Wear, 1996. **192**(1-2): p. 141-150.
180. Ogletree, D.F., R.W. Carpick, and M. Salmeron, *Calibration of frictional forces in atomic force microscopy.* Review of Scientific Instruments, 1996. **67**(9): p. 3298-3306.
181. Varenberg, M., I. Etsion, and G. Halperin, *An improved wedge calibration method for lateral force in atomic force microscopy.* Review of Scientific Instruments, 2003. **74**(7): p. 3362-3367.
182. Tocha, E., H. Schönherr, and G.J. Vancso, *Quantitative Nanotribology by AFM: A Novel Universal Calibration Platform.* Langmuir, 2006. **22**(5): p. 2340-2350.
183. Wang, F. and X. Zhao, *Effect of contact stiffness on wedge calibration of lateral force in atomic force microscopy.* Review of Scientific Instruments, 2007. **78**(4): p. 043701-4.
184. Persson, B., *Theory of rubber friction and contact mechanics.* J. Chem. Phys., 2001. **115**(8): p. 3840.
185. B.N.J, P., *On the theory of rubber friction.* Surface Science, 1998. **401**(3): p. 445-454.
186. Persson, B., *Qualitative theory of rubber friction and wear.* J. Chem. Phys., 2000. **112**(4): p. 2021.
187. Delville, A., *Structure and properties of confined liquids: a molecular model of the clay-water interface.* The Journal of Physical Chemistry, 1993. **97**(38): p. 9703-9712.